NUWC-NPT Technical Report 11,143
24 May 1996

A Two-Wave Empirical Model of the Pressure Field in a Liquid-Filled Cylindrical Shell

Andrew J. Hull
Submarine Sonar Department

Naval Undersea Warfare Center Division
Newport, Rhode Island

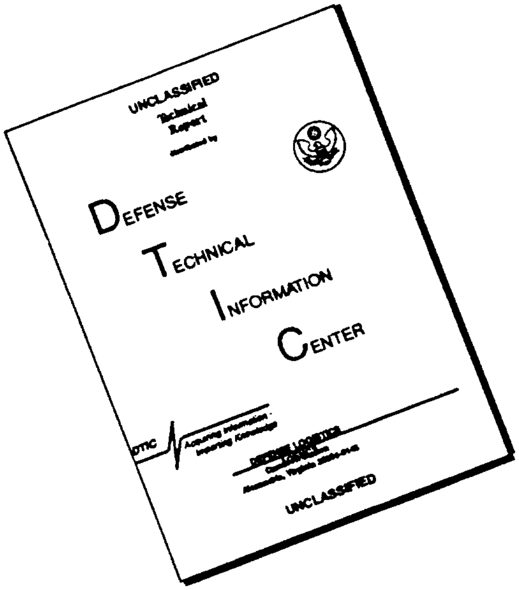

PREFACE

The investigation described in this report was sponsored by the Office of Naval Research in Arlington, Virginia.

The technical reviewer for this report was M. S. Peloquin (Code 2141).

The author wishes to thank K. A. Holt (Code 5131) for her help with the editing of the manuscript.

Reviewed and Approved: 24 May 1996

R. J. Martin
Acting Head, Submarine Sonar Department

REPORT DOCUMENTATION PAGE

Form Approved
OMB No. 0704-0188

1. AGENCY USE ONLY (Leave Blank)

2. REPORT DATE

24 May 1996

3. REPORT TYPE AND DATES COVERED

Final

4. TITLE AND SUBTITLE

A Two-Wave Empirical Model of the Pressure Field in a Liquid-Filled Cylindrical Shell

5. FUNDING NUMBERS

6. AUTHOR(S)

Andrew J. Hull

7. PERFORMING ORGANIZATION NAME(S) AND ADDRESS(ES)

Naval Undersea Warfare Center
Detachment New London
New London, Connecticut 06320

8. PERFORMING ORGANIZATION REPORT NUMBER

TR 11,143

9. SPONSORING/MONITORING AGENCY NAME(S) AND ADDRESS(ES)

Office of Naval Research
800 North Quincy Street
Arlington, VA 22217

10. SPONSORING/MONITORING AGENCY REPORT NUMBER

11. SUPPLEMENTARY NOTES

12a. DISTRIBUTION/AVAILABILITY STATEMENT

Approved for public release; distribution is unlimited.

12b. DISTRIBUTION CODE

13. ABSTRACT (Maximum 200 words)

This report develops an empirical wave propagation model of the pressure field in a liquid-filled cylindrical shell. Based on the assumption that both an extensional and a breathing wave are propagating in both the positive and negative axial directions of the shell, the model contains six unknown parameters: two forced wavenumbers and four wave propagation coefficients. The forced wavenumbers are solved for initially and then two different inverse methods are used to determine the wave propagation coefficients. The empirical model is compared to measured data taken at various locations in the shell. A method to determine the accuracy of the model and model assumptions is discussed.

14. SUBJECT TERMS

Breathing Wave Speed, Cylindrical Shell, Extensional Wave Speed, Forced Wavenumber, Inverse Method, Liquid-Filled Shell, Pressure Field, Wave Propagation Coefficient

15. NUMBER OF PAGES

90

16. PRICE CODE

17. SECURITY CLASSIFICATION OF REPORT	18. SECURITY CLASSIFICATION OF THIS PAGE	19. SECURITY CLASSIFICATION OF ABSTRACT	20. LIMITATION OF ABSTRACT
UNCLASSIFIED	UNCLASSIFIED	UNCLASSIFIED	SAR

TABLE OF CONTENTS

LIST OF ILLUSTRATIONS

LIST OF ILLUSTRATIONS (CONT'D)

LIST OF ILLUSTRATIONS (CONT'D)

LIST OF TABLES

A TWO-WAVE EMPIRICAL MODEL OF THE PRESSURE FIELD IN A LIQUID-FILLED CYLINDRICAL SHELL

1. INTRODUCTION

A comparison of experimental data with a model of the interior pressure field of a liquid-filled cylindrical shell often shows disagreement between prediction and measurement. One reason is that the models for this field [1-3] typically do not take into account such unmodeled processes as internal hydrophone mount noise, support cable interaction, and other noise effects that cause deviations from the measurements. In this report, a model of the pressure field in a liquid-filled cylindrical shell is developed based on experimental pressure measurements of the field. The underlying assumption is that two waves (an extensional and a breathing wave) are propagating in both axial directions of the shell. A four-term model that describes this motion is derived, and the six unknown model constants are determined with two inverse methods. The model makes no assumptions about the boundary conditions of the shell and the material properties of the shell or liquid. Concerning the shell/liquid interaction, the only assumption is that the dynamics of this process creates a breathing wave in the structure that originates at the bulkheads. This empirical model is developed as a "bridge" between theory and experiment, and it will identify the frequency ranges where disagreement typically occurs.

2. SYSTEM MODEL

The pressure field inside the liquid-filled shell is derived from two wave equations in the spatial domain, both of which use pressure as the independent variable. The first equation models the extensional wave contribution and is written as

$$\frac{\mathrm{d}^2 P_e(x,\omega)}{\mathrm{d}x^2} + k_e^2 P_e(x,\omega) = 0 \ , \tag{1}$$

where $P_e(x,\omega)$ is the temporal Fourier transform of the pressure that is generated by the extensional wave, x is the spatial location (m), ω is the excitation frequency (rad/s), and k_e is the complex extensional wavenumber, which is equal to

$$k_e = \frac{\omega}{c_e} \ , \tag{2}$$

where c_e is the complex extensional wave speed (m/s). The second wave equation models the breathing wave contribution and is written as

$$\frac{\mathrm{d}^2 P_b(x,\omega)}{\mathrm{d}x^2} + k_b^2 P_b(x,\omega) = 0 \ , \tag{3}$$

where $P_b(x,\omega)$ is the temporal Fourier transform of the pressure that is generated by the breathing wave and k_b is the complex breathing wavenumber (rad/m), which is equal to

$$k_b = \frac{\omega}{c_b} \ , \tag{4}$$

where c_b is the complex breathing wave speed (m/s). The solutions to equations (1) and (3) are complex exponential functions, and they can be added together using the principle of superposition, which yields the total pressure in the shell as

$$P(x,\omega) = P_b(x,\omega) + P_e(x,\omega) = \overline{A}(\omega)\mathrm{e}^{\mathrm{i}k_b x} + \overline{B}(\omega)\mathrm{e}^{-\mathrm{i}k_b x} + \overline{C}(\omega)\mathrm{e}^{\mathrm{i}k_e x} + \overline{D}(\omega)\mathrm{e}^{-\mathrm{i}k_e x} \ , \tag{5}$$

where $P(x,\omega)$ is the temporal Fourier transform of the pressure that is generated by both the extensional and breathing waves; i is the square root of -1; and $\overline{A}(\omega)$, $\overline{B}(\omega)$, $\overline{C}(\omega)$, and $\overline{D}(\omega)$ are wave propagation coefficients determined by the boundary conditions. It is now noted that the pressure field at x divided by the forward accelerometer is

$$\frac{P(x,\omega)}{\ddot{U}} = A(\omega)\mathrm{e}^{\mathrm{i}k_b x} + B(\omega)\mathrm{e}^{-\mathrm{i}k_b x} + C(\omega)\mathrm{e}^{\mathrm{i}k_e x} + D(\omega)\mathrm{e}^{-\mathrm{i}k_e x} \ , \tag{6}$$

where $\ddot{U}$ is the temporal Fourier transform of the acceleration at the forward end of the shell; $A(\omega)$, $B(\omega)$, $C(\omega)$, and $D(\omega)$ are wave propagation coefficients; and $P(x,\omega)/\ddot{U}$ has units of Pa//(m/s^2). Physically, the coefficient $A(\omega)$ corresponds to forward-traveling breathing wave energy, $B(\omega)$ corresponds to aft-traveling breathing wave energy, $C(\omega)$ corresponds to forward-traveling extensional wave energy, and $D(\omega)$ corresponds to aft-traveling extensional wave energy.

There are six unknowns in equation (6), which are the four wave propagation coefficients and the two forced (breathing and extensional) wavenumbers. Using a laboratory configuration in which a longitudinal shaker is placed at the forward end of a shell allows all these unknowns to be estimated. Due to the nonlinear (and sinusoidal) nature of the parameters in equation (6), the most numerically stable method is to first estimate the extensional wavenumber, then the breathing wavenumber, and finally the wave propagation coefficients. A method to estimate the extensional and breathing wavenumbers has previously been developed [4,5], and a shortened version is included here as section 3.

3. ESTIMATION OF THE FORCED WAVENUMBERS

In order to estimate the wave propagation coefficients and the breathing wavenumber (and the corresponding breathing wave speed), it is necessary to know the extensional wavenumber (which is related to the corresponding extensional wave speed by equation (2)). This complex, frequency-dependent quantity is determined using measurements from forward and aft impedance heads that are attached to the shell ends in the test facility [4]. Although these measurements contain a breathing wave contribution, it typically occurs only at low frequencies and can be easily discerned from the extensional wave effects. Such behavior is described in the experiment section.

The governing differential equation of the extensional wave is expressed on the spatial domain as a single wave equation with particle displacement as the independent variable:

$$\frac{d^2U(x,\omega)}{dx^2} + k_e^2 U(x,\omega) = 0 \ , \tag{7}$$

where $U(x,\omega)$ is the temporal Fourier transform of the axial displacement. Equation (7) is a one-dimensional "lumped" approximation of the extensional wave motion in the system that combines the effect of the shell and the liquid together as a homogeneous medium that supports longitudinal wave motion. Although this approximation is not sufficient to model the radial motion of the shell, it is an accurate model of axial motion and the corresponding extensional wave propagation in the liquid-filled shell. The energy attenuation in the shell is defined with a structural damping law, and therefore the wave speed is a complex quantity. The real part of the wave speed corresponds to energy transmission and the imaginary part corresponds to energy attenuation.

The solution to equation (7) is

$$U(x,\omega) = G(\omega)\mathrm{e}^{\mathrm{i}k_e x} + H(\omega)\mathrm{e}^{-\mathrm{i}k_e x} , \tag{8}$$

where $G(\omega)$ and $H(\omega)$ are coefficients determined by the boundary conditions at the ends of the shell. The temporal Fourier transform of the axial force in the shell is

$$F(x,\omega) = A_s E_x \frac{\mathrm{d}U(x,\omega)}{\mathrm{d}x} = A_s E_x \mathrm{i}k_e \left[G(\omega)\mathrm{e}^{\mathrm{i}k_e x} - H(\omega)\mathrm{e}^{-\mathrm{i}k_e x} \right] , \tag{9}$$

where A_s is the cross-sectional area of the shell (m^2) and E_x is the effective longitudinal modulus of the shell (N/m^2). The known parameters in equations (8) and (9) are the location of the sensors (x) and the frequency of excitation (ω). Although the effective longitudinal modulus (E_x) is unknown, equation (9) will be rewritten as a ratio of forces permitting the cancellation of this term and the cross-sectional area (A_s). Additionally, the coefficients $G(\omega)$ and $H(\omega)$ are unknown; however, they will be condensed out of the mathematical relationships. The inversion of equations (8) and (9) at the sensor locations will allow for a measurement of the unknown extensional wavenumber k_e and extensional wave speed c_e. This technique is described next.

In the extensional wave measurement part of the experiment, the forward and aft pair of sensors (impedance heads) described earlier collect data that are in the form of transfer functions between each pair. The position of the forward pair of sensors is defined as $x = 0$ and of the aft pair as $x = L$, where L is the length of the shell (m). The two transfer function measurements used are the forward displacement divided by the aft displacement and the forward force divided by the aft force. Their theoretical form can be rewritten using equations (8) and (9) as

$$\frac{U(0,\omega)}{U(L,\omega)} = \frac{G(\omega)+H(\omega)}{G(\omega)\mathrm{e}^{\mathrm{i}k_e L}+H(\omega)\mathrm{e}^{-\mathrm{i}k_e L}} = R_1 \qquad (10)$$

and

$$\frac{F(0,\omega)}{F(L,\omega)} = \frac{G(\omega)-H(\omega)}{G(\omega)\mathrm{e}^{\mathrm{i}k_e L}-H(\omega)\mathrm{e}^{-\mathrm{i}k_e L}} = R_2 \ , \qquad (11)$$

where R_1 and R_2 are transfer function data from the experiment at a specific test frequency. Equations (10) and (11) are rewritten as functions of $H(\omega)/G(\omega)$ and are set equal to each other, yielding

$$\cos(k_e L) = \frac{R_2 R_1 + 1}{R_2 + R_1} = \phi \ , \qquad (12)$$

where ϕ is a complex quantity. Using an angle-sum relationship on the complex cosine term in equation (12) and separating the equation into real and imaginary parts results in

$$\cosh[\mathrm{Im}(k_e)L] = \frac{\mathrm{Re}(\phi)}{\cos[\mathrm{Re}(k_e)L]} \qquad (13)$$

and

$$\sinh[\mathrm{Im}(k_e)L] = \frac{-\mathrm{Im}(\phi)}{\sin[\mathrm{Re}(k_e)L]} \ , \qquad (14)$$

where Re denotes the real part and Im denotes the imaginary part of the corresponding complex quantity.

Equation (14) is now squared and subtracted from the square of equation (13), yielding

$$\left\{\cosh[\mathrm{Im}(k_e)L]\right\}^2 - \left\{\sinh[\mathrm{Im}(k_e)L]\right\}^2 = \frac{[\mathrm{Re}(\phi)]^2}{\left\{\cos[\mathrm{Re}(k_e)L]\right\}^2} - \frac{[\mathrm{Im}(\phi)]^2}{\left\{\sin[\mathrm{Re}(k_e)L]\right\}^2} = 1 \ . \qquad (15)$$

Equation (15) can be simplified with trigonometric power relationships to

$$\cos[2\,\mathrm{Re}(k_e)L] =$$

$$[\mathrm{Re}(\phi)]^2 + [\mathrm{Im}(\phi)]^2 - \sqrt{\left([\mathrm{Re}(\phi)]^2 + [\mathrm{Im}(\phi)]^2\right)^2 - \left(2[\mathrm{Re}(\phi)]^2 - 2[\mathrm{Im}(\phi)]^2 - 1\right)} = s \ . \qquad (16)$$

Note that only a negative sign in front of the radical is used. The real part of k_e in equation (16) is now solved for by

$$\mathrm{Re}(k_e) = \begin{cases} \dfrac{1}{2L}\mathrm{Arc}\cos(s) + \dfrac{n\pi}{2L} & n \text{ even} \\ \\ \dfrac{1}{2L}\mathrm{Arc}\cos(-s) + \dfrac{n\pi}{2L} & n \text{ odd} \end{cases} , \tag{17}$$

where n is a nonnegative integer and capital A denotes the principal value of the inverse cosine function. The value of n is determined from the function s, which is a cosine function with respect to frequency. At zero frequency, n is 0. Every time s cycles through π radians, n is increased by 1. The imaginary part of k_e is determined by adding equations (13) and (14) together, resulting in

$$\mathrm{Im}(k_e) = \frac{1}{L}\log_e\left\{\frac{\mathrm{Re}(\phi)}{\cos[\mathrm{Re}(k_e)L]} - \frac{\mathrm{Im}(\phi)}{\sin[\mathrm{Re}(k_e)L]}\right\} . \tag{18}$$

Now that the real and imaginary parts of the wavenumber k_e are known, the complex-valued extensional wave speed can be determined at each frequency by

$$c_e = \mathrm{Re}(c_e) + \mathrm{i}\,\mathrm{Im}(c_e) = \frac{\omega}{k_e} . \tag{19}$$

Note that the extensional wave speed has been measured without knowing the boundary conditions at $x = 0$ and $x = L$.

Once the extensional wave speed is known, five independent equally spaced measurements of the spatial pressure field are needed to eliminate the wave propagation coefficients and solve for the breathing wave speed [5]. Without loss of generality, the origin of the coordinate system is defined as $x = 0$ at the middle (third) pressure sensor (hydrophone). Equation (6) is written to correspond to the locations of the five pressure sensors as

$$\frac{P(-2\delta,\omega)}{\ddot{U}} = A(\omega)\mathrm{e}^{-\mathrm{i}k_e 2\delta} + B(\omega)\mathrm{e}^{\mathrm{i}k_e 2\delta} + C(\omega)\mathrm{e}^{-\mathrm{i}k_b 2\delta} + D(\omega)\mathrm{e}^{\mathrm{i}k_b 2\delta} = S_1 , \tag{20}$$

$$\frac{P(-\delta,\omega)}{\ddot{U}} = A(\omega)\mathrm{e}^{-\mathrm{i}k_e \delta} + B(\omega)\mathrm{e}^{\mathrm{i}k_e \delta} + C(\omega)\mathrm{e}^{-\mathrm{i}k_b \delta} + D(\omega)\mathrm{e}^{\mathrm{i}k_b \delta} = S_2 , \tag{21}$$

$$\frac{P(0,\omega)}{\ddot{U}} = A(\omega) + B(\omega) + C(\omega) + D(\omega) = S_3 \ , \tag{22}$$

$$\frac{P(\delta,\omega)}{\ddot{U}} = A(\omega)\mathrm{e}^{\mathrm{i}k_e\delta} + B(\omega)\mathrm{e}^{-\mathrm{i}k_e\delta} + C(\omega)\mathrm{e}^{\mathrm{i}k_b\delta} + D(\omega)\mathrm{e}^{-\mathrm{i}k_b\delta} = S_4 \ , \tag{23}$$

and

$$\frac{P(2\delta,\omega)}{\ddot{U}} = A(\omega)\mathrm{e}^{\mathrm{i}k_e 2\delta} + B(\omega)\mathrm{e}^{-\mathrm{i}k_e 2\delta} + C(\omega)\mathrm{e}^{\mathrm{i}k_b 2\delta} + D(\omega)\mathrm{e}^{-\mathrm{i}k_b 2\delta} = S_5 \ , \tag{24}$$

where δ is the sensor-to-sensor spacing (m) and S_1 through S_5 correspond to the measured transfer function data of the hydrophone divided by the forward accelerometer at a specific frequency.

Equations (21) and (23) are now added together to yield

$$(A+B)\cos(k_e\delta) + (C+D)\cos(k_b\delta) = (1/2)(S_2 + S_4) \ , \tag{25}$$

and equations (20) and (24) are added together to produce

$$(A+B)\cos(k_e 2\delta) + (C+D)\cos(k_b 2\delta) = (1/2)(S_1 + S_5) \ . \tag{26}$$

Equation (22) is then rewritten with the term $(A + B)$ on the left-hand side and is substituted into equations (25) and (26), yielding

$$C + D = \frac{(1/2)(S_2 + S_4) - S_3\cos(k_e\delta)}{\cos(k_b\delta) - \cos(k_e\delta)} \tag{27}$$

and

$$C + D = \frac{(1/2)(S_1 + S_5) - S_3\cos(k_e 2\delta)}{\cos(k_b 2\delta) - \cos(k_e 2\delta)} \ , \tag{28}$$

respectively. Equations (27) and (28) are next set equal to each other. Applying a double angle trigonometric relationship to the $\cos(k_b 2\delta)$ term then produces

$$X\cos^2(k_b\delta) + Y\cos(k_b\delta) + Z = 0 \ , \tag{29a}$$

where

$$X = (S_2 + S_4) - 2S_3\cos(k_e\delta) \ , \tag{29b}$$

$$Y = S_3\cos(k_e\delta) - (1/2)(S_1 + S_5) \ , \tag{29c}$$

and

$$Z = [(1/2)(S_1 + S_5) + S_3]\cos(k_e\delta) - (1/2)(S_2 + S_4)\cos(k_e 2\delta) - (1/2)(S_2 + S_4) \ . \tag{29d}$$

Equation (29) is a quadratic form with the solution

$$\cos(k_b\delta) = \frac{-Y \pm \sqrt{Y^2 - 4XZ}}{2X} = \psi \ , \tag{30}$$

where ψ is a complex quantity. Rewriting equation (30) as real and imaginary terms produces

$$\cos[2\,\mathrm{Re}(k_b)\delta] =$$

$$[\mathrm{Re}(\psi)]^2 + [\mathrm{Im}(\psi)]^2 - \sqrt{\left([\mathrm{Re}(\psi)]^2 + [\mathrm{Im}(\psi)]^2\right)^2 - \left(2[\mathrm{Re}(\psi)]^2 - 2[\mathrm{Im}(\psi)]^2 - 1\right)} = r \ , \tag{31}$$

where Re denotes the real part and Im denotes the imaginary part of the corresponding complex quantity. Note that only a negative sign in front of the radical is used in equation (31). However, both the negative and the positive signs in front of the radical in equation (30) are needed. The real part of k_b in equation (31) is now solved for by

$$\mathrm{Re}(k_b) = \begin{cases} \dfrac{1}{2\delta}\mathrm{Arc}\cos(r) + \dfrac{m\pi}{2\delta} & m \text{ even} \\ \\ \dfrac{1}{2\delta}\mathrm{Arc}\cos(-r) + \dfrac{m\pi}{2\delta} & m \text{ odd} \end{cases} \ , \tag{32}$$

where m is a nonnegative integer and capital A denotes the principal value of the inverse cosine function. The value of m is determined from the function r, which is a cosine function with respect to frequency. At zero frequency, m is 0. Every time r cycles through π radians, m is increased by 1. The imaginary part of k_b is determined from equation (30), resulting in

$$\mathrm{Im}(k_b) = \frac{1}{\delta}\log_e\left\{\frac{\mathrm{Re}(\psi)}{\cos[\mathrm{Re}(k_b)\delta]} - \frac{\mathrm{Im}(\psi)}{\sin[\mathrm{Re}(k_b)\delta]}\right\} . \tag{33}$$

Now that the real and imaginary parts of the wavenumber k_b are known, the complex-valued breathing wave speed can be determined at each frequency with

$$c_b = \mathrm{Re}(c_b) + \mathrm{i}\,\mathrm{Im}(c_b) = \frac{\omega}{k_b} \ . \tag{34}$$

Use of this method produces two wave speed measurements because of the retention of the positive and negative signs in equation (30). One of the wave speeds is the breathing wave speed, and the other is the extensional wave speed, which was previously known. The extensional wave speed is typically at least one order of magnitude greater than the breathing wave speed.

4. ESTIMATION OF THE WAVE PROPAGATION COEFFICIENTS

Two methods are now used to estimate the wave propagation coefficients. The first, which uses four hydrophone measurements and (mathematically) produces an exact solution for the coefficients, is called the direct inverse method. The second uses N hydrophone measurements and a Gauss linearization scheme with an ordinary least squares constraint to solve for the coefficients [6]. Both these methods are mathematically developed in this section and applied to data in the experiment section.

In the first method, equation (6) is rewritten at four different hydrophone measurement locations as

$$\frac{P(x_1,\omega)}{\ddot{U}} = A(\omega)e^{ik_b x_1} + B(\omega)e^{-ik_b x_1} + C(\omega)e^{ik_e x_1} + D(\omega)e^{-ik_e x_1} = T_1 \ , \tag{35}$$

$$\frac{P(x_2,\omega)}{\ddot{U}} = A(\omega)e^{ik_b x_2} + B(\omega)e^{-ik_b x_2} + C(\omega)e^{ik_e x_2} + D(\omega)e^{-ik_e x_2} = T_2 \ , \tag{36}$$

$$\frac{P(x_3,\omega)}{\ddot{U}} = A(\omega)e^{ik_b x_3} + B(\omega)e^{-ik_b x_3} + C(\omega)e^{ik_e x_3} + D(\omega)e^{-ik_e x_3} = T_3 \ , \tag{37}$$

and

$$\frac{P(x_4,\omega)}{\ddot{U}} = A(\omega)e^{ik_b x_4} + B(\omega)e^{-ik_b x_4} + C(\omega)e^{ik_e x_4} + D(\omega)e^{-ik_e x_4} = T_4 \ , \tag{38}$$

where T_1, T_2, T_3, and T_4 are the transfer function data at a specific frequency. Unlike the estimation of the breathing wave speed, it is not necessary that the spatial distances x_1 through x_4 be equally spaced. Equations (35)-(38) are now written in matrix form as

$$\begin{bmatrix} e^{ik_b x_1} & e^{-ik_b x_1} & e^{ik_e x_1} & e^{-ik_e x_1} \\ e^{ik_b x_2} & e^{-ik_b x_2} & e^{ik_e x_2} & e^{-ik_e x_2} \\ e^{ik_b x_3} & e^{-ik_b x_3} & e^{ik_e x_3} & e^{-ik_e x_3} \\ e^{ik_b x_4} & e^{-ik_b x_4} & e^{ik_e x_4} & e^{-ik_e x_4} \end{bmatrix} \begin{Bmatrix} A(\omega) \\ B(\omega) \\ C(\omega) \\ D(\omega) \end{Bmatrix} = \begin{Bmatrix} T_1 \\ T_2 \\ T_3 \\ T_4 \end{Bmatrix} . \tag{39}$$

The coefficients are then solved for by multiplication of each side of equation (39) by a matrix inverse, which results in

$$\begin{Bmatrix} A(\omega) \\ B(\omega) \\ C(\omega) \\ D(\omega) \end{Bmatrix} = \begin{bmatrix} e^{ik_b x_1} & e^{-ik_b x_1} & e^{ik_e x_1} & e^{-ik_e x_1} \\ e^{ik_b x_2} & e^{-ik_b x_2} & e^{ik_e x_2} & e^{-ik_e x_2} \\ e^{ik_b x_3} & e^{-ik_b x_3} & e^{ik_e x_3} & e^{-ik_e x_3} \\ e^{ik_b x_4} & e^{-ik_b x_4} & e^{ik_e x_4} & e^{-ik_e x_4} \end{bmatrix}^{-1} \begin{Bmatrix} T_1 \\ T_2 \\ T_3 \\ T_4 \end{Bmatrix} . \tag{40}$$

In the second method, or the Gauss linearization scheme, the matrix iteration equation to estimate the wave propagation coefficients is

$$\mathbf{b}^{(k+1)} = \mathbf{b}^{(k)} + \left[[\mathbf{X}^{(k)}]^{\mathrm{T}} [\mathbf{X}^{(k)}] \right]^{-1} \left[[\mathbf{X}^{(k)}]^{\mathrm{T}} (\mathbf{y} - \mathbf{h}^{(k)}) \right] , \tag{41}$$

where the superscript k represents the kth iteration; the vector $\mathbf{b}$ is the wave propagation coefficient vector and is equal to

$$\mathbf{b} = \begin{Bmatrix} A(\omega) \\ B(\omega) \\ C(\omega) \\ D(\omega) \end{Bmatrix} ; \tag{42}$$

$\mathbf{X}$ is the following N by 4 sensitivity coefficient matrix

$$\mathbf{X} = \begin{bmatrix} e^{ik_b x_1} & e^{-ik_b x_1} & e^{ik_e x_1} & e^{-ik_e x_1} \\ e^{ik_b x_2} & e^{-ik_b x_2} & e^{ik_e x_2} & e^{-ik_e x_2} \\ \vdots & \vdots & \vdots & \vdots \\ e^{ik_b x_N} & e^{-ik_b x_N} & e^{ik_e x_N} & e^{-ik_e x_N} \end{bmatrix} ; \tag{43}$$

$\mathbf{y}$ is the N dimensional vector containing the measurement data as

$$\mathbf{y} = \begin{Bmatrix} T_1 \\ T_2 \\ \vdots \\ T_N \end{Bmatrix} ; \tag{44}$$

and **h** is the N dimensional vector containing the model calculated using the current value of the estimated parameters and is equal to

$$\mathbf{h} = \begin{Bmatrix} A(\omega)e^{ik_b x_1} + B(\omega)e^{-ik_b x_1} + C(\omega)e^{ik_e x_1} + D(\omega)e^{-ik_e x_1} \\ A(\omega)e^{ik_b x_2} + B(\omega)e^{-ik_b x_2} + C(\omega)e^{ik_e x_2} + D(\omega)e^{-ik_e x_2} \\ \vdots \\ A(\omega)e^{ik_b x_N} + B(\omega)e^{-ik_b x_N} + C(\omega)e^{ik_e x_N} + D(\omega)e^{-ik_e x_N} \end{Bmatrix} . \tag{45}$$

Once the equations are assembled, the matrix **b** can be determined by iteration on the left-hand side of equation (41) at each specific frequency.

5. EXPERIMENT

Use of this model with the inverse method corresponds to the physical testing configuration in the Axial Vibration Test Facility (AVTF) at the Naval Undersea Warfare Center/Division Newport, as shown in figure 1. The AVTF has been designed to provide a simple procedure for testing long structures under varying tensions and temperatures. The longitudinal shaker at its forward end provides axial excitation to the structure. A rope attached to the aft end of the structure and a winch allows the tension to be adjusted. A mass is attached between the shell and the rope to increase the force levels and decrease the acceleration levels. This mass also produces an impedance change at the end of the bar that is sufficiently large to allow accurate modeling of the rope behavior by a spring and damper rather than by a continuous media expression. A rail from which thin Kevlar lines can be hung to provide lateral support to heavy or long test specimens runs the entire length of the facility. The unit is completely surrounded by an air-conditioned PVC duct to permit temperature-dependent testing. To collect data during a test, impedance heads are attached to the forward and aft ends of the structure (as described earlier). Each impedance head consists of a single axial force transducer and an accelerometer. Additional data are collected by hydrophones in the liquid-filled shell. A load cell that measures the tension on the structure is located between the rope and the mass.

Equipment used in this experiment includes a Zonic Corporation model 1215-10-T-ZSP86 hydraulic shaker, two PCB Piezotronics model 348A accelerometers, two PCB Piezotronics model 233A force transducers, a Lebow model 31/3 load cell, and a Cordem Corporation model 1215-RMO tension drum.

In the first part of the experiment, which measures the extensional wave speed, a longitudinally reinforced liquid-filled urethane shell containing five equally spaced hydrophones was placed in tension, as shown in figure 1. The shell had a mean radius of 0.015 m and a thickness of 0.0028 m; the internal liquid had a density of 760 kg/m^3. The axial tension on the shell was 890 N and the stressed length was 12.0 m. The point mass had a weight of 13.6 kg. The data from the force transducers, accelerometers, and hydrophones were acquired in the time domain with a Hewlett Packard (HP) 3562 dynamic signal analyzer. The analyzer then Fourier transformed the raw data to the frequency domain to obtain the desired transfer functions. The test was run with a frequency range between 3 and 100 Hz.

Equations (7)-(19) were applied to the experimental test data taken with the force transducers and accelerometers, and the resulting extensional wave speed of the structure was found. Figure 2 shows the calculated extensional wave speed versus frequency. The solid line corresponds to the computed wave speed and the dashed line to the ordinary least squares (OLS) straight-line fit. The OLS fit was applied to the data between 35 and 100 Hz to minimize the effect of the breathing wave interaction seen at lower frequencies. The resulting OLS fit was $c_e = 677.3 + 0.8f$ (m/s) for the real part and $c_e = 83.3 - 0.05f$ (m/s) for the imaginary part (where f is frequency in Hertz). These same values are used for the extensional wave speed in the following calculations in order to determine the breathing wave speed and estimate the wave propagation coefficients.

In the second part of the experiment, transfer functions of the hydrophone data divided by the forward accelerometer data were collected. The five hydrophones were spaced at intervals of 1.83 m with a distance of 2.96 m from the forward end of the shell to the first hydrophone. Equations (20)-(34) were applied to the experimental test data, and the resulting breathing wave speed of the structure was calculated. Figure 3 is a plot of the breathing wave speed versus frequency. The plus symbols mark the data from this experiment that were obtained using the method developed in section 3. In the figure, it is noted that the breathing wave for this specific structure is spatially coherent from 3 to 13 Hz. Above 13 Hz, the imaginary part of the measurement begins to diverge. It is also possible that effects other than spatial incoherence are preventing the breathing wave from being identified at higher frequencies. Changing the extensional wave speed by ±20 percent and recalculating the breathing wave speed produced a change in the breathing wave speed of less than 1 percent. Thus, the breathing wave speed measurement method is very insensitive to incorrect extensional wave speeds. Additionally, the breathing wave speed was also insensitive to varying axial tensions.

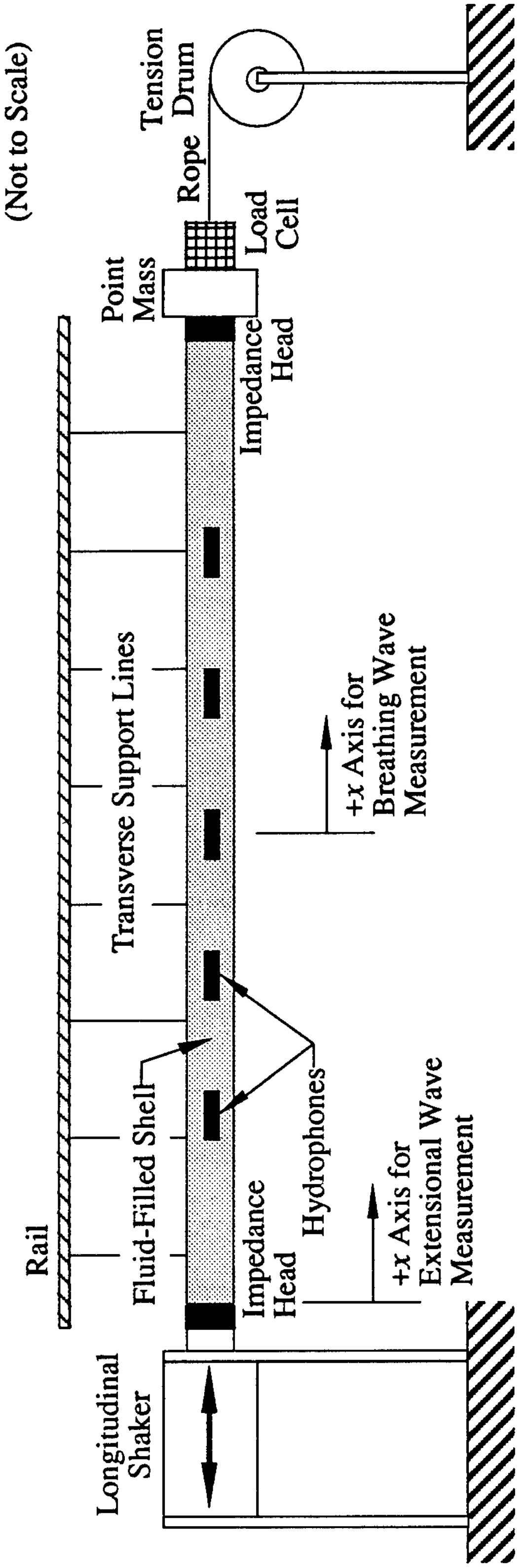

Figure 1. The Laboratory Configuration

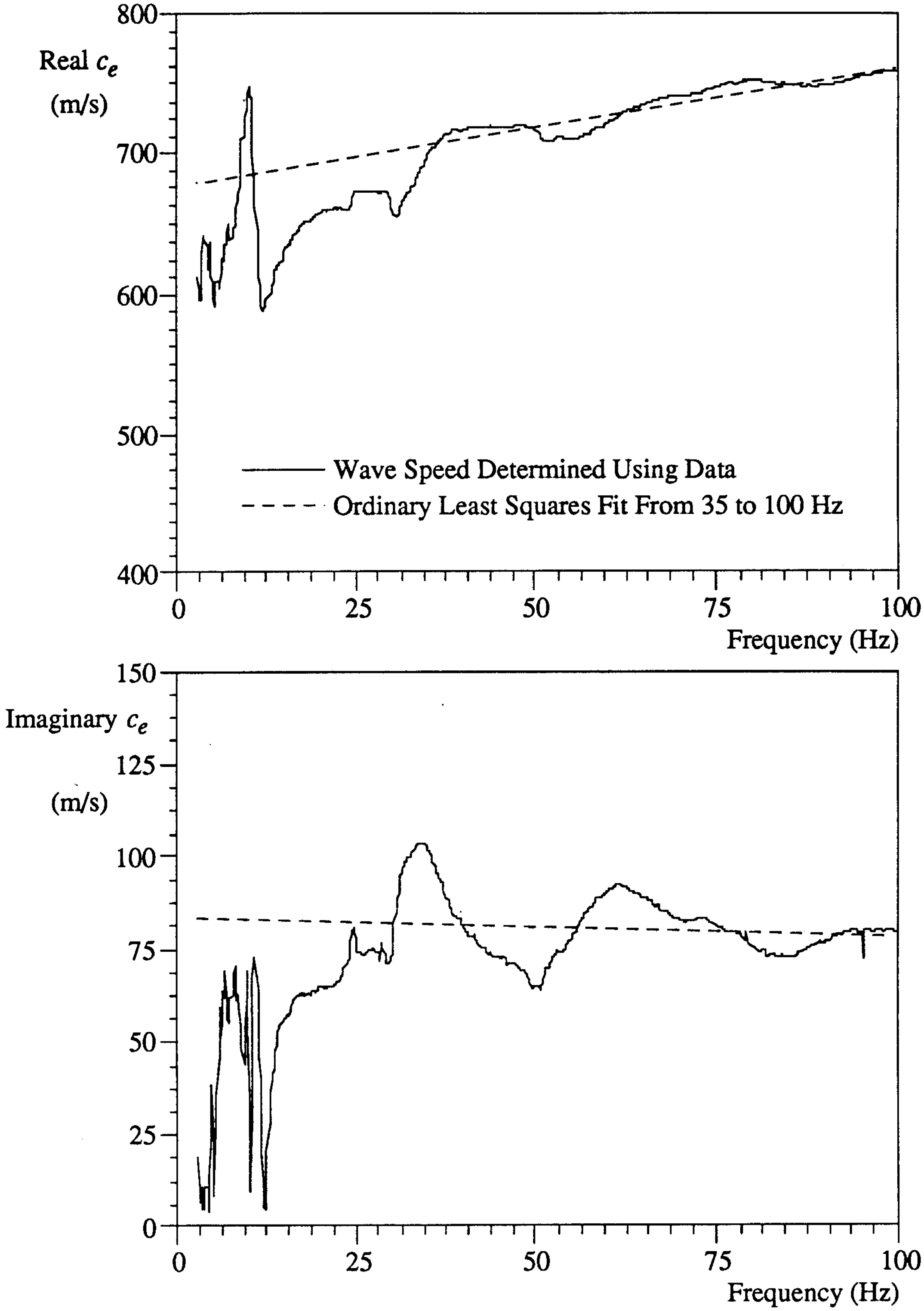

Figure 2. Extensional Wave Speed Versus Frequency

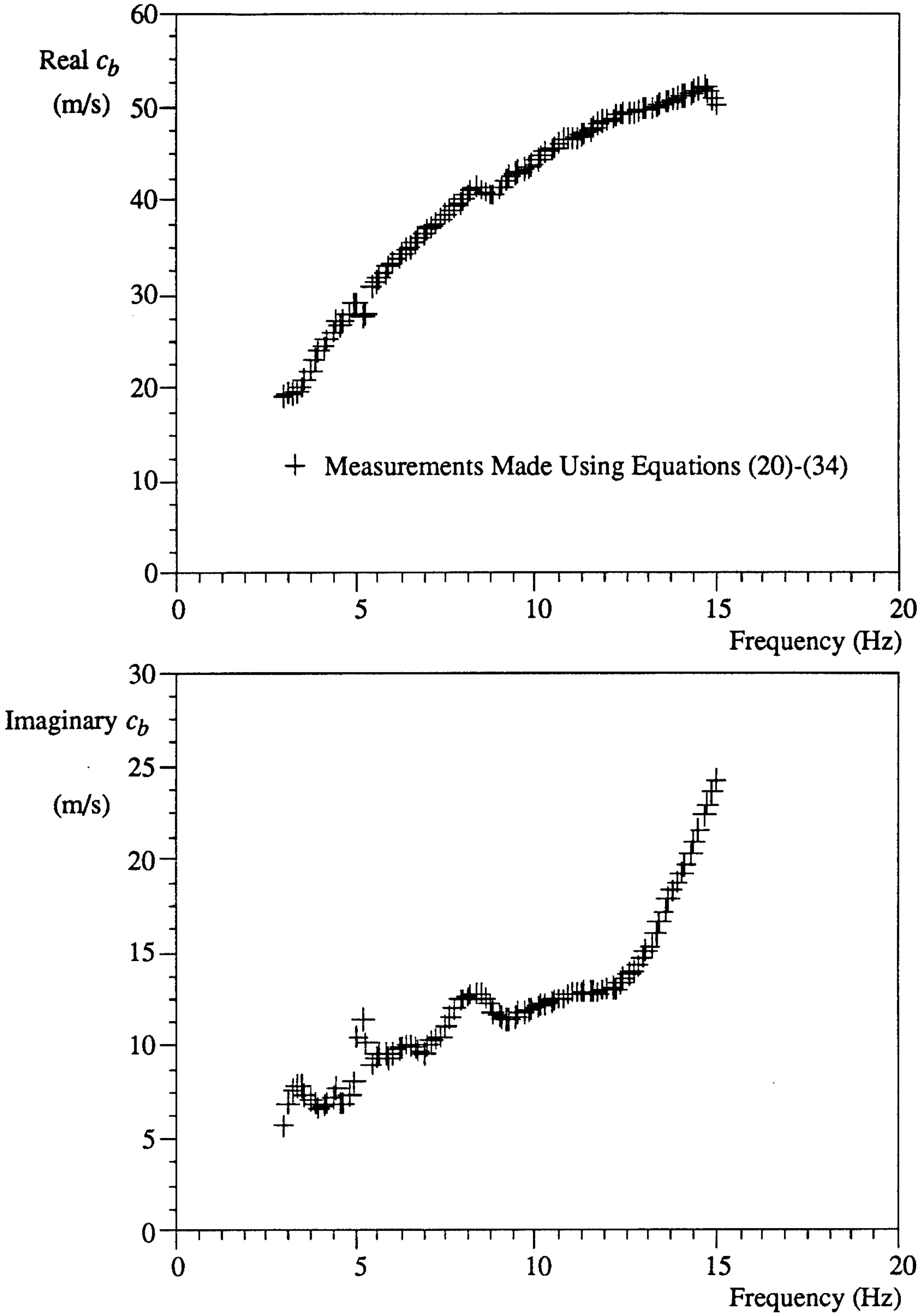

Figure 3. Breathing Wave Speed Versus Frequency

Once the extensional and breathing wave speeds are measured, equations (35)-(45) can be applied to the hydrophone data. Although four hydrophone measurements are sufficient to define the empirical pressure field, they are insufficient to verify the accuracy of the model. This is because the model (by definition) is equal to the four data points used to create it. To resolve the problem of determining the accuracy of the model, 12 hydrophones were placed in the shell and were spaced at intervals of 0.5 m with a distance of 3.0 m from the forward end of the shell to the first hydrophone. The coherence versus frequency plots for each hydrophone measurement are included in appendix A. The signal-to-noise ratio of each hydrophone and the forward accelerometer were approximately 60 dB. The models were fit using two different variations of equation (6): the first included the $A(\omega)$ term and is referred to as the four-term model and the second omitted the $A(\omega)$ term and is referred to as the three-term model. This $A(\omega)$ term corresponds to the breathing wave pressure generated by the aft bulkhead of the shell. The effect of this model variation is discussed below.

Figures 4, 5, 6, and 7 are plots of the data and two models of the pressure field versus distance at 5.4, 12.7, 32.1, and 61.2 Hz, respectively. The pressure field versus distance at 41 different frequencies is included in appendix B. The (pressure field) models were created using the direct inverse method (equations (35)-(40)). The solid line represents the pressure field including the $A(\omega)$ term and is based on the spatial locations corresponding to the first (x_1 = 3.0 m), fourth (x_2 = 4.5 m), eighth (x_3 = 6.5 m), and twelfth (x_4 = 8.5 m) hydrophone sensors. The dashed line shows the pressure field excluding the $A(\omega)$ term and is based on the spatial locations corresponding to the first (x_2 = 3.0 m), sixth (x_3 = 5.5 m), and twelfth (x_4 = 8.5 m) hydrophone sensors. The x_1 location is not used for the three-term model because it corresponds to the $A(\omega)$ term. The extensional wave speeds used in deriving both models were determined from figure 2, and the breathing wave speeds from figure 3. For the region above 15 Hz, the breathing wave speed was extrapolated.

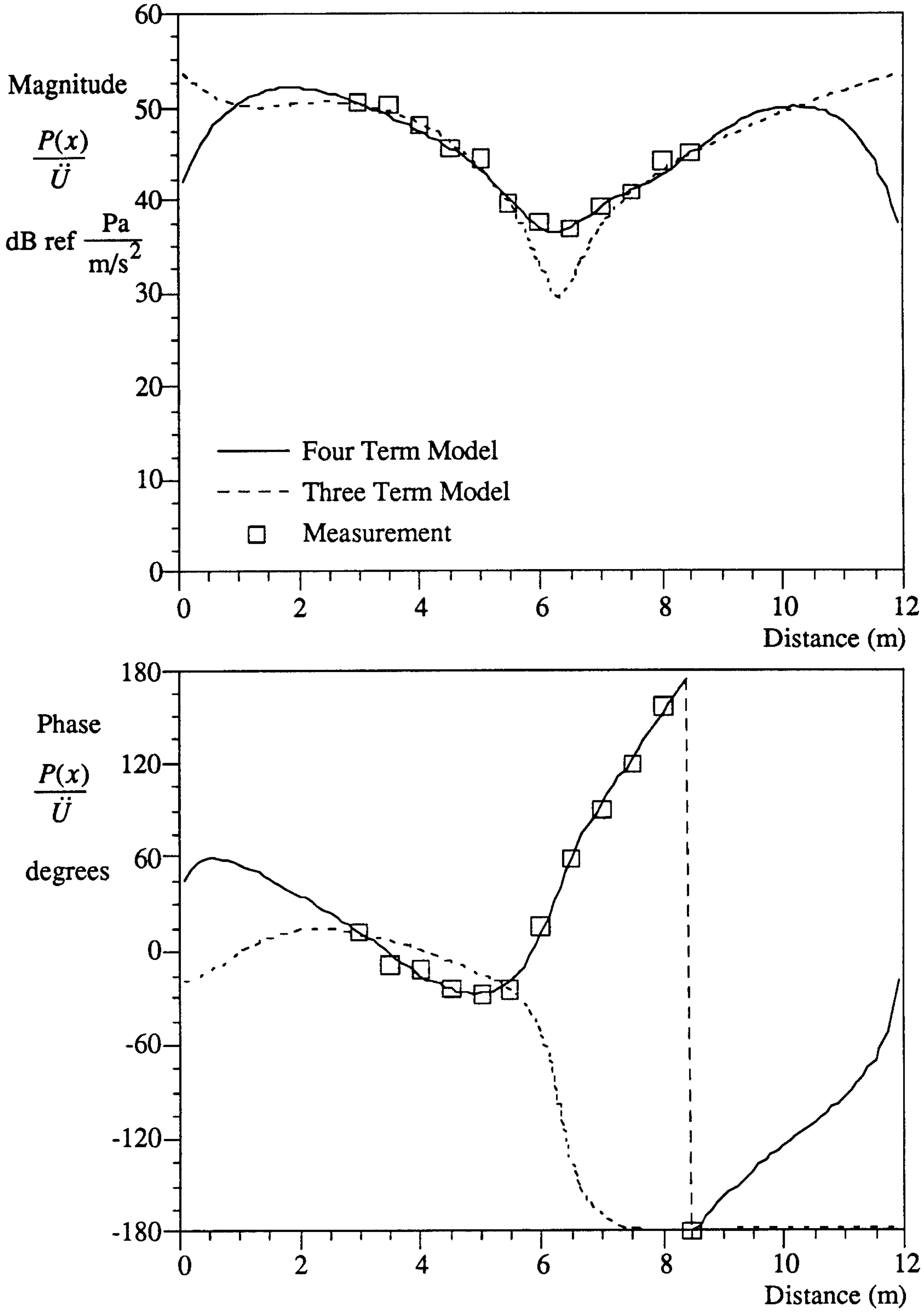

Figure 4. Pressure Field Versus Distance at 5.4 Hz With Model Determined Using the Direct Inverse Method

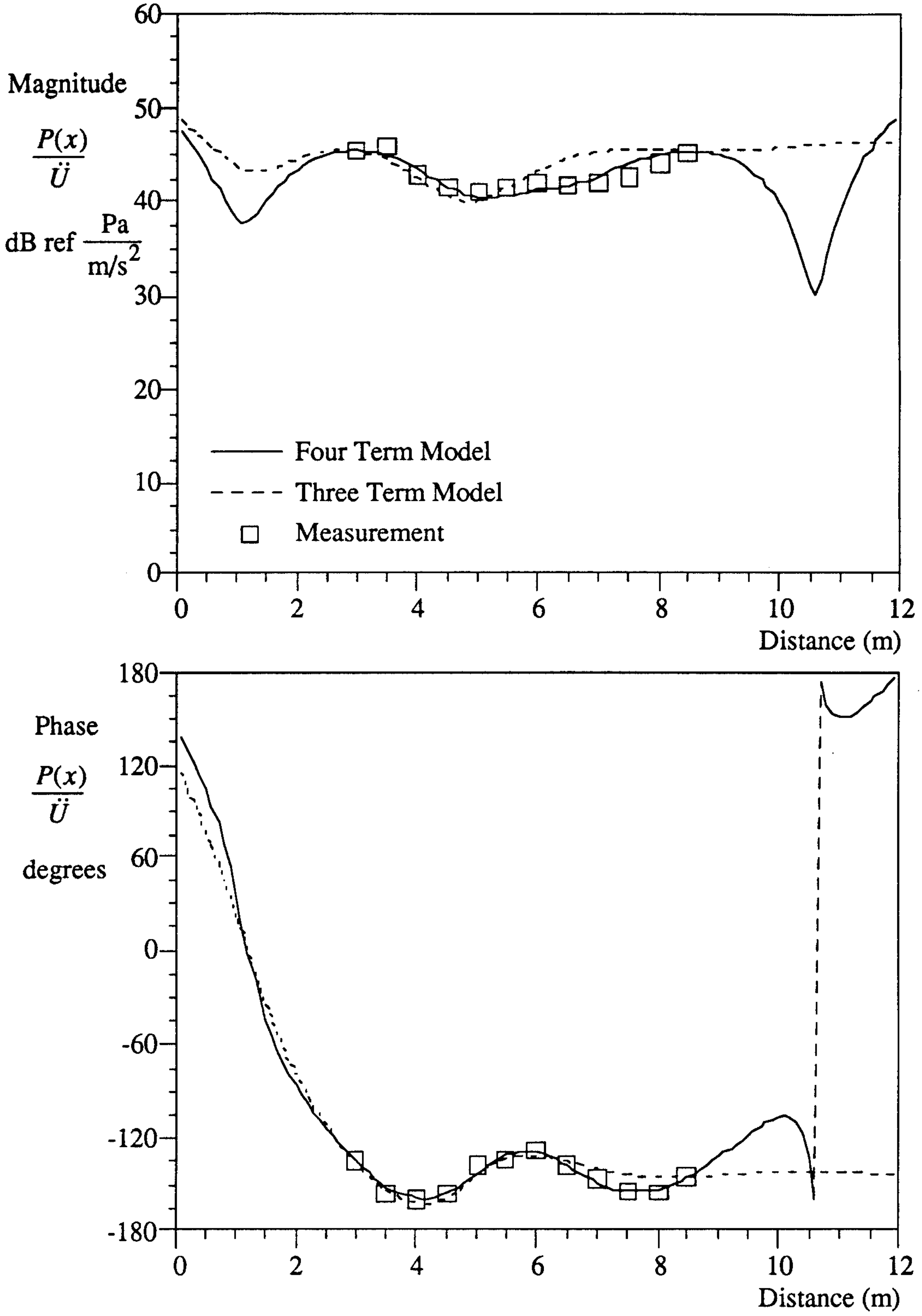

Figure 5. Pressure Field Versus Distance at 12.7 Hz With Model Determined Using the Direct Inverse Method

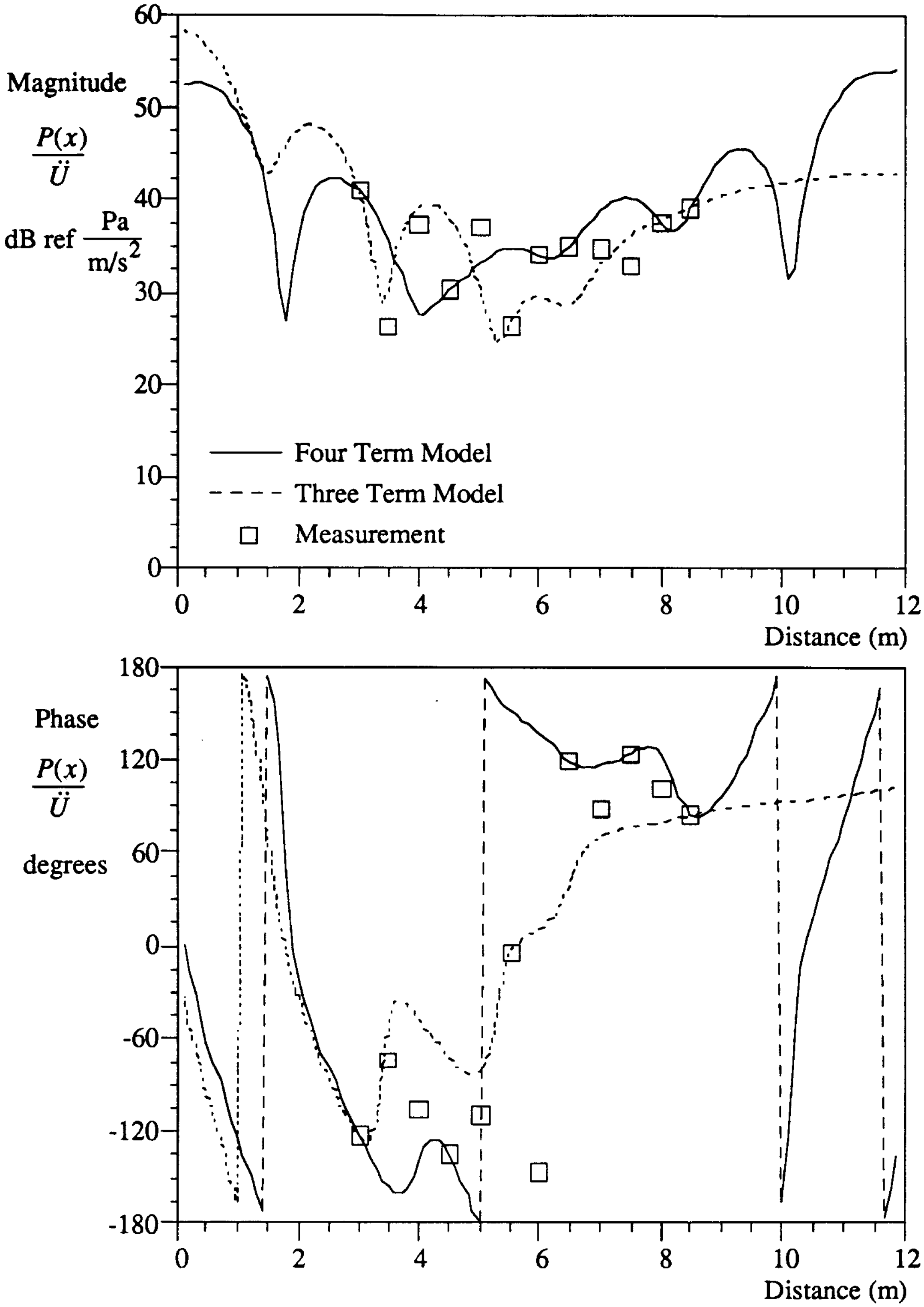

Figure 6. Pressure Field Versus Distance at 32.1 Hz With Model Determined Using the Direct Inverse Method

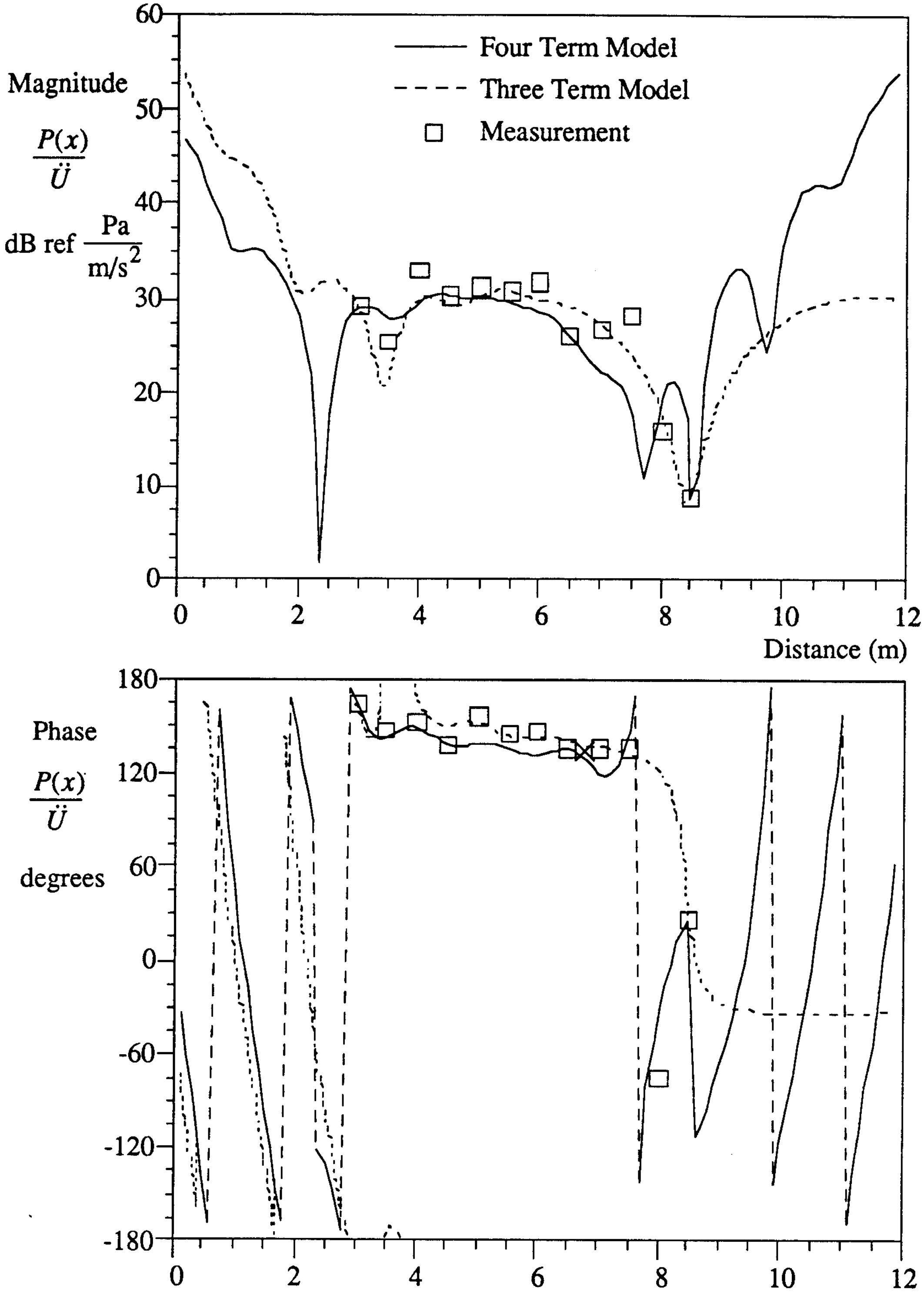

Figure 7. Pressure Field Versus Distance at 61.2 Hz With Model Determined Using the Direct Inverse Method

Figures 8, 9, 10, and 11 are plots of the data and two models of the pressure field versus distance at 5.4, 12.7, 32.1, and 61.2 Hz, respectively. The models were created using the Gauss linearization method (equations (41)-(45)). The solid line shows the pressure field including the $A(\omega)$ term and is based on all 12 hydrophone measurements. The dashed line depicts the pressure field excluding the $A(\omega)$ term and is also based on all 12 hydrophone measurements. The extensional wave speeds used in creating the model were determined from figure 2, and the breathing wave speeds from figure 3. For the region above 15 Hz, the breathing wave speed was extrapolated. Due to the similarity of the Gauss linearization method to the direct inverse method, no additional plots of the Gauss linearization method are included.

The four different variations of the model were all computed and compared to the data. The formula used for this comparison, in decibels, was

$$\beta(\omega) = 20 \log_{10}\left(\frac{1}{N}\right)\sum_{i=1}^{N}\left|\frac{|h_i(\omega)| - |y_i(\omega)|}{\bar{y}(\omega)}\right| , \tag{46}$$

where

$$\bar{y}(\omega) = \frac{1}{N}\sum_{i=1}^{N}|y_i(\omega)| . \tag{47}$$

The term i is the ith member of the corresponding vector and N is the total number of measurements (N = 12). The average difference between the models and the measurements (equation (46)) at various frequencies is listed in table 1.

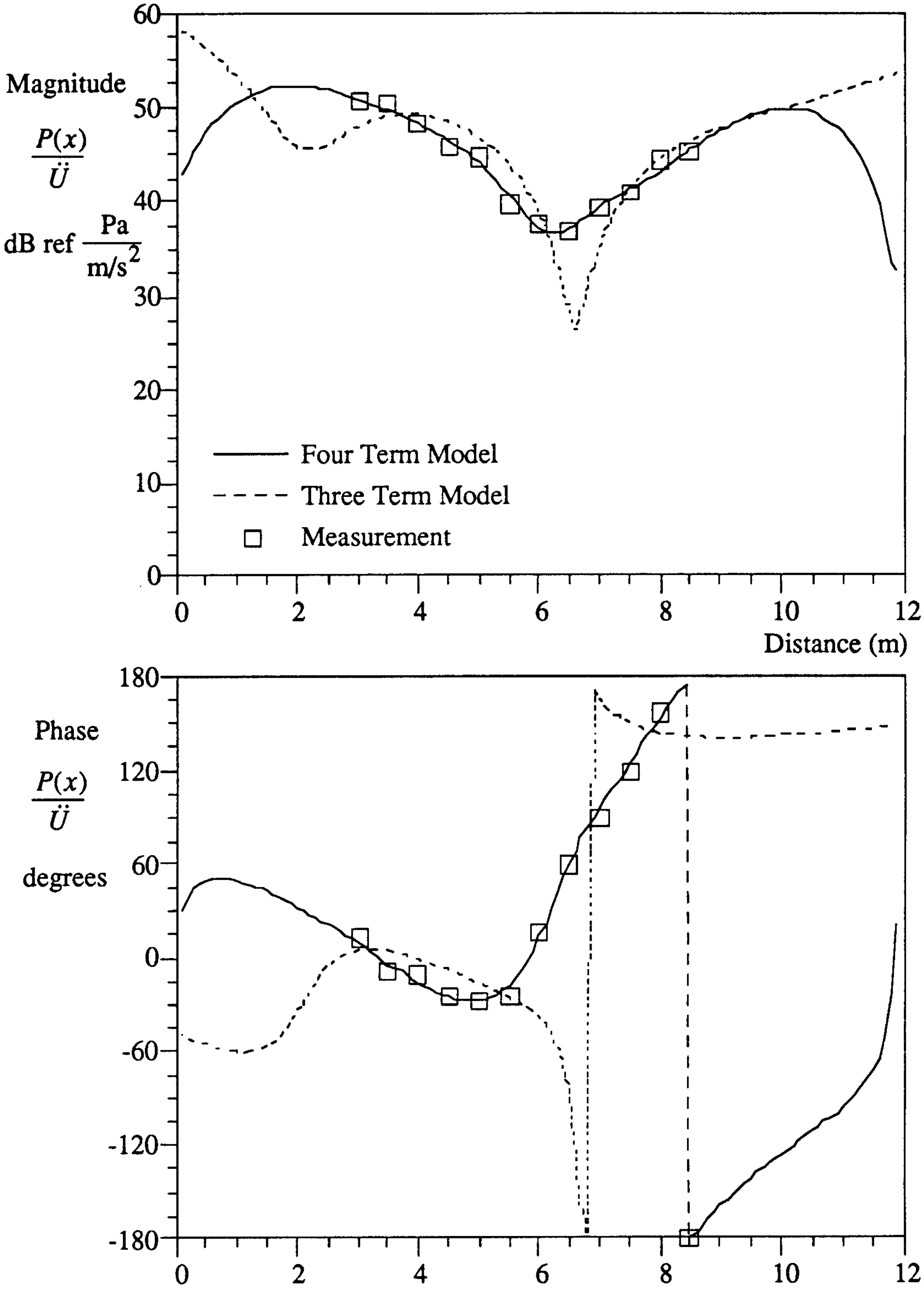

Figure 8. Pressure Field Versus Distance at 5.4 Hz With Model Determined Using the Gauss Linearization Method

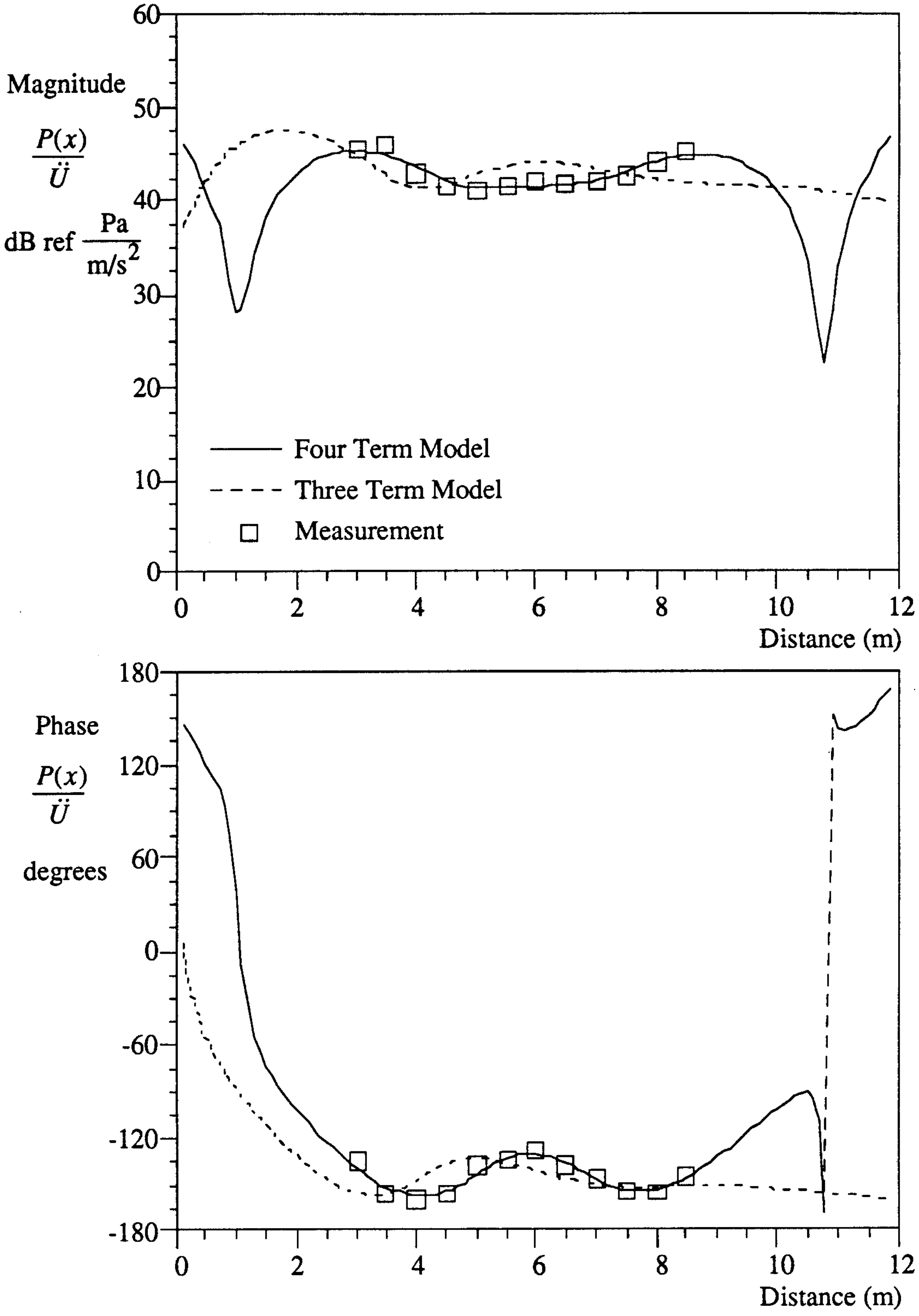

Figure 9. Pressure Field Versus Distance at 12.7 Hz With Model Determined Using the Gauss Linearization Method

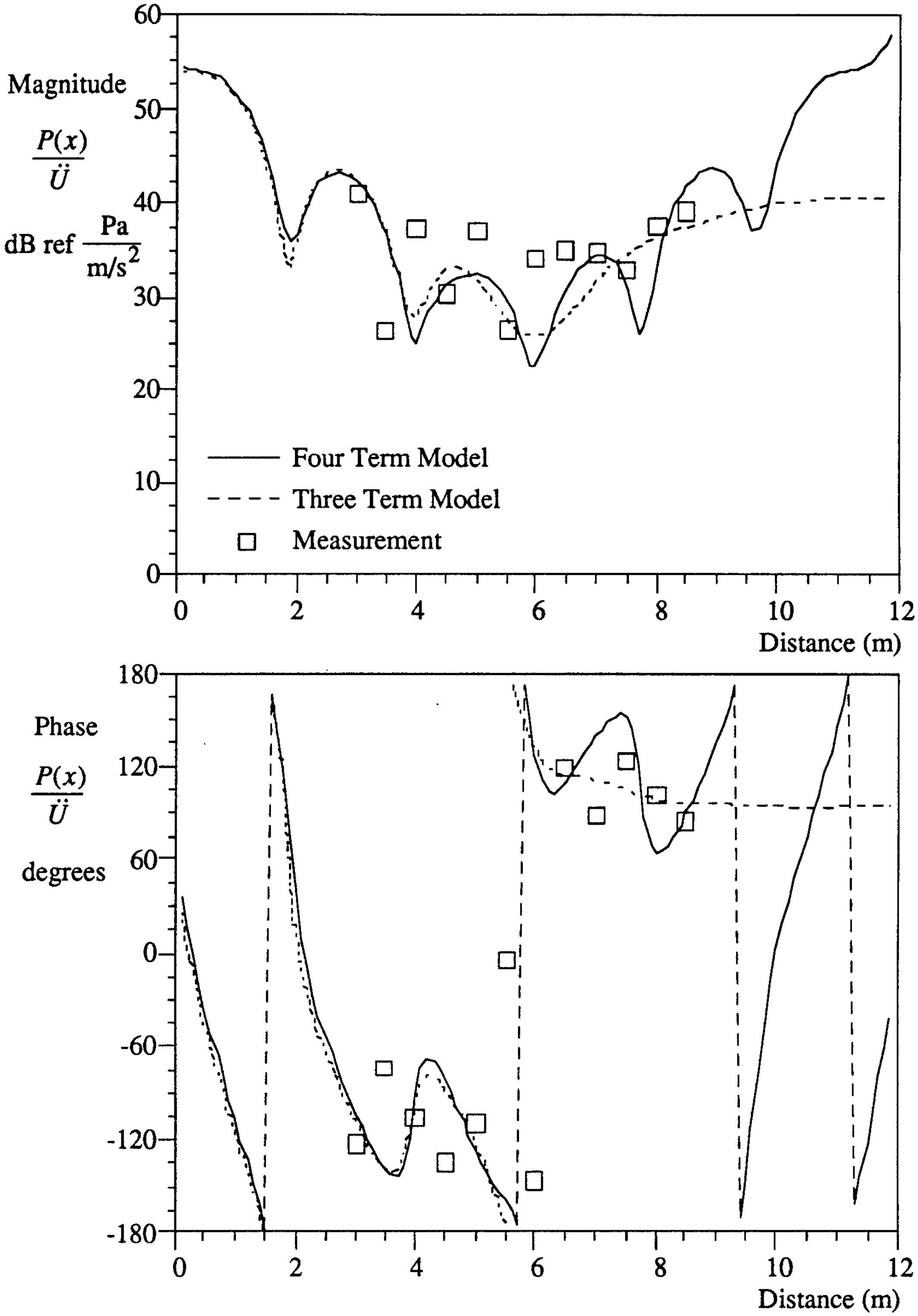

Figure 10. Pressure Field Versus Distance at 32.1 Hz With Model Determined Using the Gauss Linearization Method

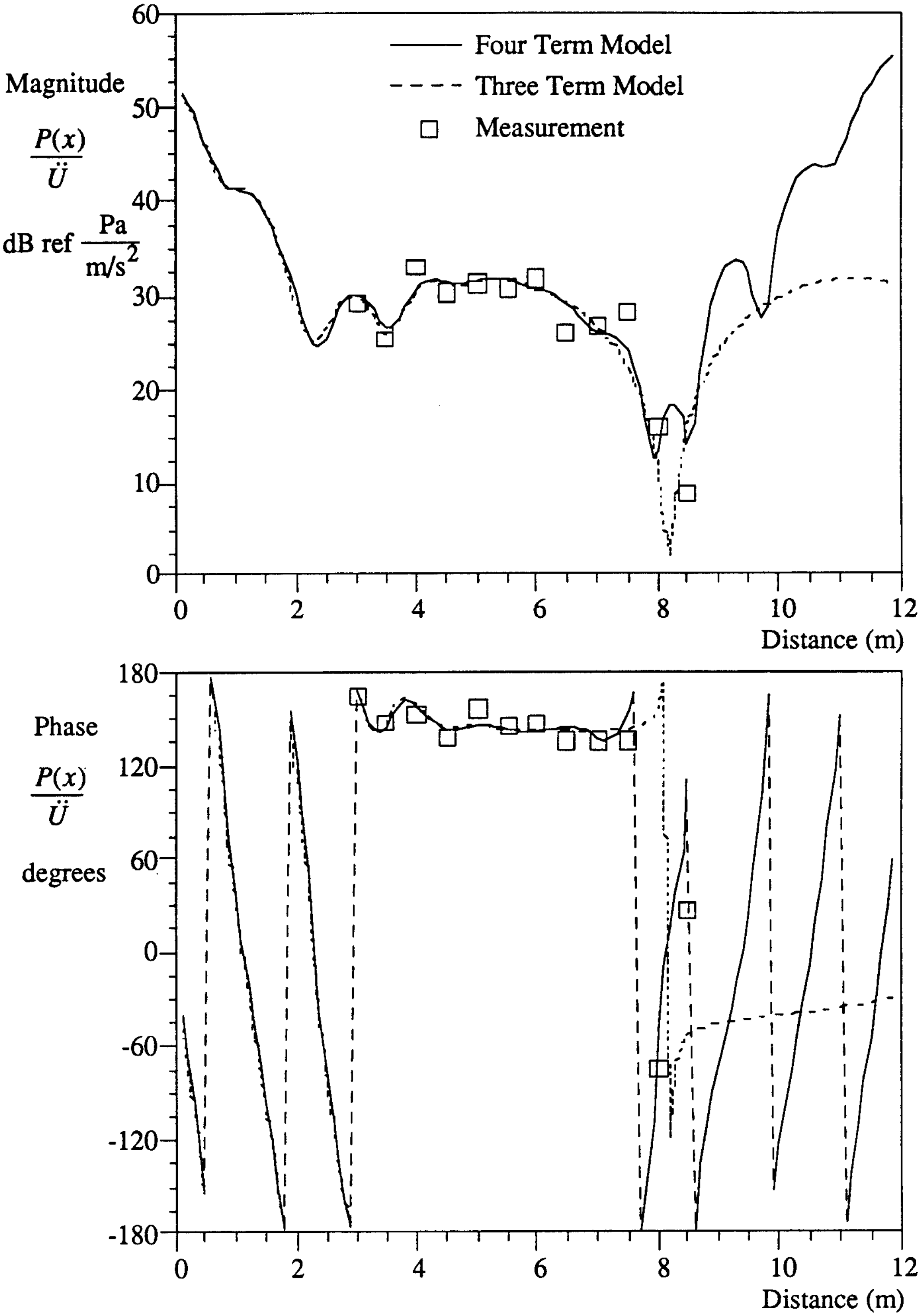

Figure 11. Pressure Field Versus Distance at 61.2 Hz With Model Determined Using the Gauss Linearization Method

Table 1. Average Difference Between Model and Measurement in Decibels

Frequency	Direct Inverse Method		Gauss Linearization Method	
(Hz)	4 Term	3 Term	4 Term	3 Term
3.0	0.6	0.8	0.6	1.0
5.4	0.5	0.8	0.5	2.3
7.9	0.4	1.1	0.4	1.4
10.3	0.2	0.7	0.3	2.4
12.7	0.6	1.4	0.4	1.8
15.1	0.5	1.2	3.3	0.7
17.5	1.2	0.9	3.2	1.5
20.0	1.0	1.4	2.1	2.5
22.4	0.9	2.5	3.7	2.1
24.8	0.9	4.2	2.3	2.5
27.2	1.2	3.7	2.0	2.4
29.7	2.2	3.2	3.1	3.5
32.1	3.6	3.0	4.8	4.4
34.5	4.0	2.6	6.3	3.9
37.0	5.1	2.5	4.5	3.0
39.4	6.9	2.5	3.5	2.7
41.8	4.8	2.1	2.8	2.1
44.2	3.9	1.8	2.2	2.0
46.7	3.3	1.7	2.1	2.5
49.1	3.1	1.8	2.4	2.6
51.5	2.9	2.0	2.4	2.6
53.9	2.7	2.1	2.4	2.7
56.3	2.7	2.3	2.5	2.8
58.8	2.2	2.0	1.9	2.2
61.2	2.3	1.7	1.7	1.7
63.6	2.5	1.8	1.9	1.8
66.1	2.4	1.9	2.0	1.7
68.5	2.3	1.9	1.8	1.7

Table 1. Average Difference Between Model and Measurement in Decibels (Cont'd)

Frequency	Direct Inverse Method		Gauss Linearization Method	
(Hz)	4 Term	3 Term	4 Term	3 Term
70.9	2.0	1.9	1.7	1.7
73.3	1.9	1.9	1.8	2.0
75.8	1.9	1.6	1.6	1.6
78.2	1.6	1.5	1.3	1.4
80.6	1.7	1.1	1.3	1.3
83.0	1.3	1.5	1.4	1.5
85.4	1.4	2.2	1.9	2.1
87.9	1.5	3.0	2.2	2.4
90.3	1.8	4.1	2.5	2.6
92.7	1.7	3.4	2.5	2.5
95.2	2.2	3.2	2.6	2.6
97.6	2.1	3.3	2.6	2.7
100.0	1.8	3.2	2.6	2.7

The four-term models are extremely accurate from 3 to approximately 13 Hz. At 13 Hz, the Gauss linearization method begins to diverge from the direct inverse method. The direct inverse method is still accurate up to approximately 27 Hz. From 27 to 50 Hz, there is a difference of about 4 dB between the experiment and both models. Because the models are being defined by the experimental values and the coherence of the measurements are almost unity, this difference is larger than expected. There could be a number of reasons why this divergence occurs:

- A transverse wave is introducing unmodeled energy into the measurements.
- The wave speeds are not consistent across the length of the module.
- The hydrophones themselves are creating significant breathing wave energy sources in this frequency range.

- The transverse support lines are a noise source.
- The spatial coherence length of the breathing wave generated at the aft bulkhead is causing a situation where some breathing wave energy is being input into the aft hydrophones but not into the forward ones, which creates an inconsistent model.
- Nonaxisymmetric effects of wave motion are being detected by the hydrophones.
- The hydrophone mounts are transmitting unmodeled energy into the hydrophones.

The models above 50 Hz have a difference from the measured values of about 2 dB. This is considered borderline for accuracy in this particular experiment.

In the region above 50 Hz, the four-term models may be more accurate; however, they are creating pressure levels that are too high in the spatial region around the aft bulkhead. Additionally, the phase angle associated with these models at the aft bulkhead is incorrect in this frequency range, which is why the three-term models are included in the analysis. Because the three-term models assume only a single-direction breathing wave moving from the forward bulkhead to the aft end of the shell, they correspond more closely to the physics of the problem in the higher frequency range, even though the average difference between measurement and model may be greater than that of the four-term models.

6. CONCLUSIONS AND RECOMMENDATIONS

A two-wave empirical model of the pressure field in a liquid-filled cylindrical shell can be derived based on four hydrophone measurements in the liquid. Two comparably accurate methods were used to derive this pressure field: a direct inverse method and a Gauss linearization method. A three- and a four-term version of both methods was investigated. It was found that at the frequency range of 3 to 30 Hz, the four-term model was more accurate and in the frequency range of 50 to 100 Hz, the three-term model was more accurate. It is likely that an unmodeled noise source is contributing to the pressure field from 30 to 50 Hz.

The experiment should be rerun using shells of different diameter, stiffness, and length to determine if these model-to-experiment differences are shell dependent.

7. REFERENCES

1. P. W. Jameson, S. A. Africk, D. M. Chase, and E. C. H. Schmidt, "Investigation of Towed-Array Self-Noise Mechanisms by Analytical Models and Laboratory Experiments," Bolt, Beranek, and Newman, Inc., Report No. 2819, Cambridge, Massachusetts, 19 September 1974.

2. J. C. F. Chow and J. T. Apter, "Wave Propagation in a Viscous Incompressible Fluid Contained in Flexible Viscoelastic Tubes," *Journal of the Acoustical Society of America,* vol. 44, no. 2, pp. 437-443, 1968.

3. G. W. Morgan and J. P. Kiely, "Wave Propagation in a Viscous Liquid Contained in a Flexible Tube," *Journal of the Acoustical Society of America,* vol. 26, no. 3, pp. 323-328, May 1954.

4. A. J. Hull, "An Inverse Method to Measure the Axial Modulus of Composite Materials Under Tension," *Journal of Sound and Vibration* (To Be Published).

5. A. J. Hull, "An Inverse Method to Measure the Breathing Wave Speed in a Liquid-Filled Cylindrical Shell," NUWC-NPT Technical Report 11,093, Naval Undersea Warfare Center Detachment, New London, CT, 5 February 1996.

6. J. V. Beck and K. J. Arnold, *Parameter Estimation in Engineering and Science*, John Wiley & Sons, Inc., New York, 1977.

APPENDIX A - COHERENCE VERSUS FREQUENCY PLOTS

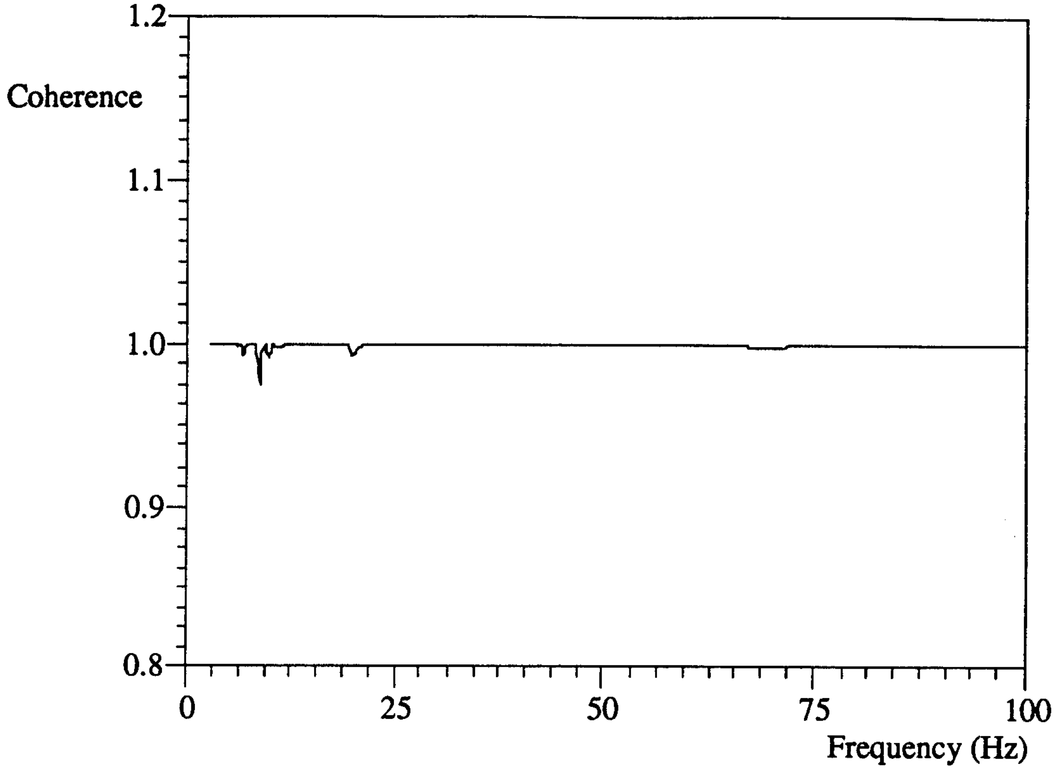

Figure A-1. Coherence Versus Frequency for Channel 1

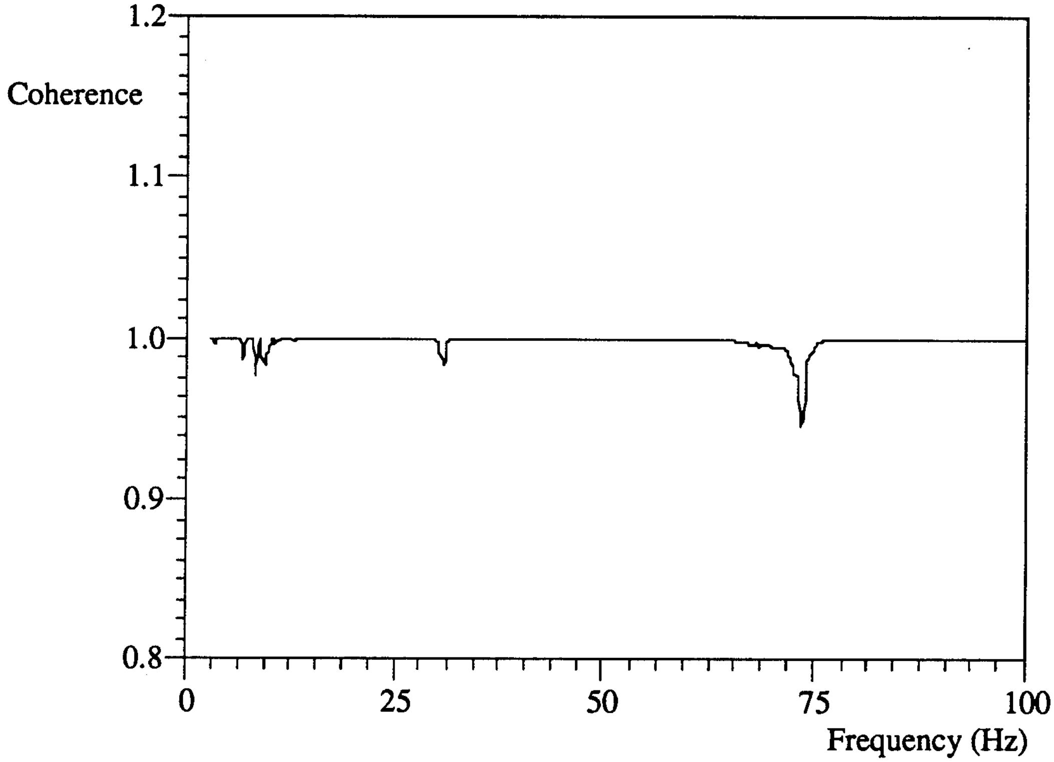

Figure A-2. Coherence Versus Frequency for Channel 2

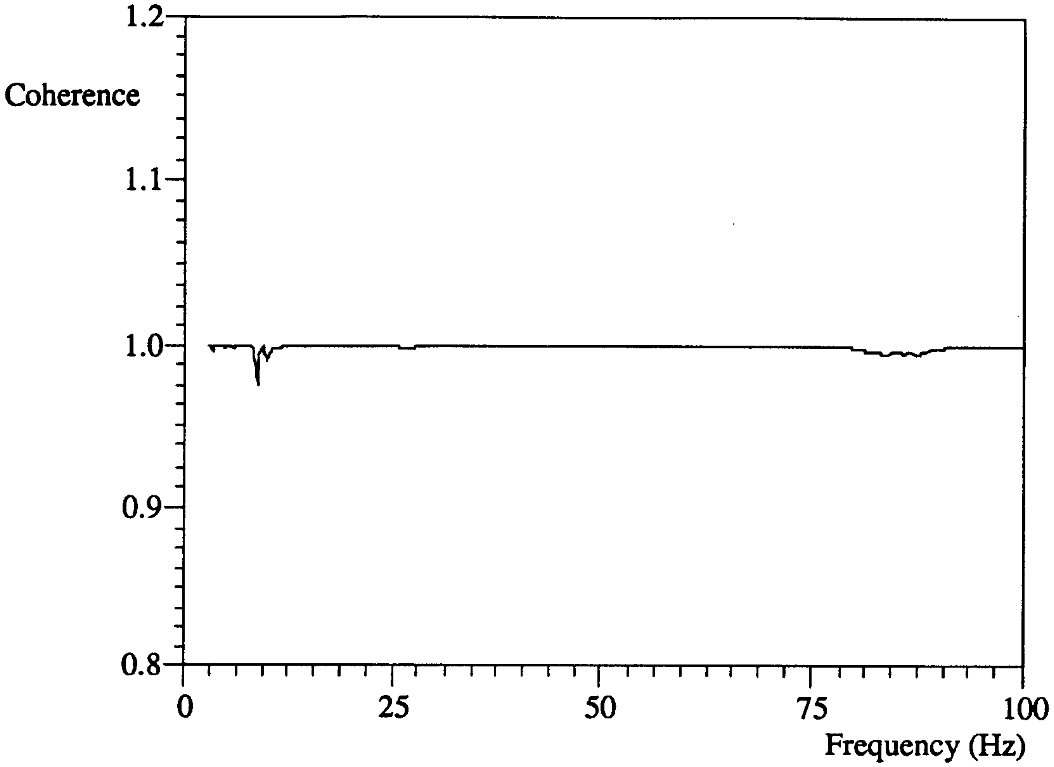

Figure A-3. Coherence Versus Frequency for Channel 3

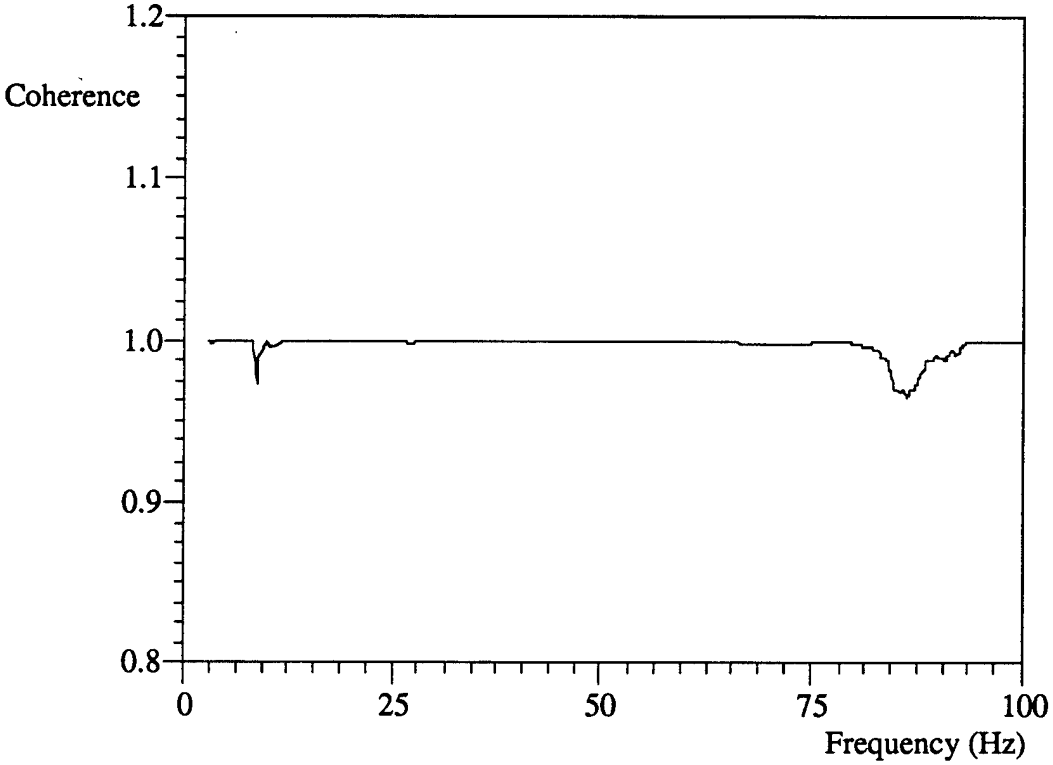

Figure A-4. Coherence Versus Frequency for Channel 4

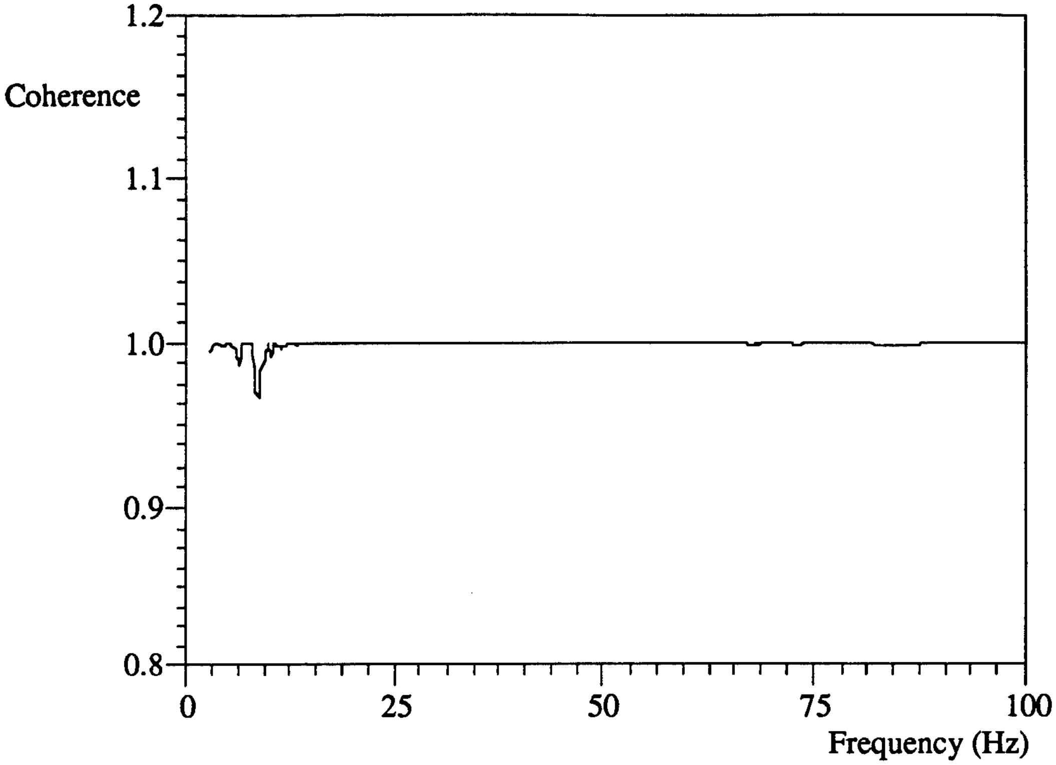

Figure A-5. Coherence Versus Frequency for Channel 5

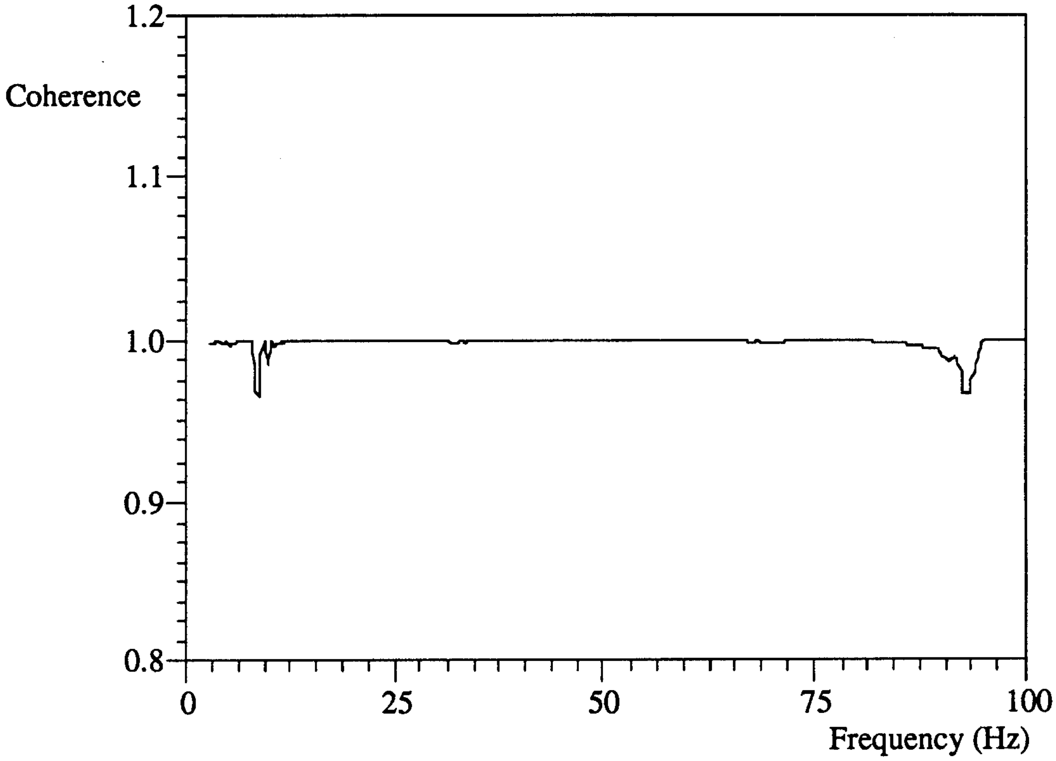

Figure A-6. Coherence Versus Frequency for Channel 6

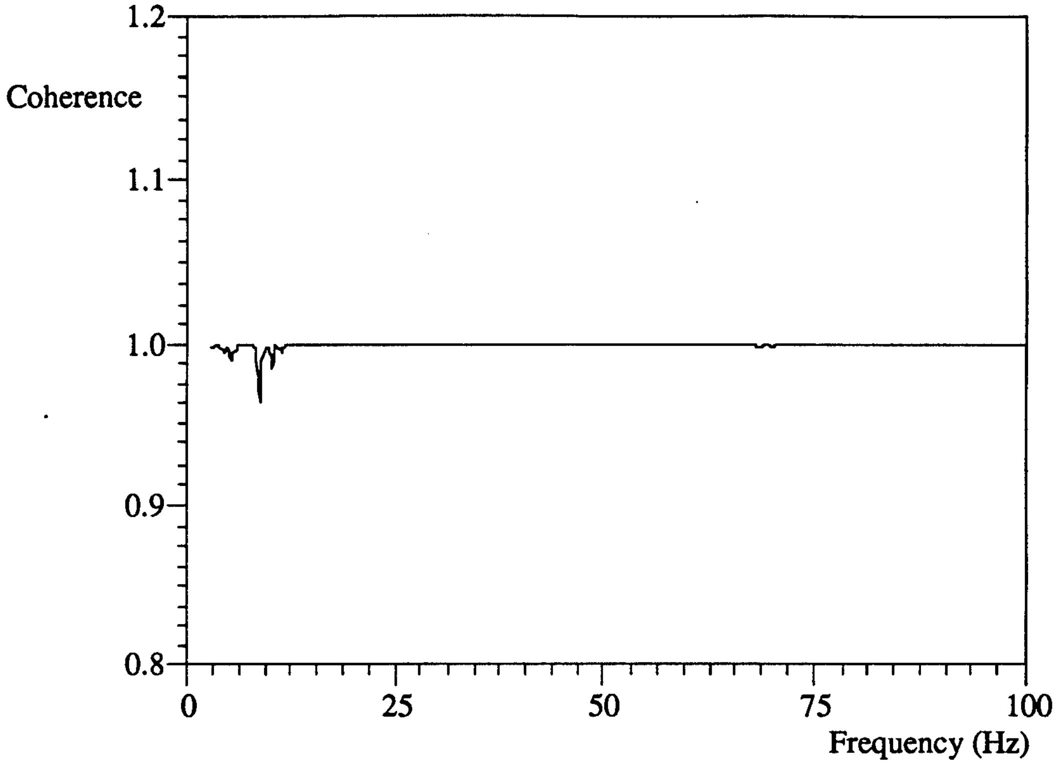

Figure A-7. Coherence Versus Frequency for Channel 7

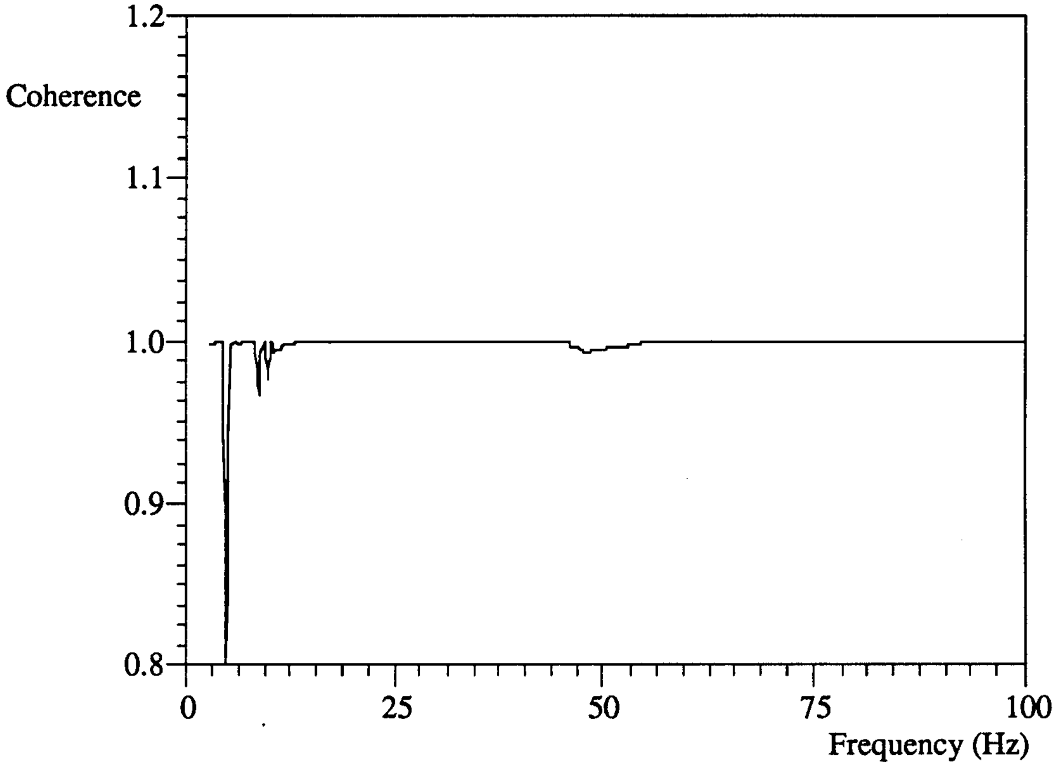

Figure A-8. Coherence Versus Frequency for Channel 8

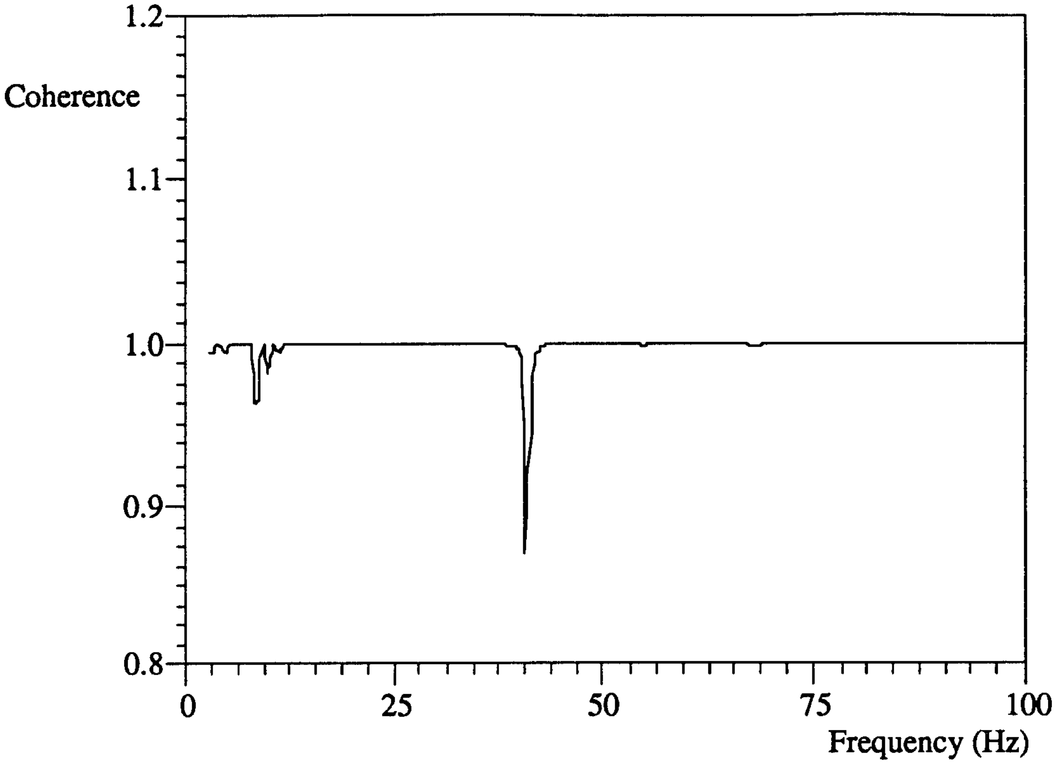

Figure A-9. Coherence Versus Frequency for Channel 9

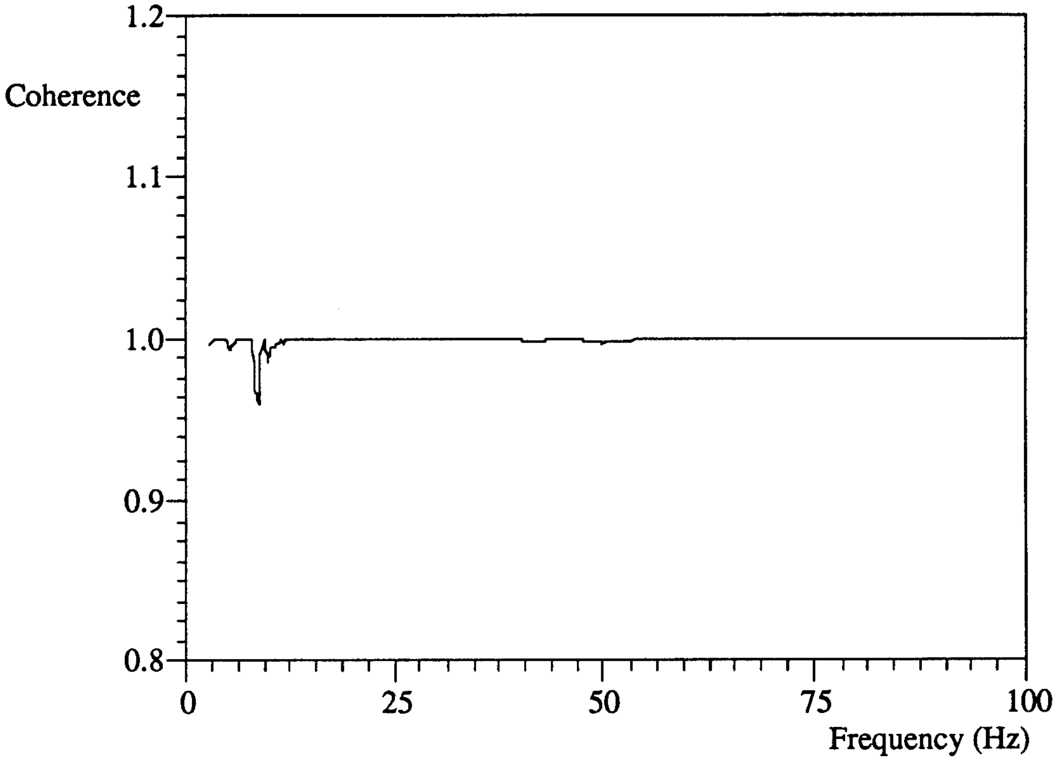

Figure A-10. Coherence Versus Frequency for Channel 10

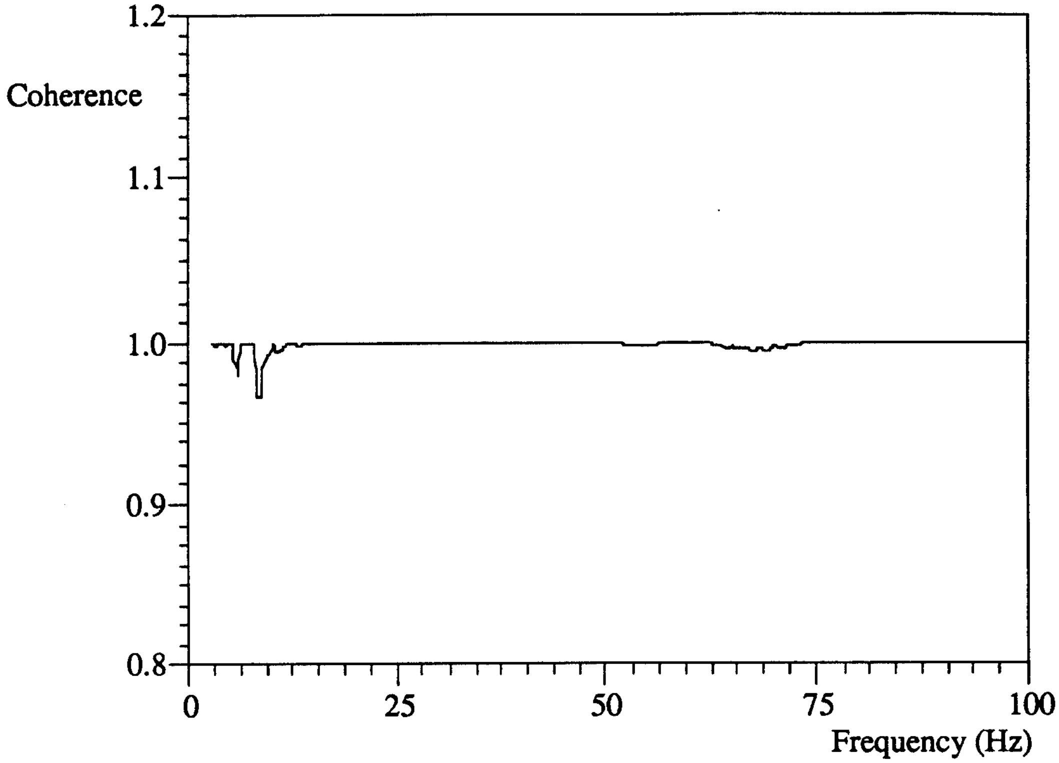

Figure A-11. Coherence Versus Frequency for Channel 11

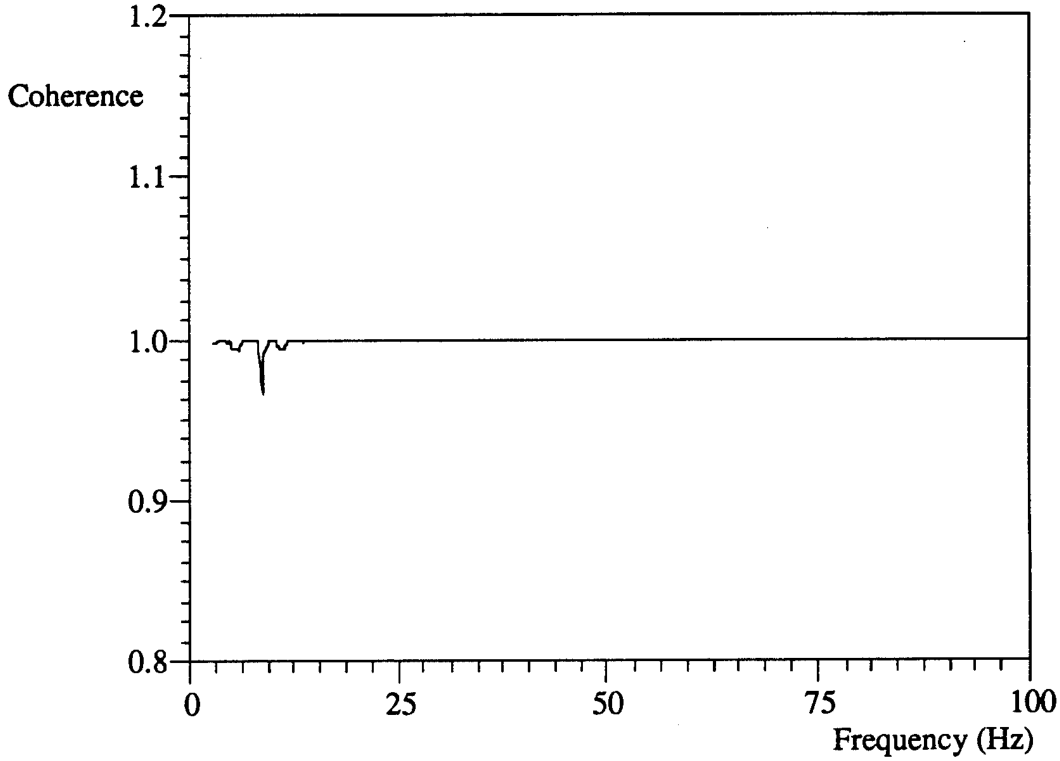

Figure A-12. Coherence Versus Frequency for Channel 12

APPENDIX B - PRESSURE FIELD VERSUS DISTANCE PLOTS

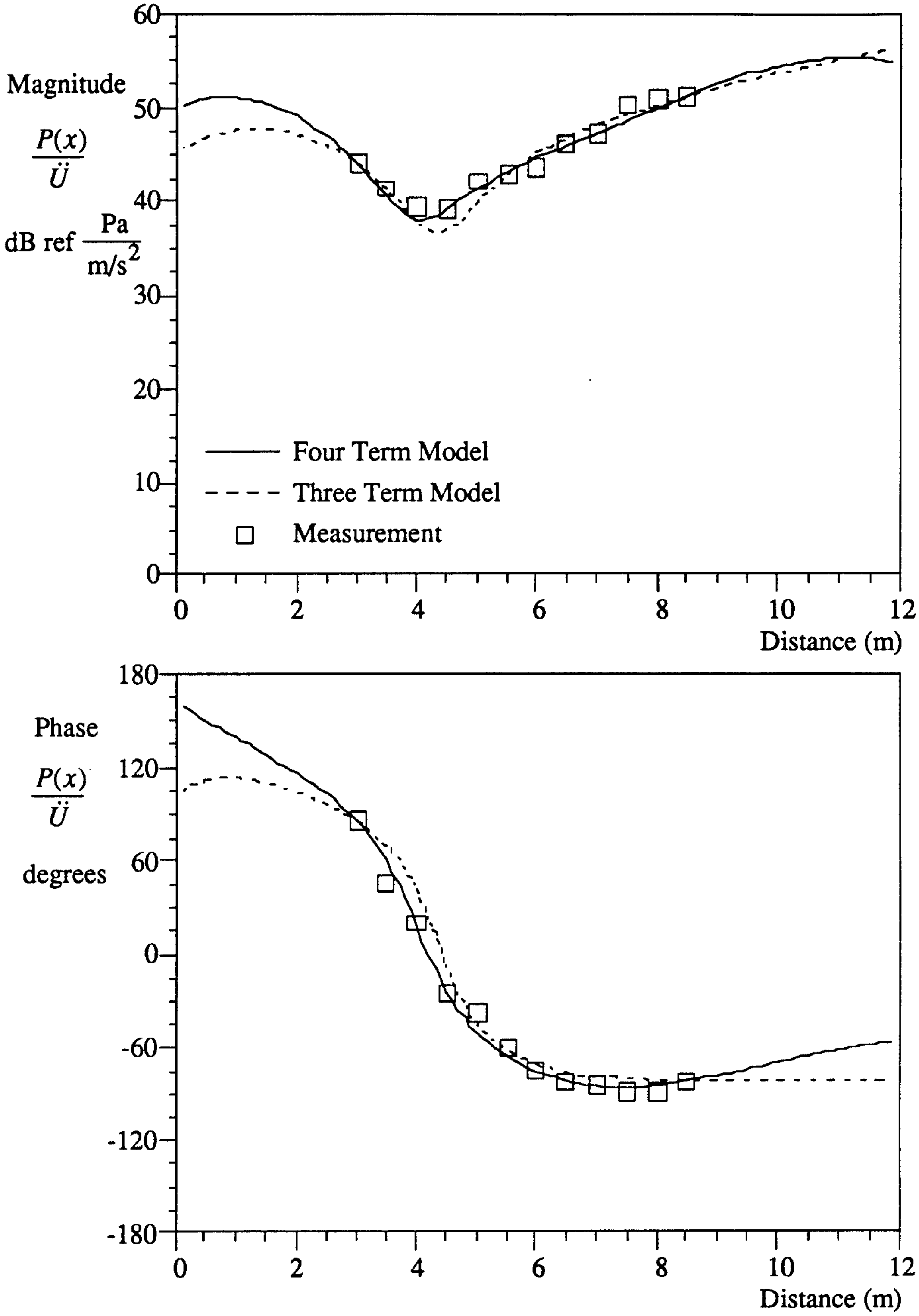

Figure B-1. Pressure Field Versus Distance at 3.0 Hz

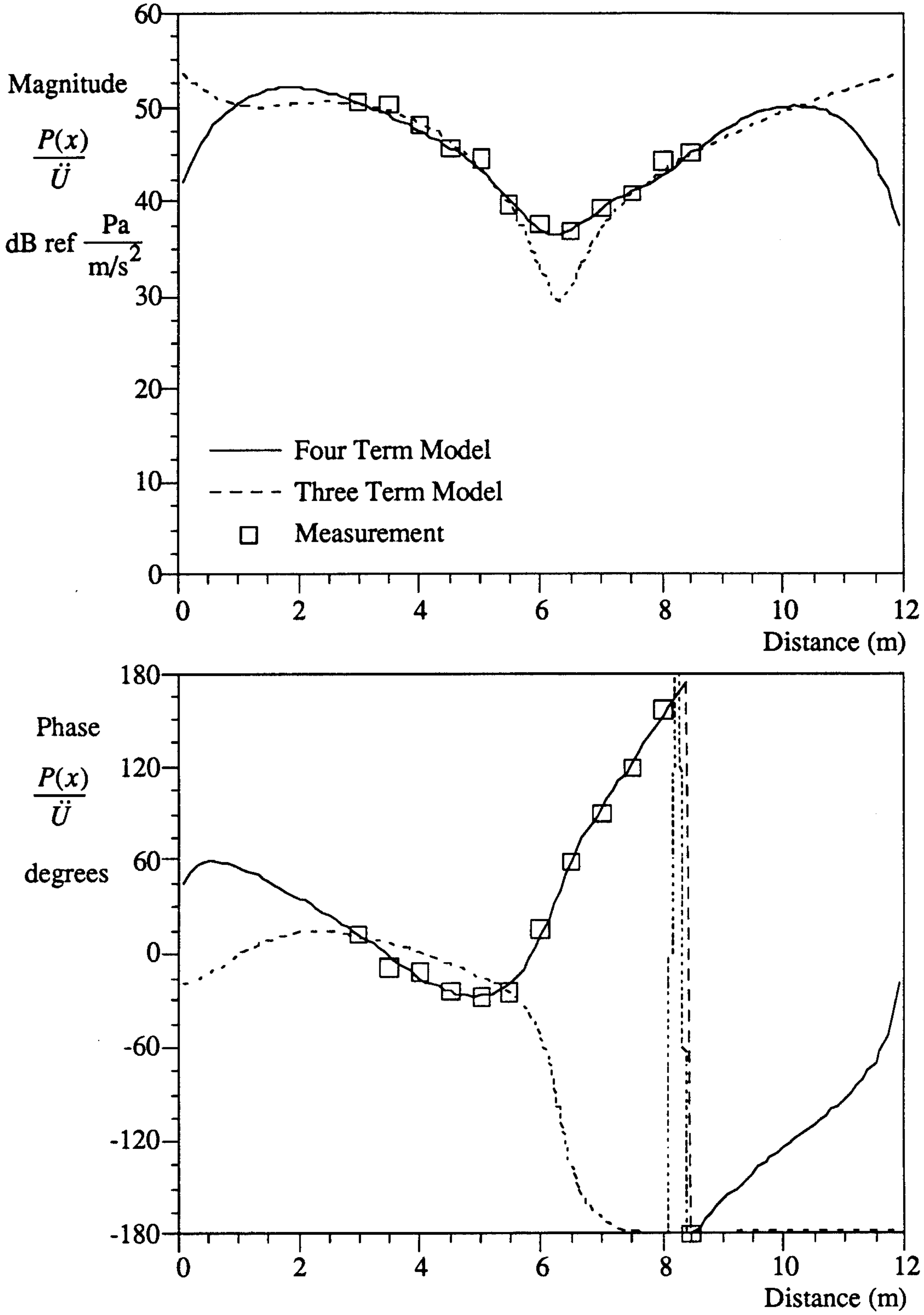

Figure B-2. Pressure Field Versus Distance at 5.4 Hz

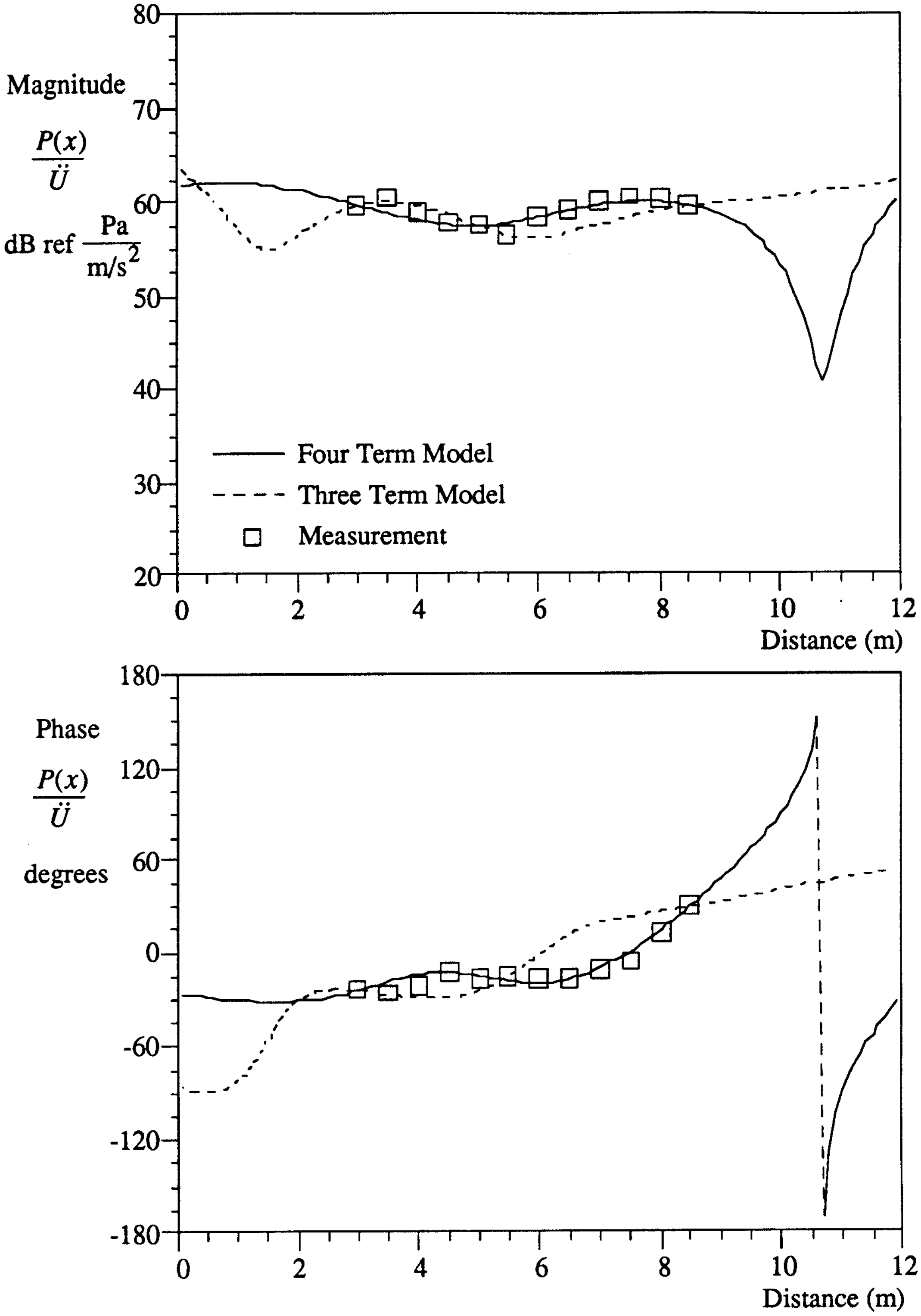

Figure B-3. Pressure Field Versus Distance at 7.9 Hz

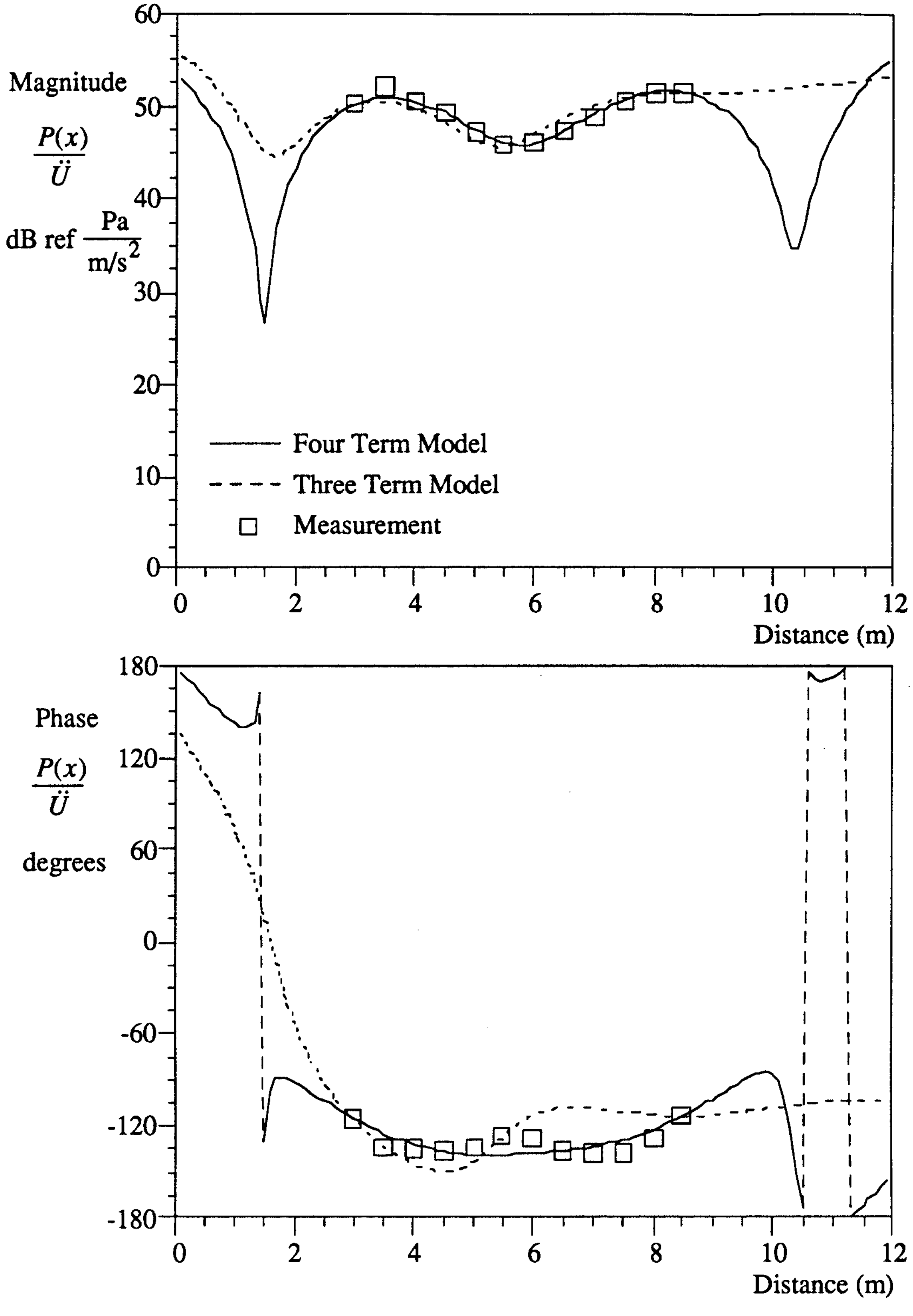

Figure B-4. Pressure Field Versus Distance at 10.3 Hz

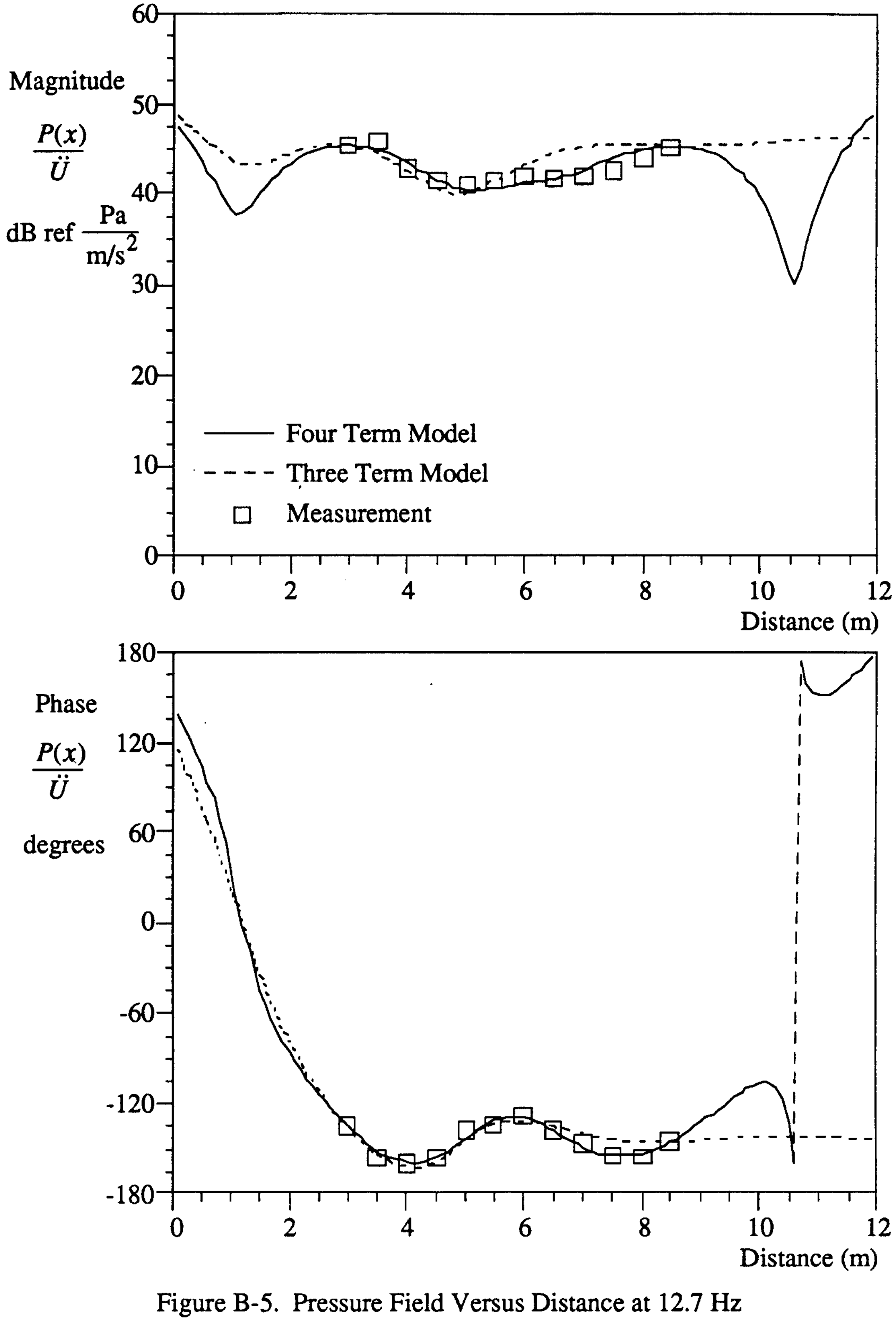

Figure B-5. Pressure Field Versus Distance at 12.7 Hz

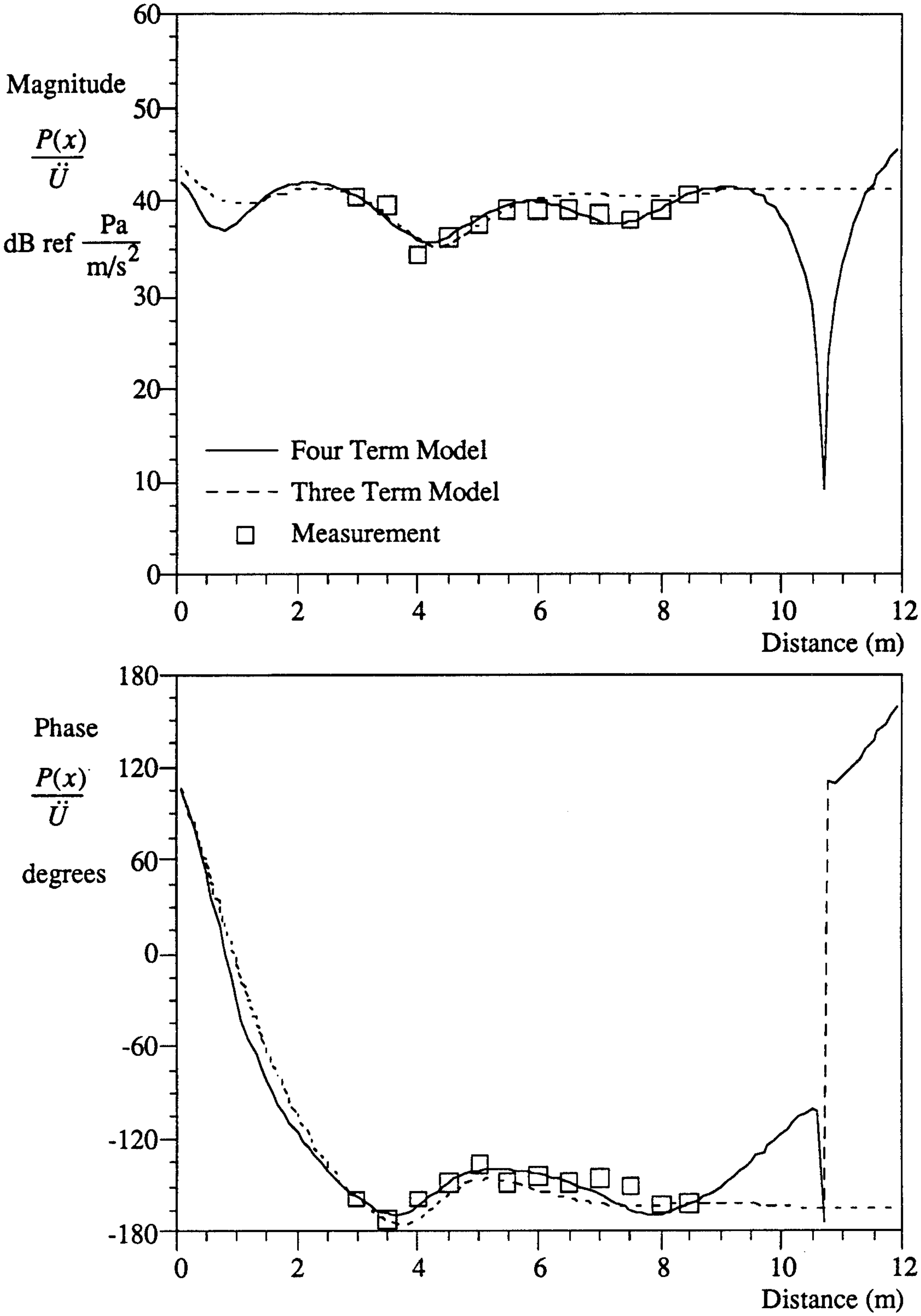

Figure B-6. Pressure Field Versus Distance at 15.1 Hz

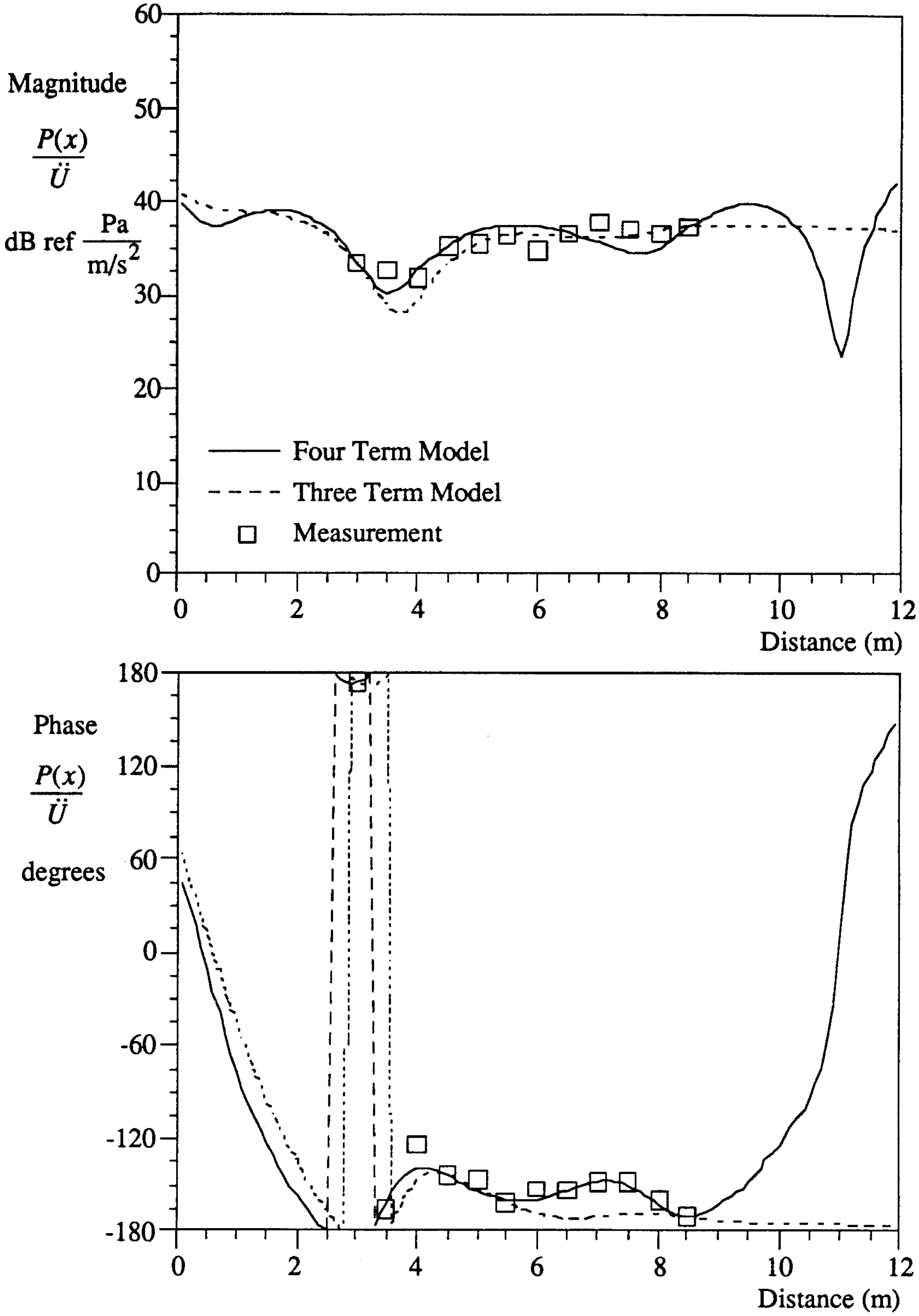

Figure B-7. Pressure Field Versus Distance at 17.6 Hz

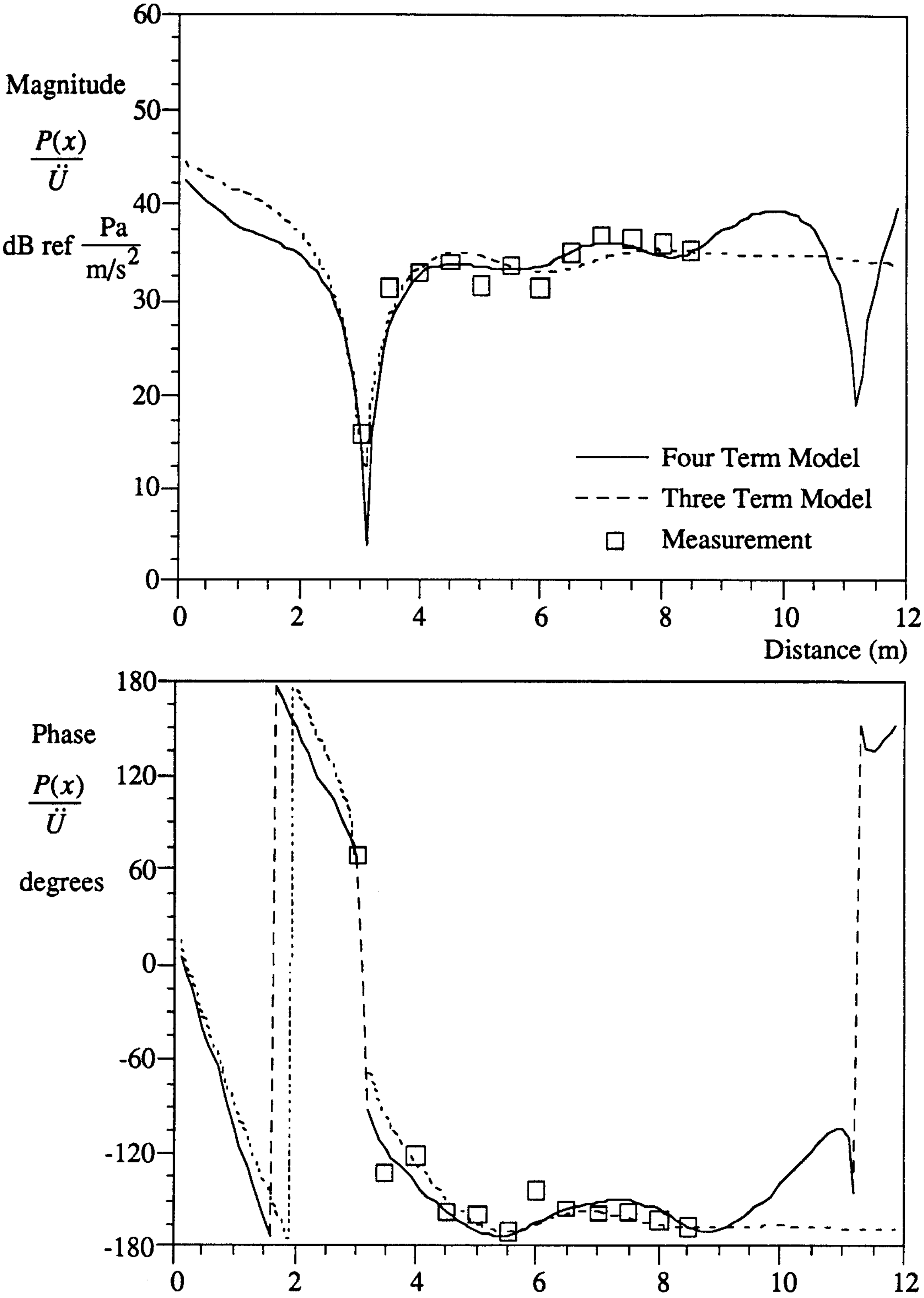

Figure B-8. Pressure Field Versus Distance at 20.0 Hz

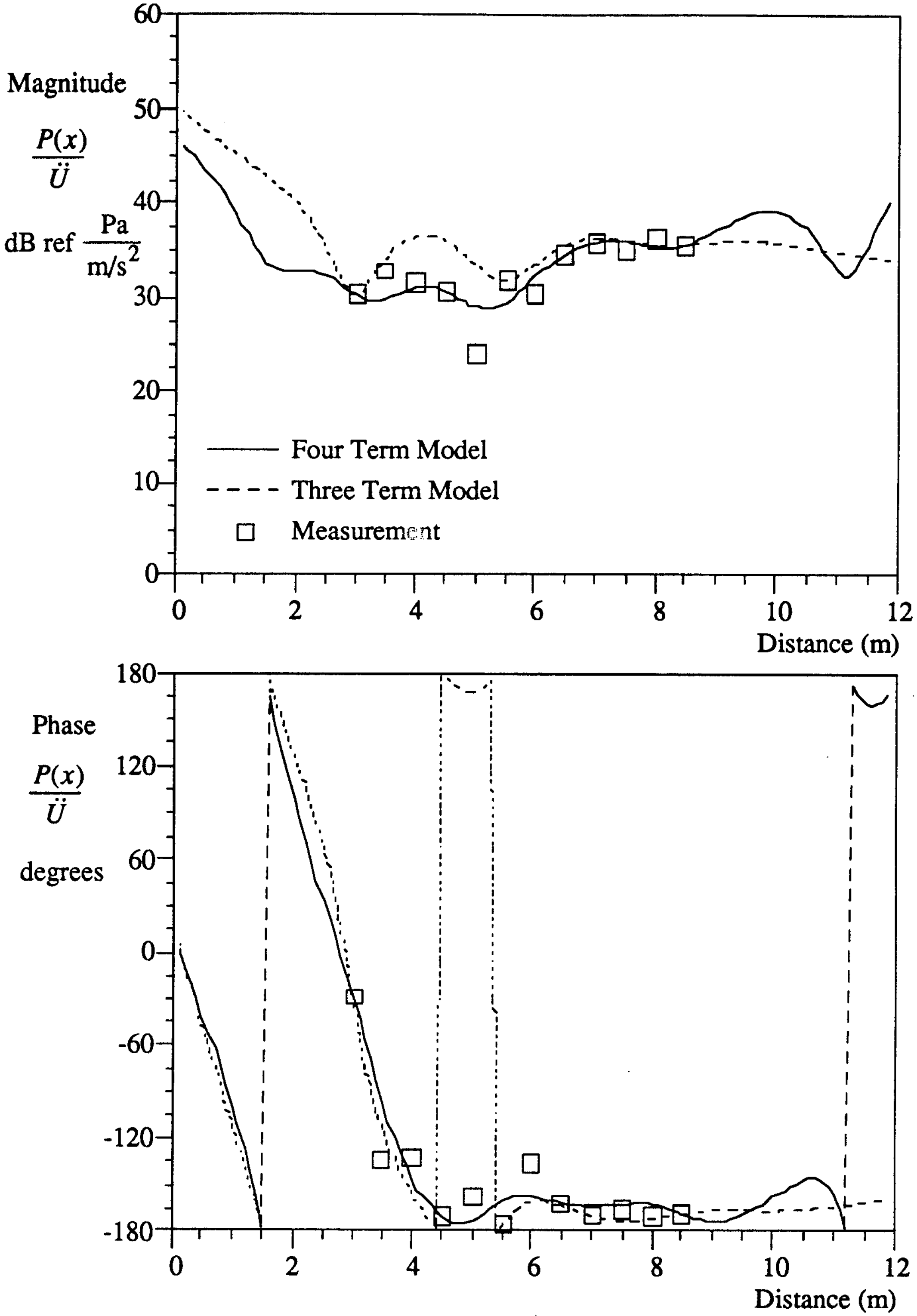

Figure B-9. Pressure Field Versus Distance at 22.4 Hz

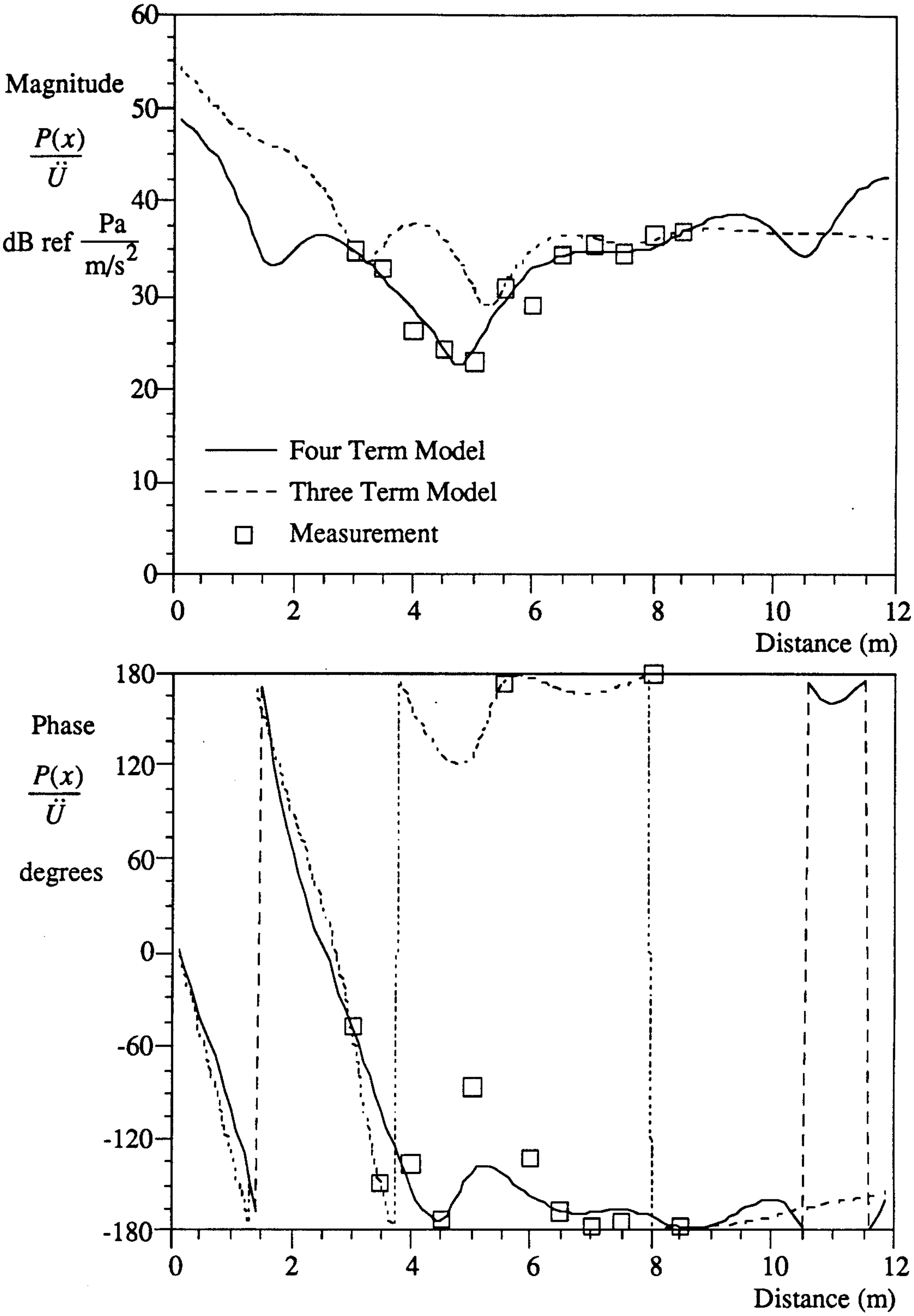

Figure B-10. Pressure Field Versus Distance at 24.8 Hz

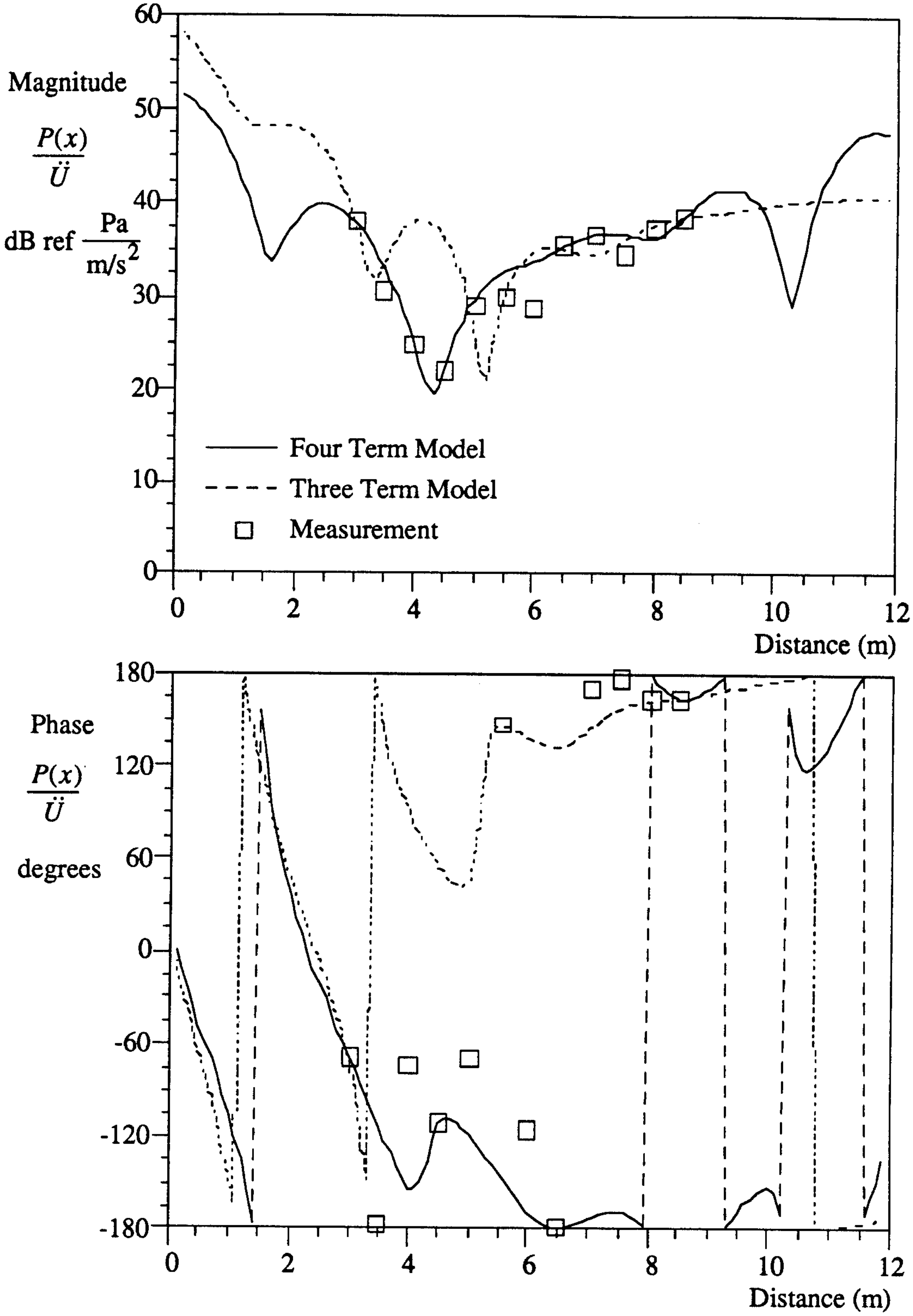

Figure B-11. Pressure Field Versus Distance at 27.3 Hz

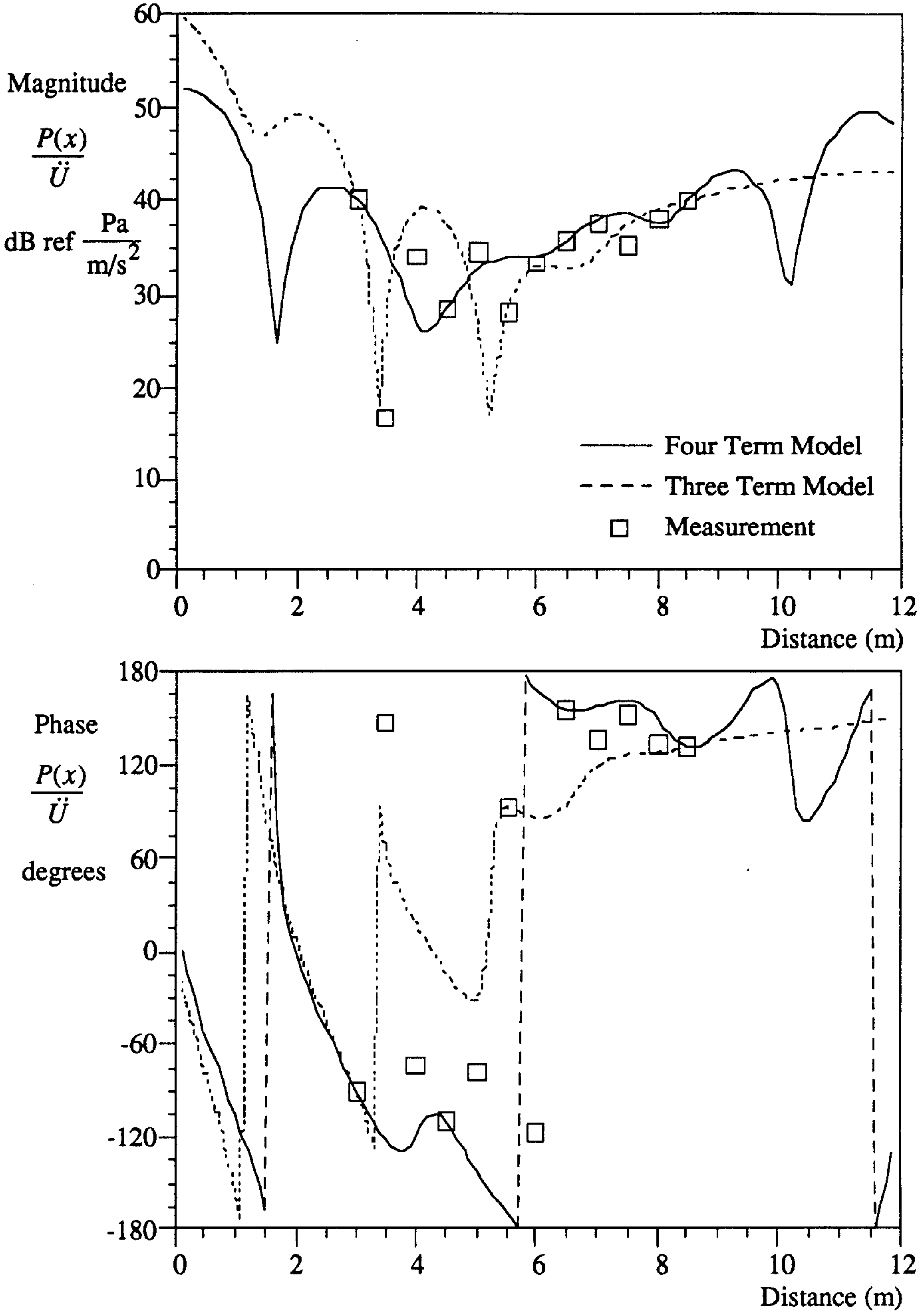

Figure B-12. Pressure Field Versus Distance at 29.7 Hz

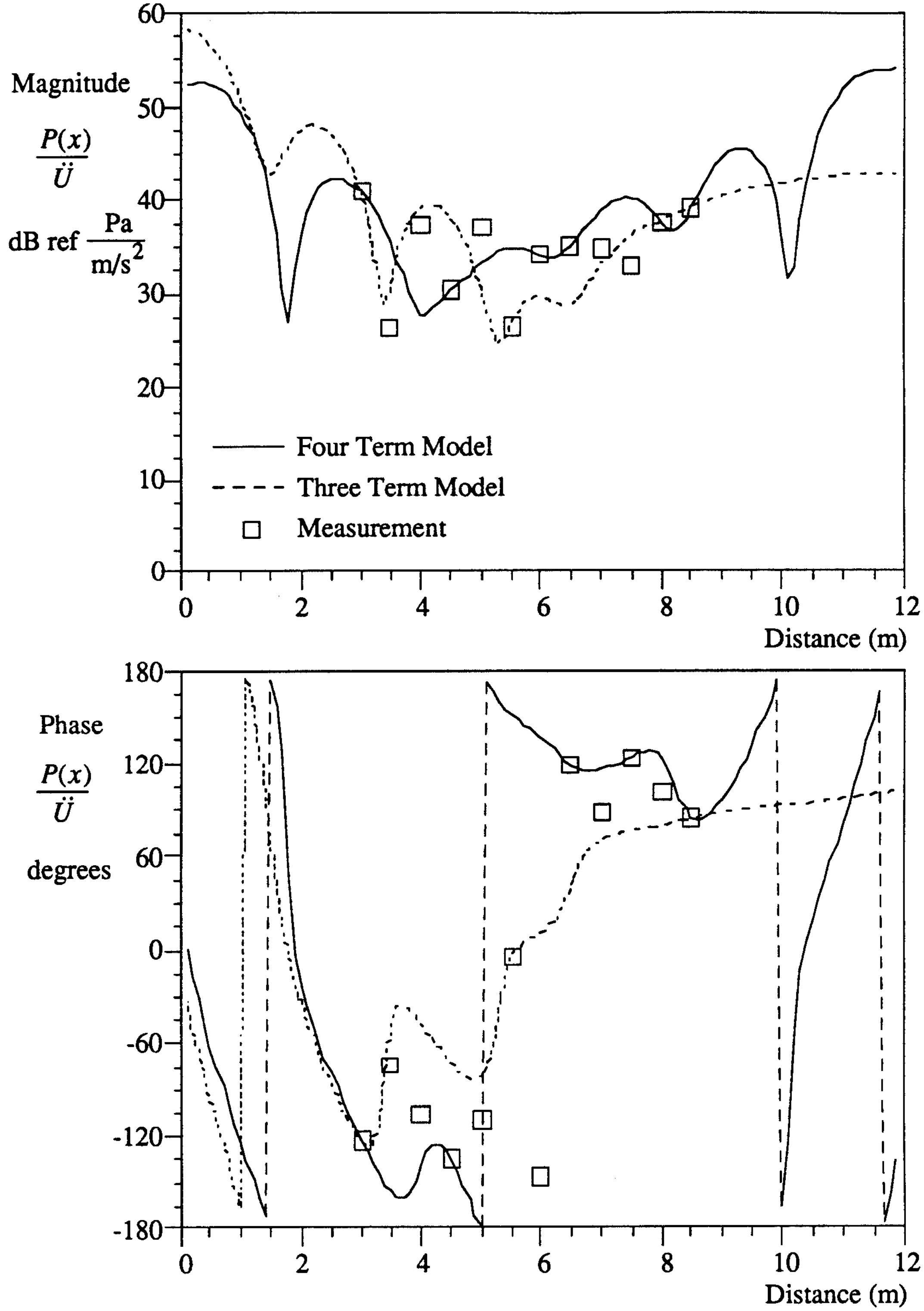

Figure B-13. Pressure Field Versus Distance at 32.1 Hz

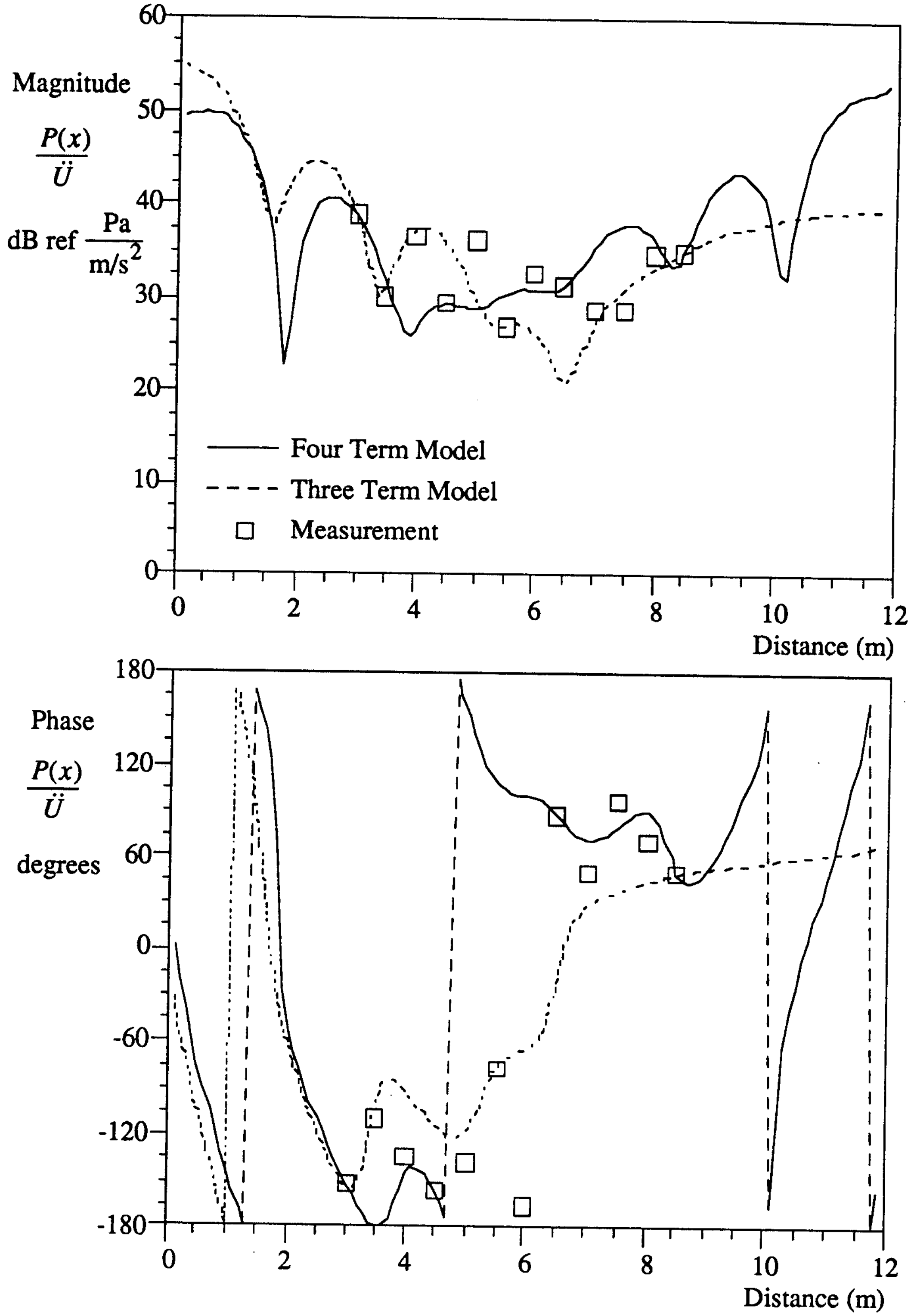

Figure B-14. Pressure Field Versus Distance at 34.5 Hz

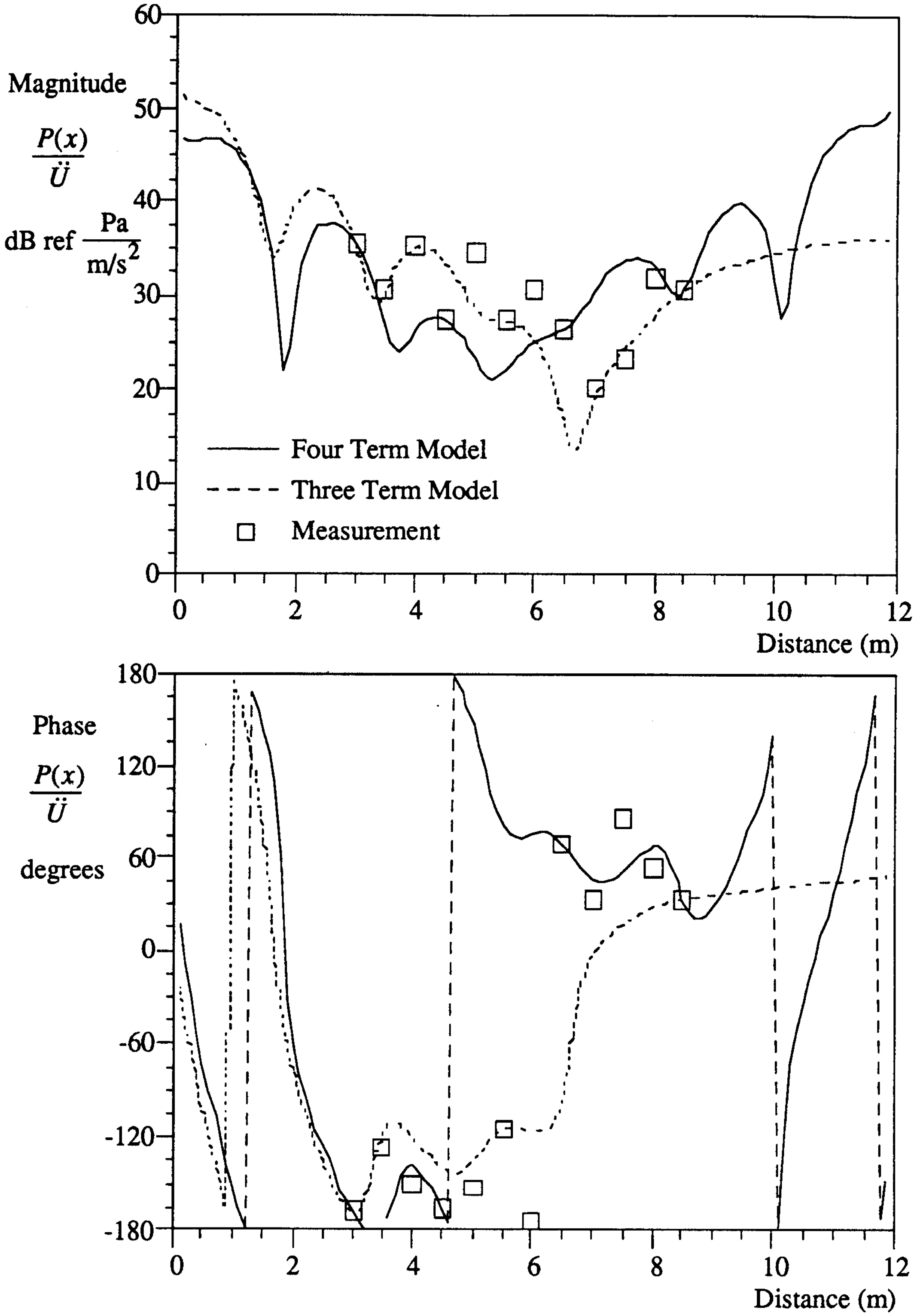

Figure B-15. Pressure Field Versus Distance at 37.0 Hz

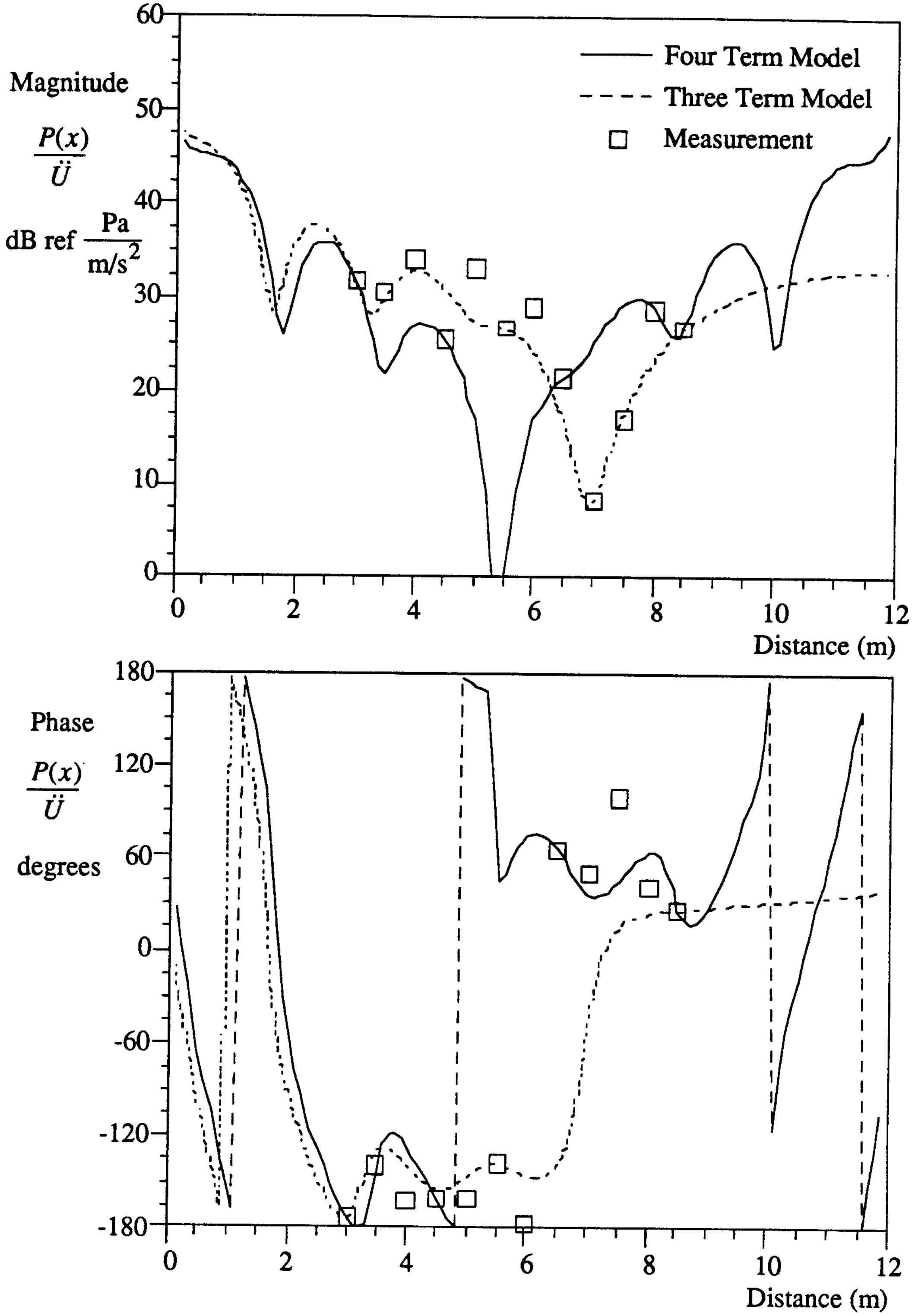

Figure B-16. Pressure Field Versus Distance at 39.4 Hz

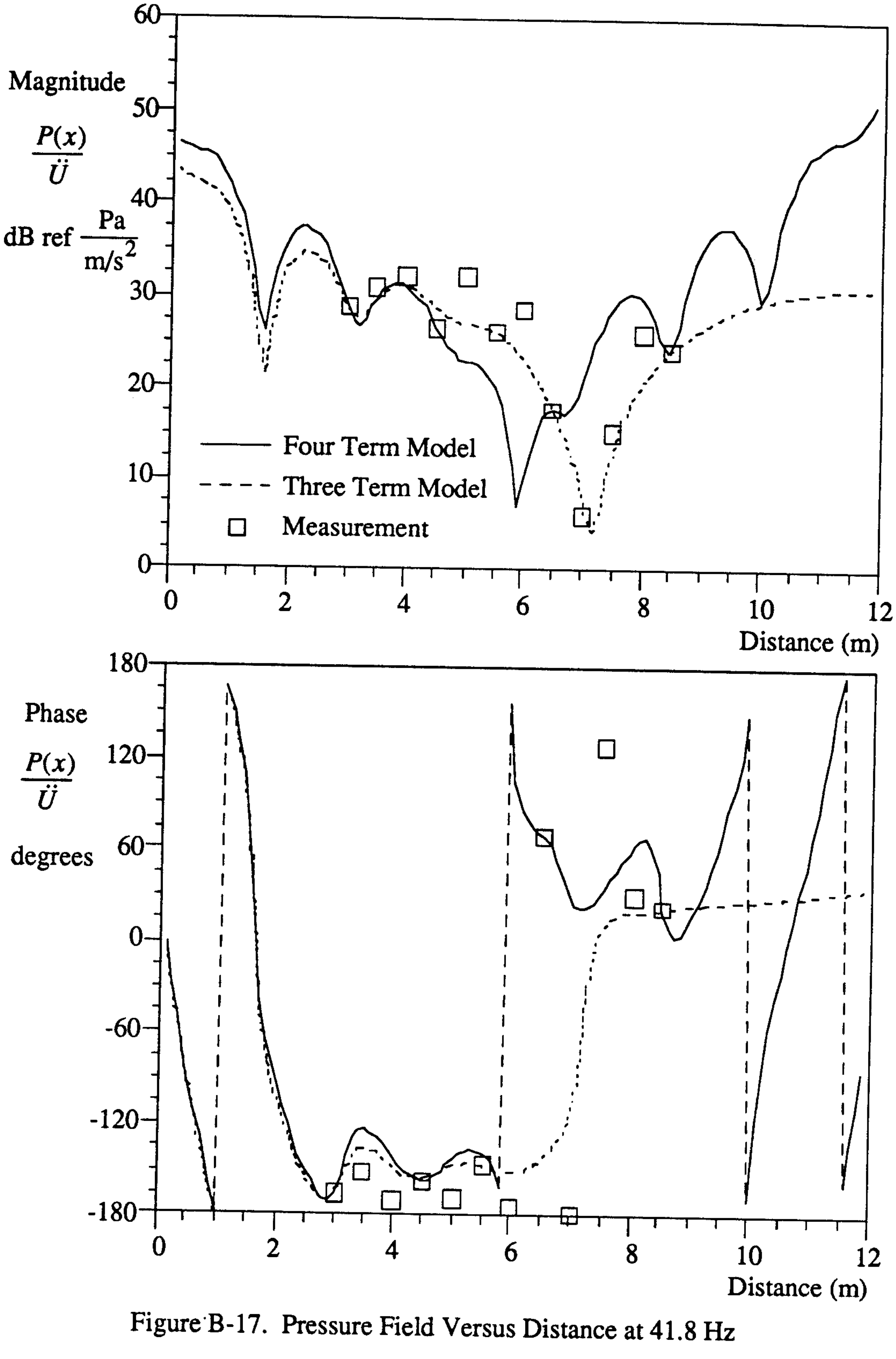

Figure B-17. Pressure Field Versus Distance at 41.8 Hz

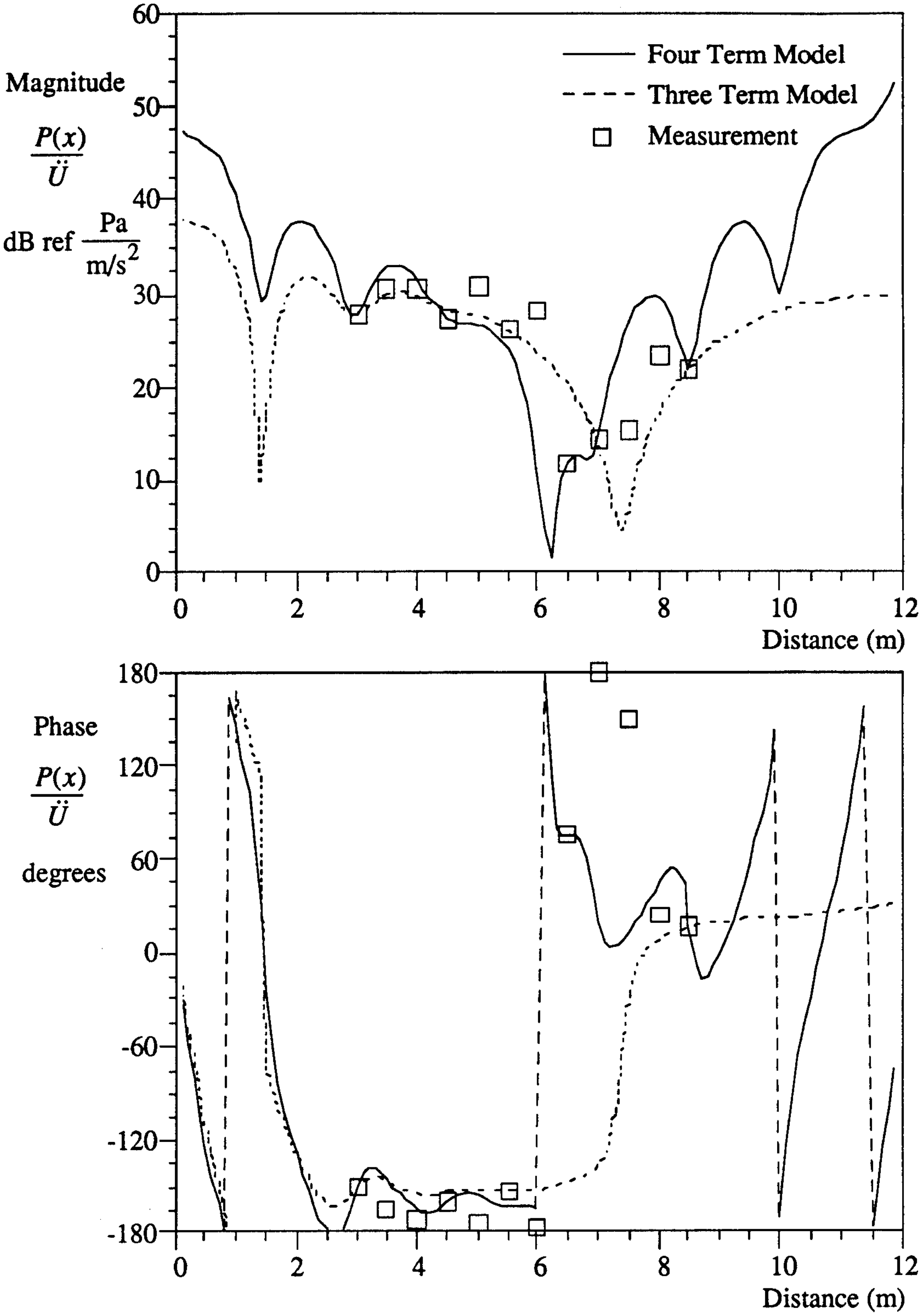

Figure B-18. Pressure Field Versus Distance at 44.2 Hz

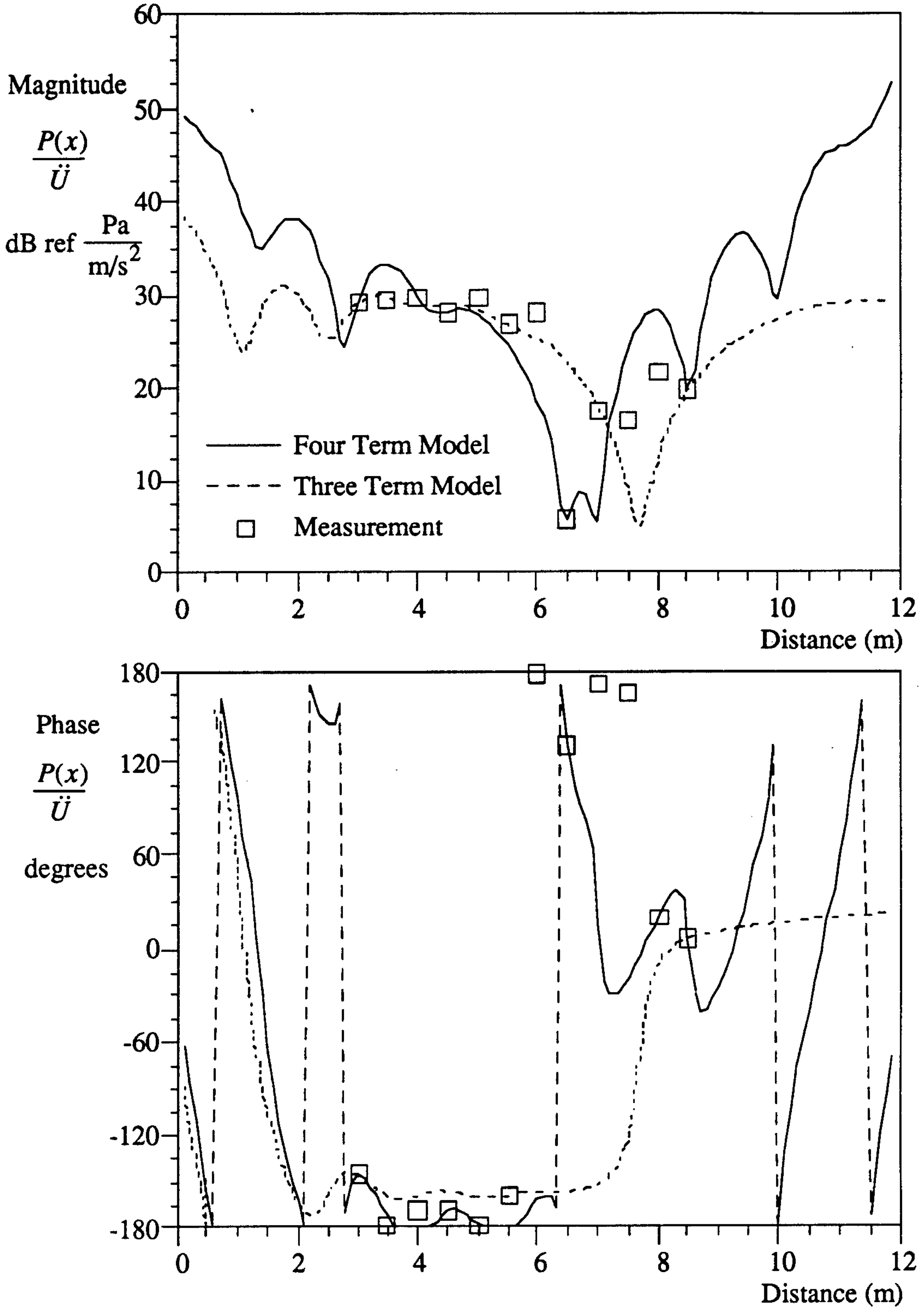

Figure B-19. Pressure Field Versus Distance at 46.7 Hz

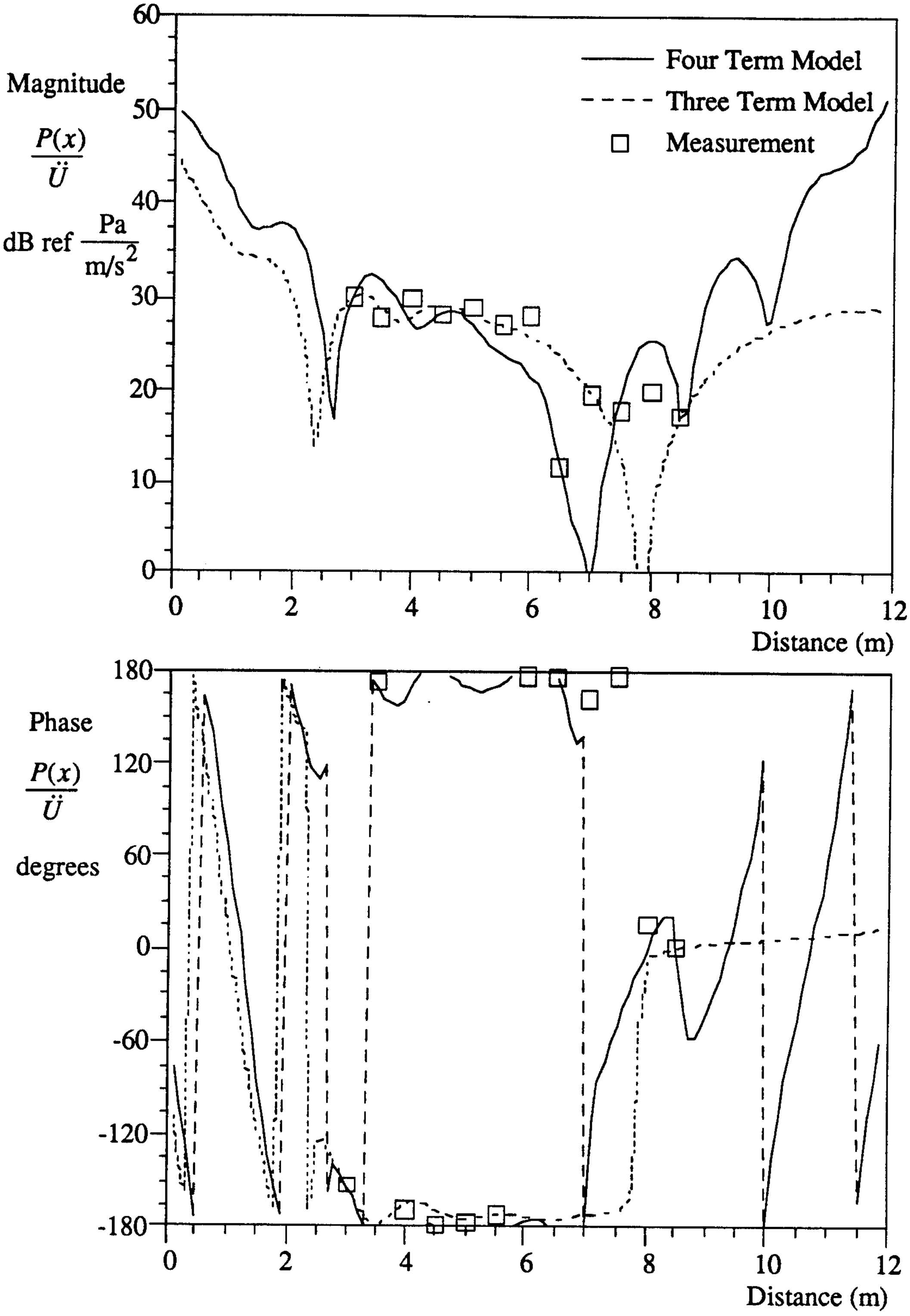

Figure B-20. Pressure Field Versus Distance at 49.1 Hz

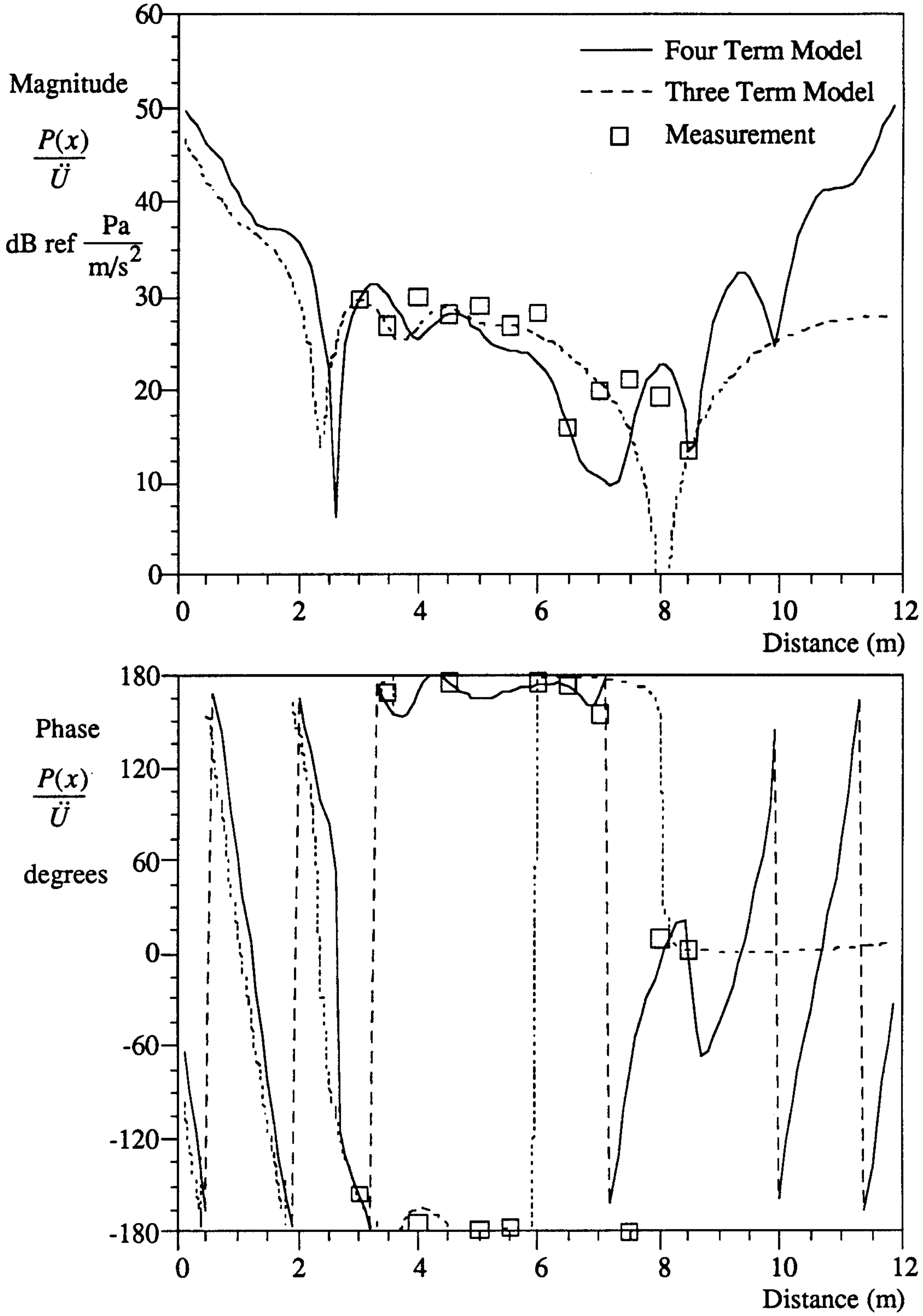

Figure B-21. Pressure Field Versus Distance at 51.5 Hz

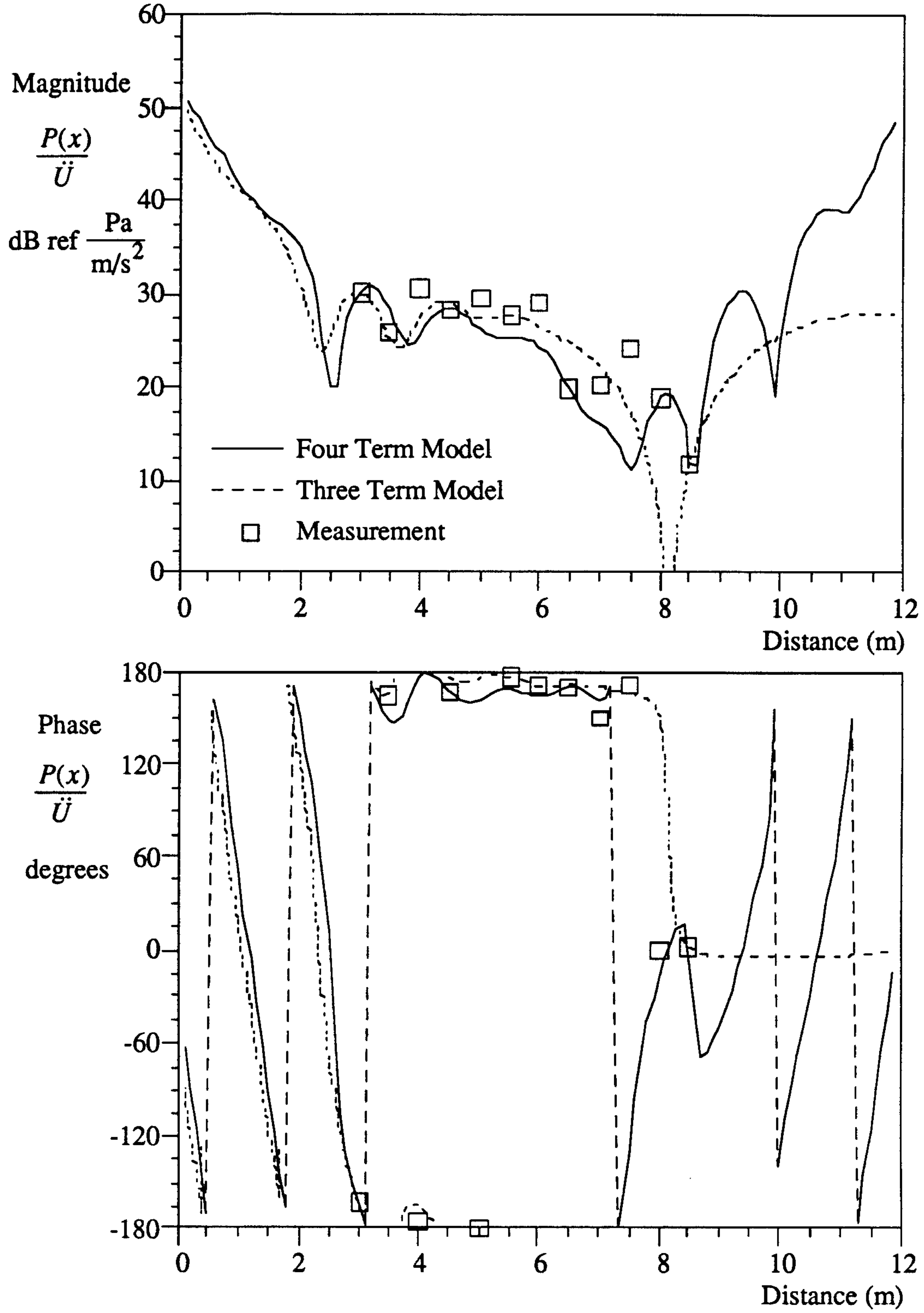

Figure B-22. Pressure Field Versus Distance at 53.9 Hz

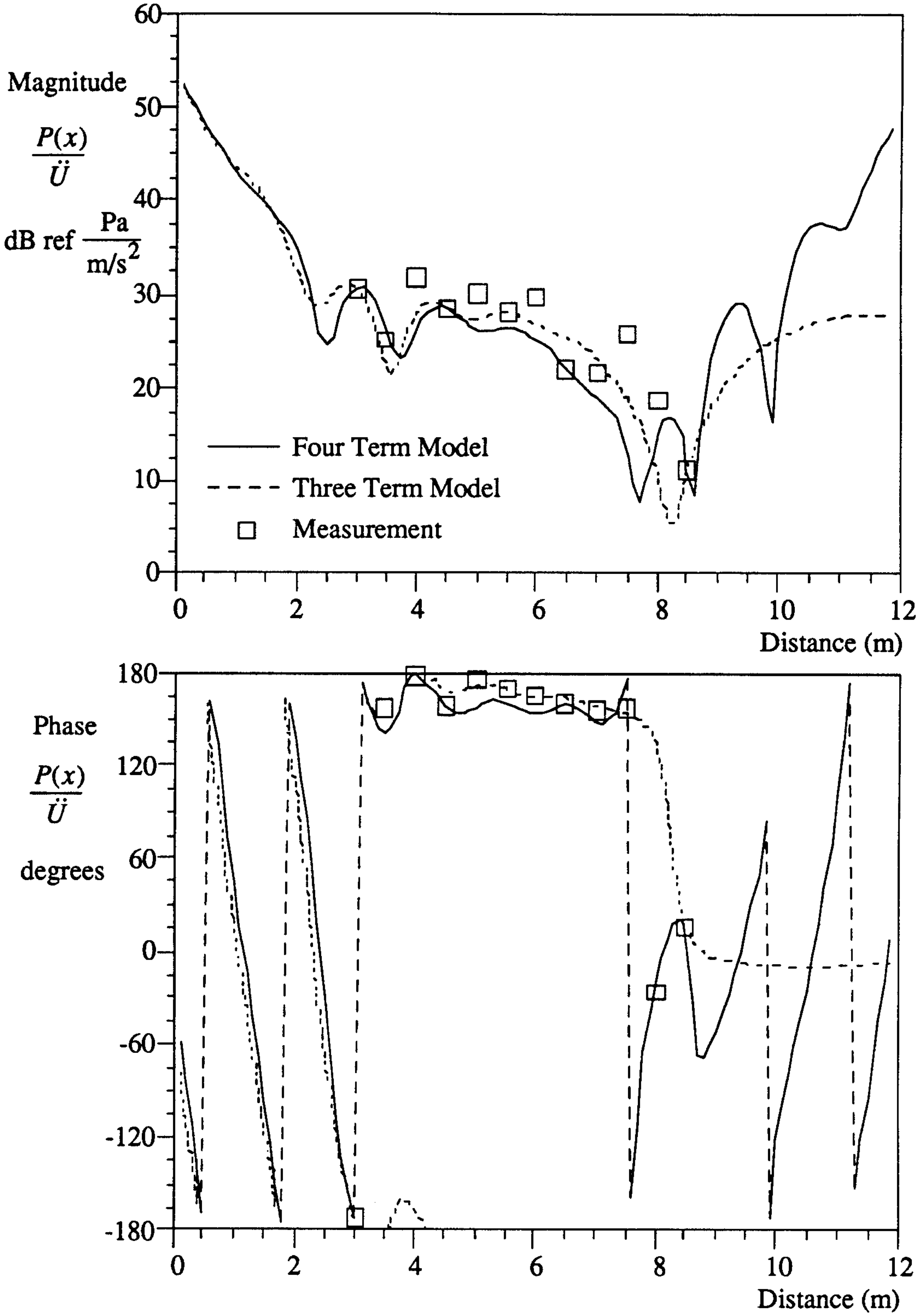

Figure B-23. Pressure Field Versus Distance at 56.4 Hz

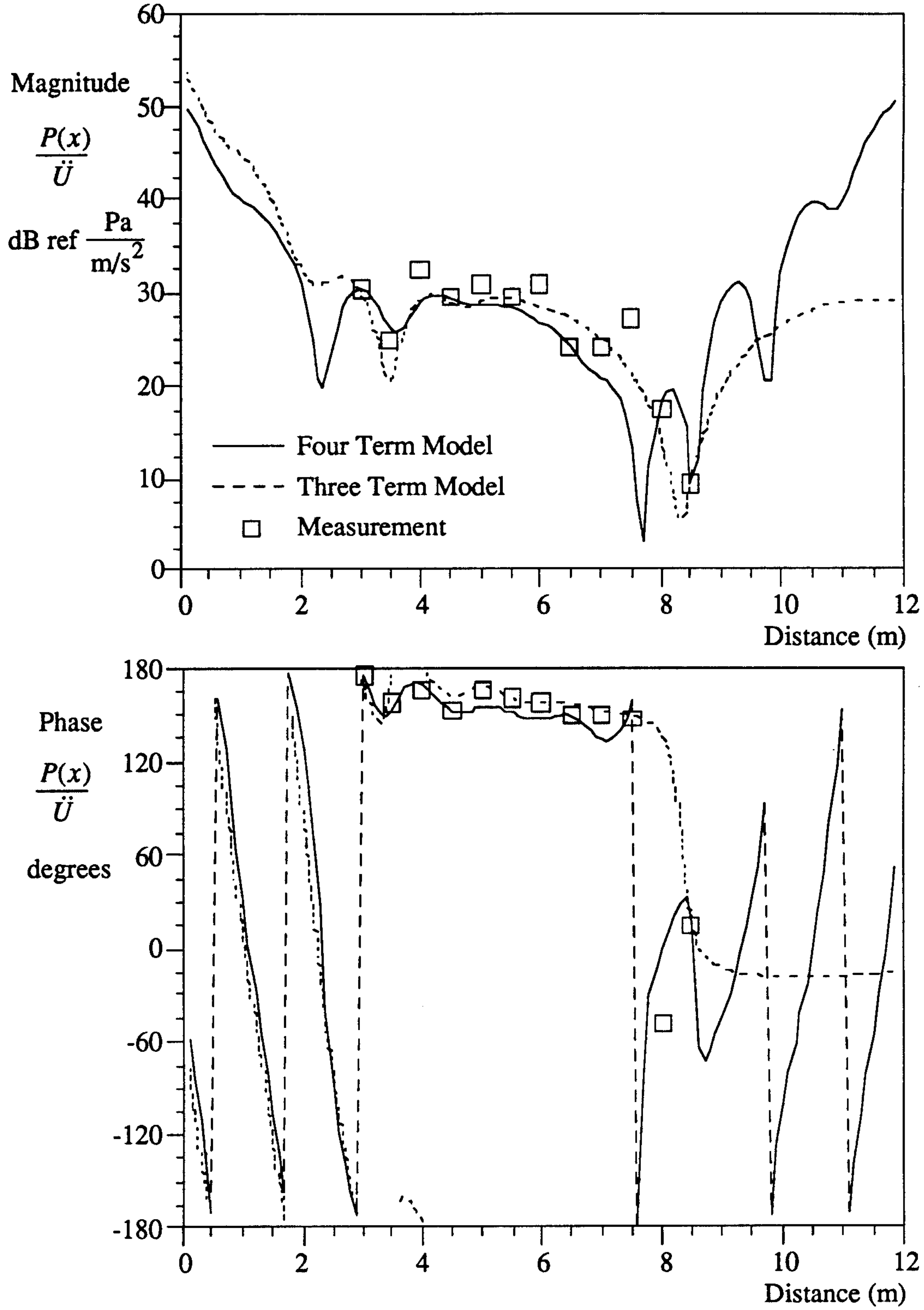

Figure B-24. Pressure Field Versus Distance at 58.8 Hz

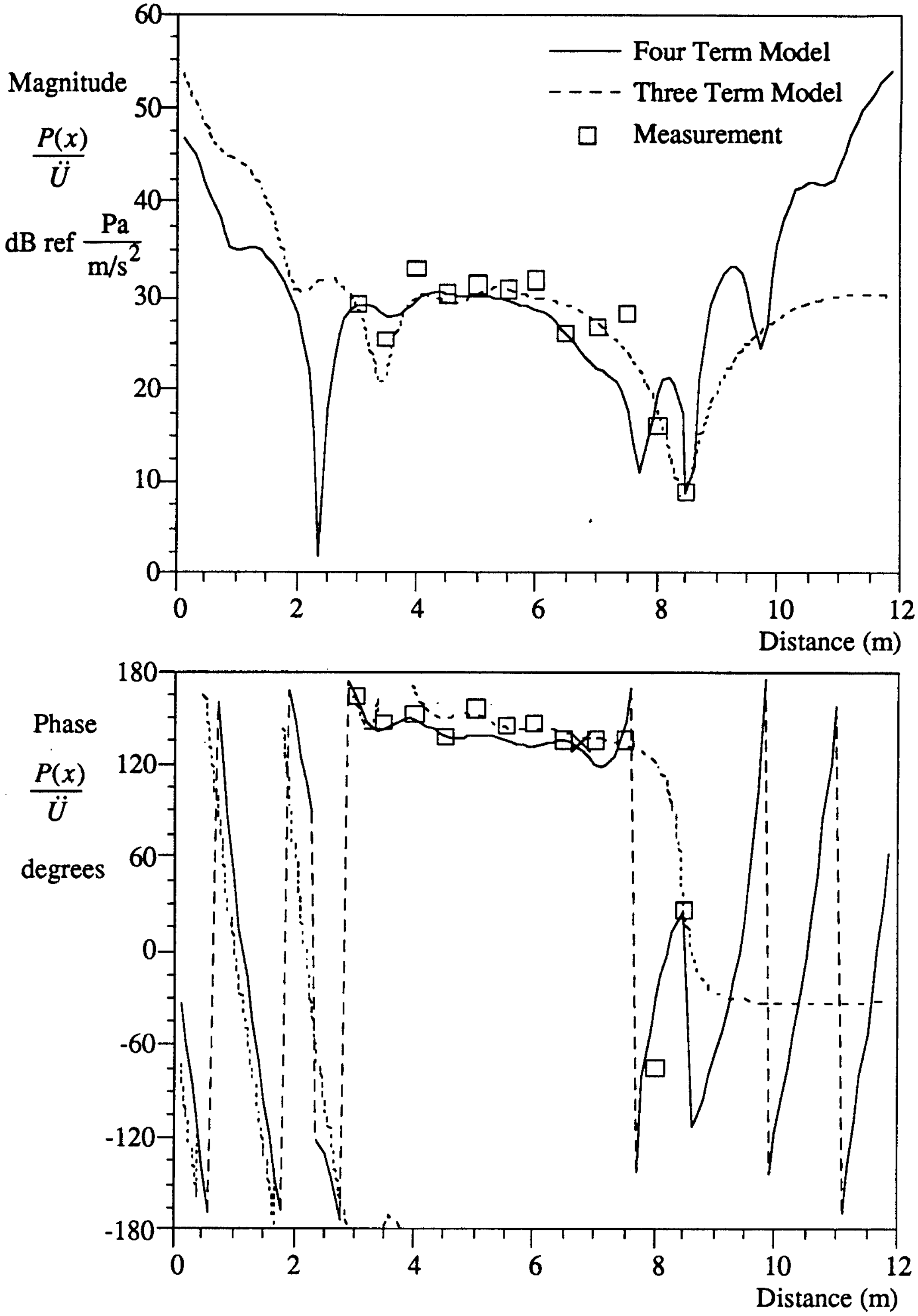

Figure B-25. Pressure Field Versus Distance at 61.2 Hz

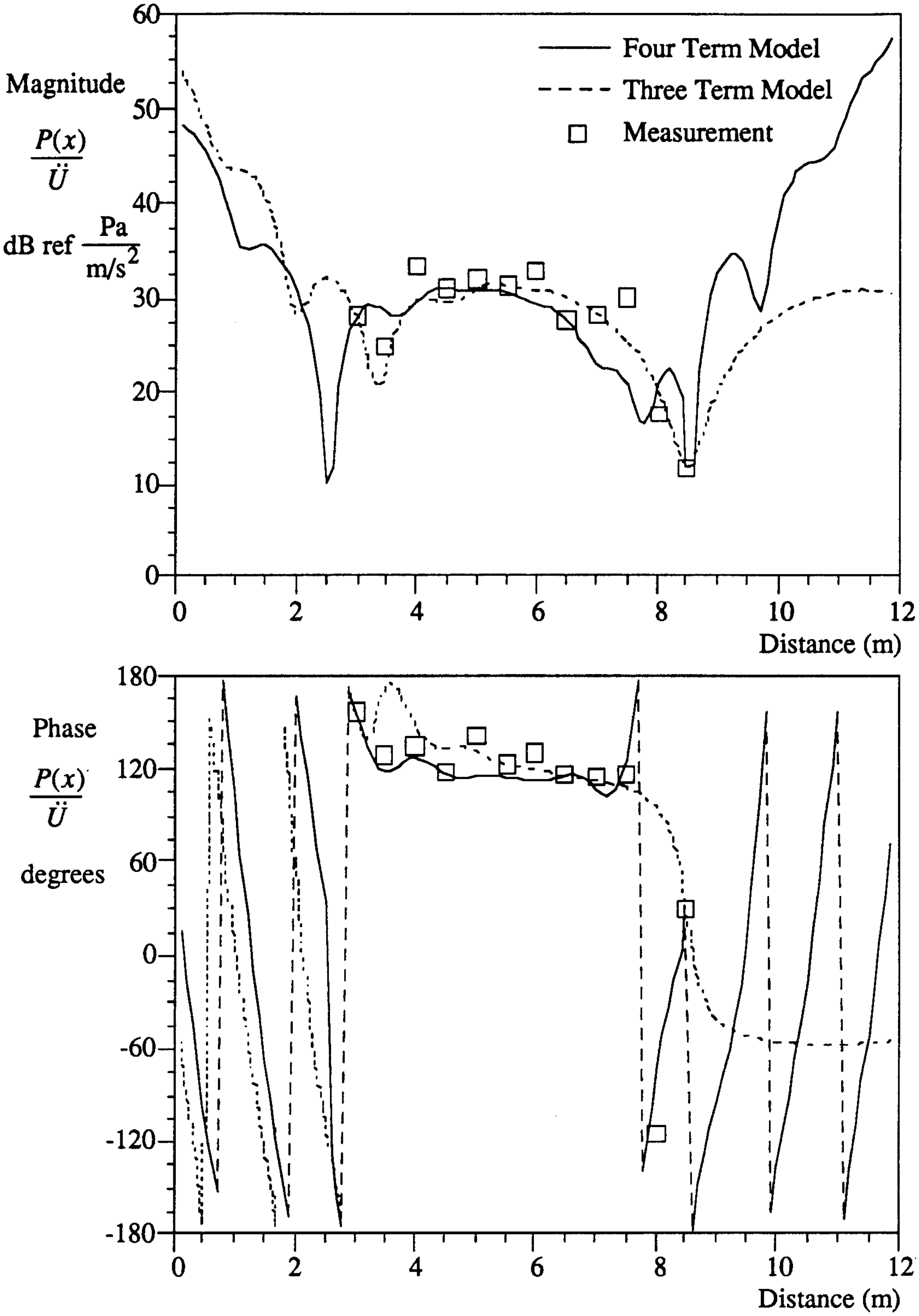

Figure B-26. Pressure Field Versus Distance at 63.6 Hz

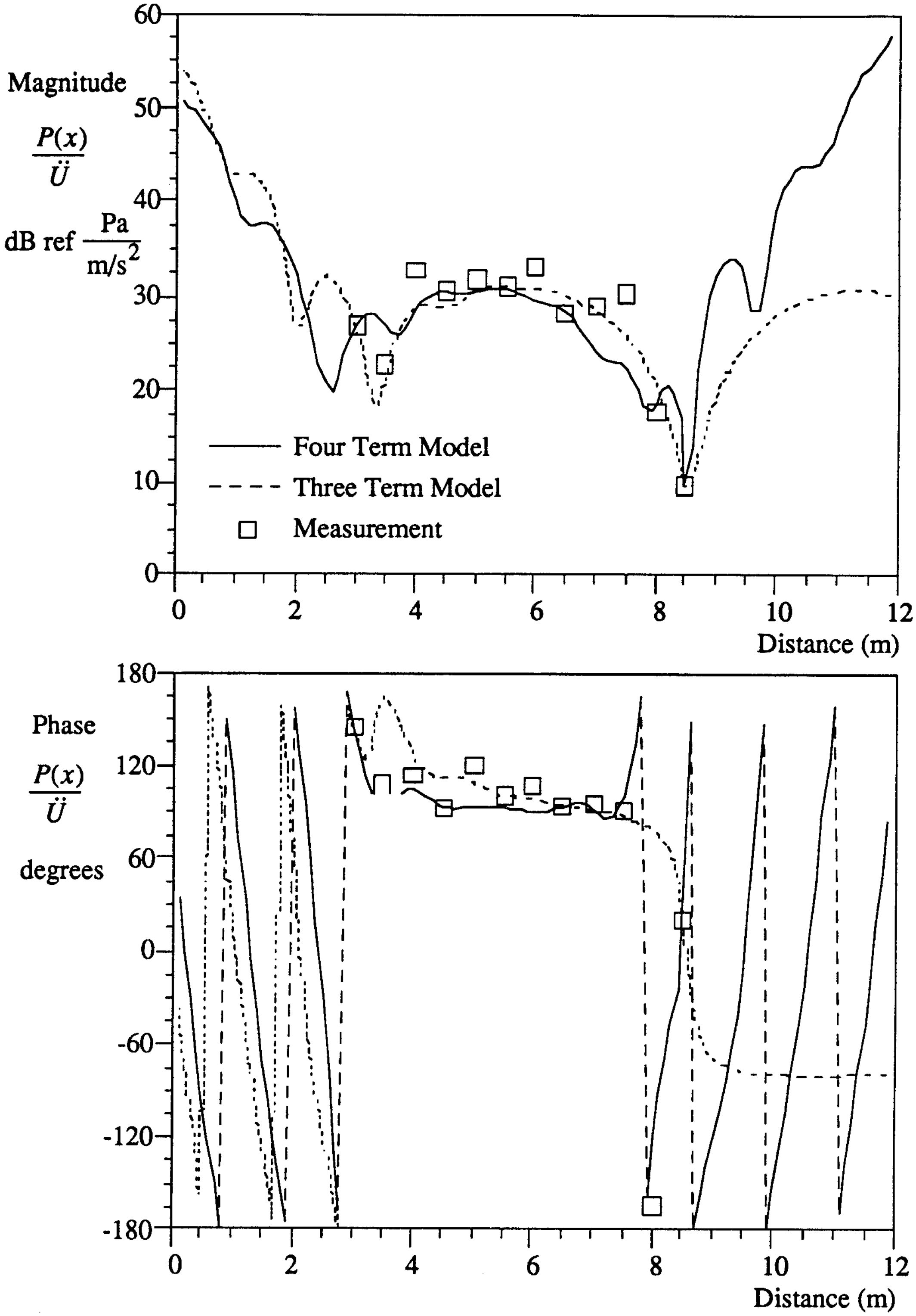

Figure B-27. Pressure Field Versus Distance at 66.1 Hz

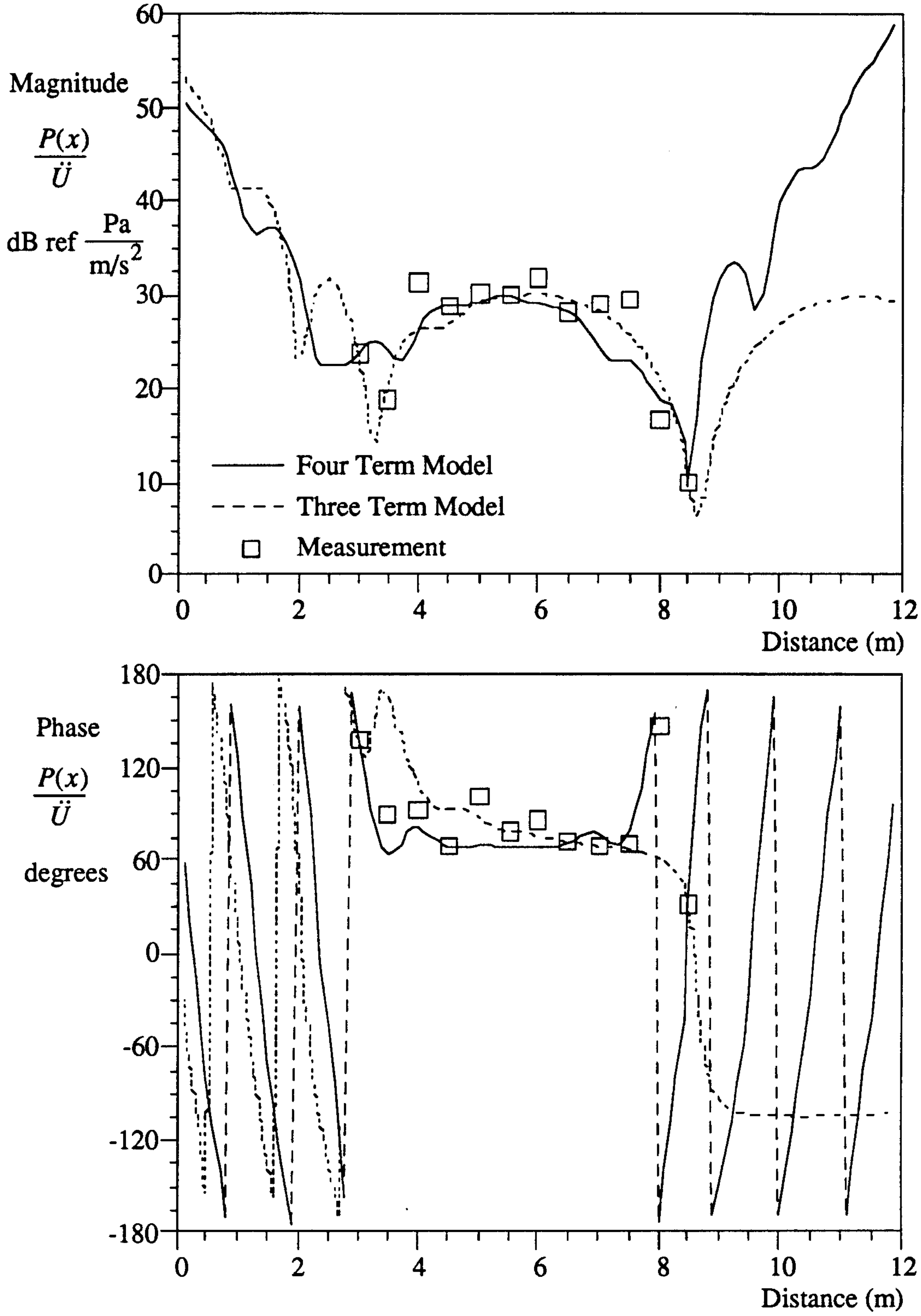

Figure B-28. Pressure Field Versus Distance at 68.5 Hz

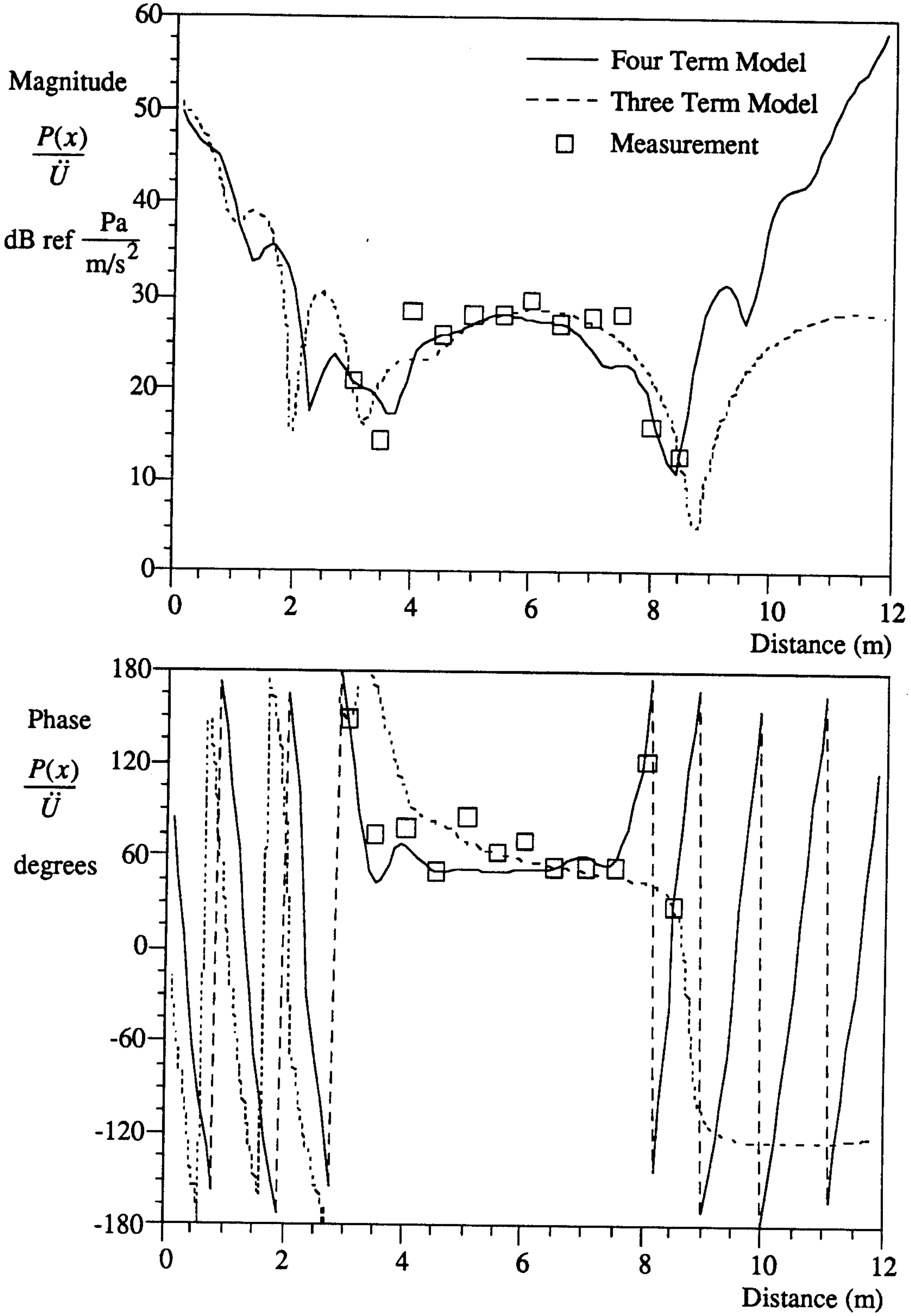

Figure B-29. Pressure Field Versus Distance at 70.9 Hz

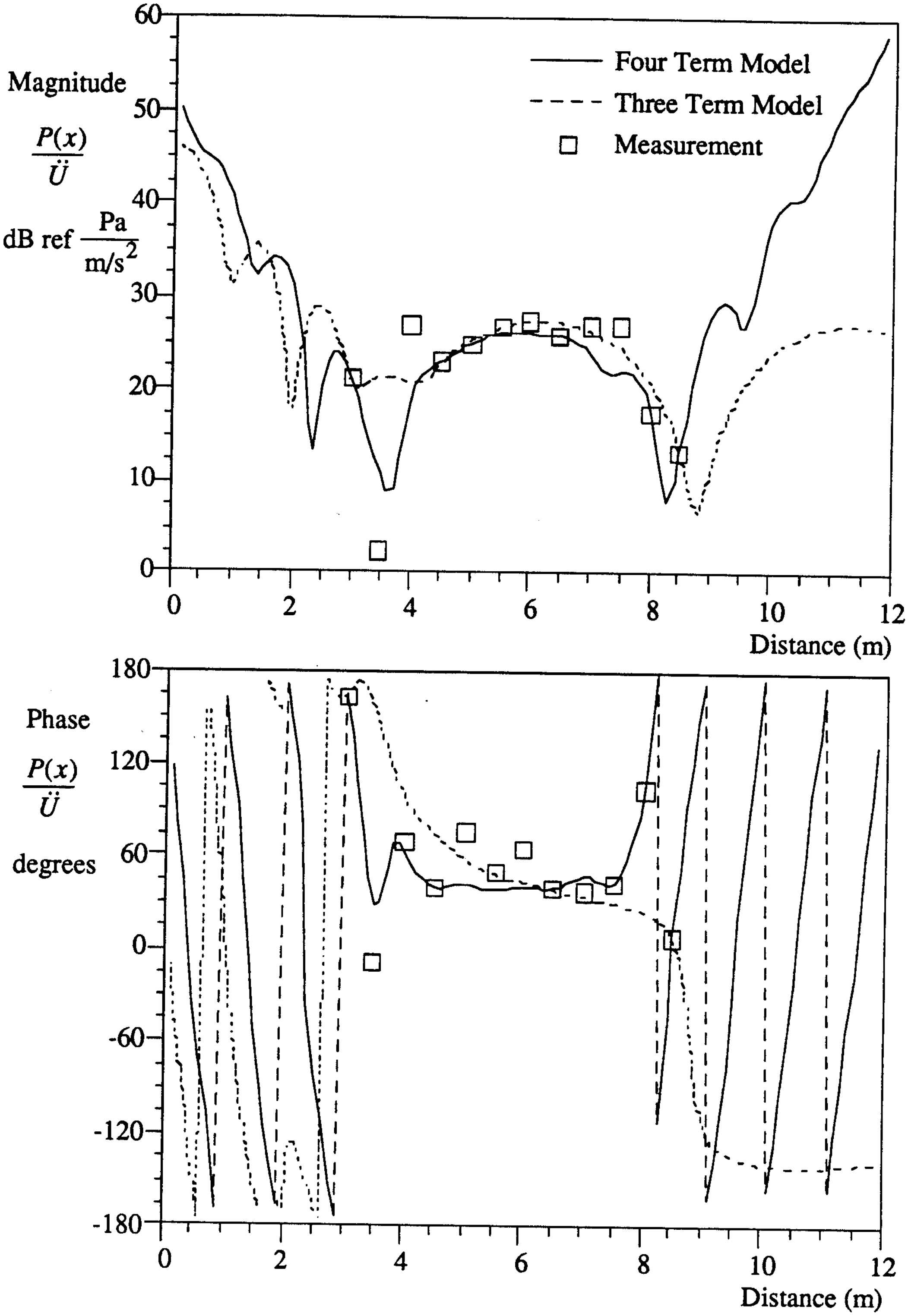

Figure B-30. Pressure Field Versus Distance at 73.3 Hz

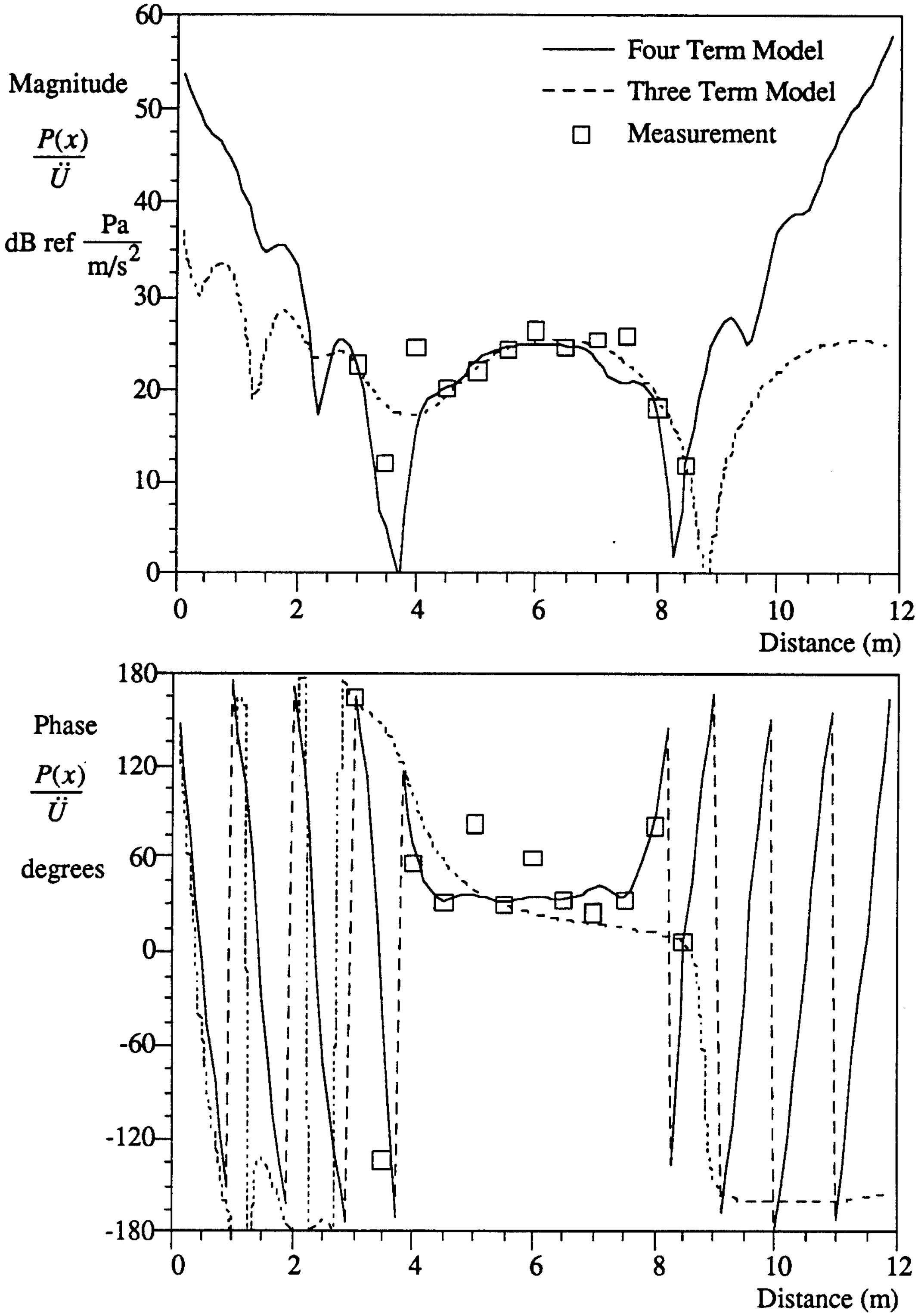

Figure B-31. Pressure Field Versus Distance at 75.8 Hz

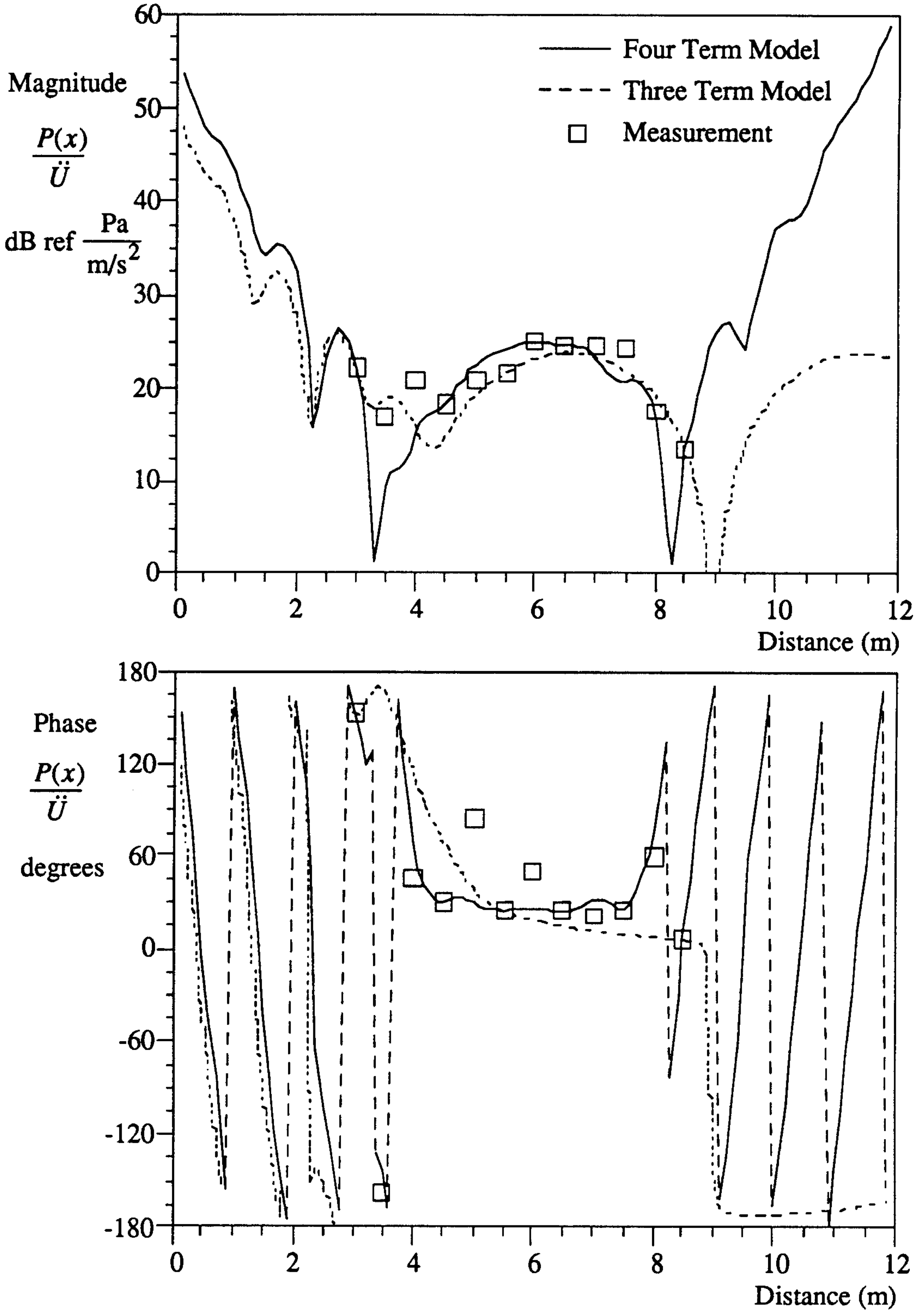

Figure B-32. Pressure Field Versus Distance at 78.2 Hz

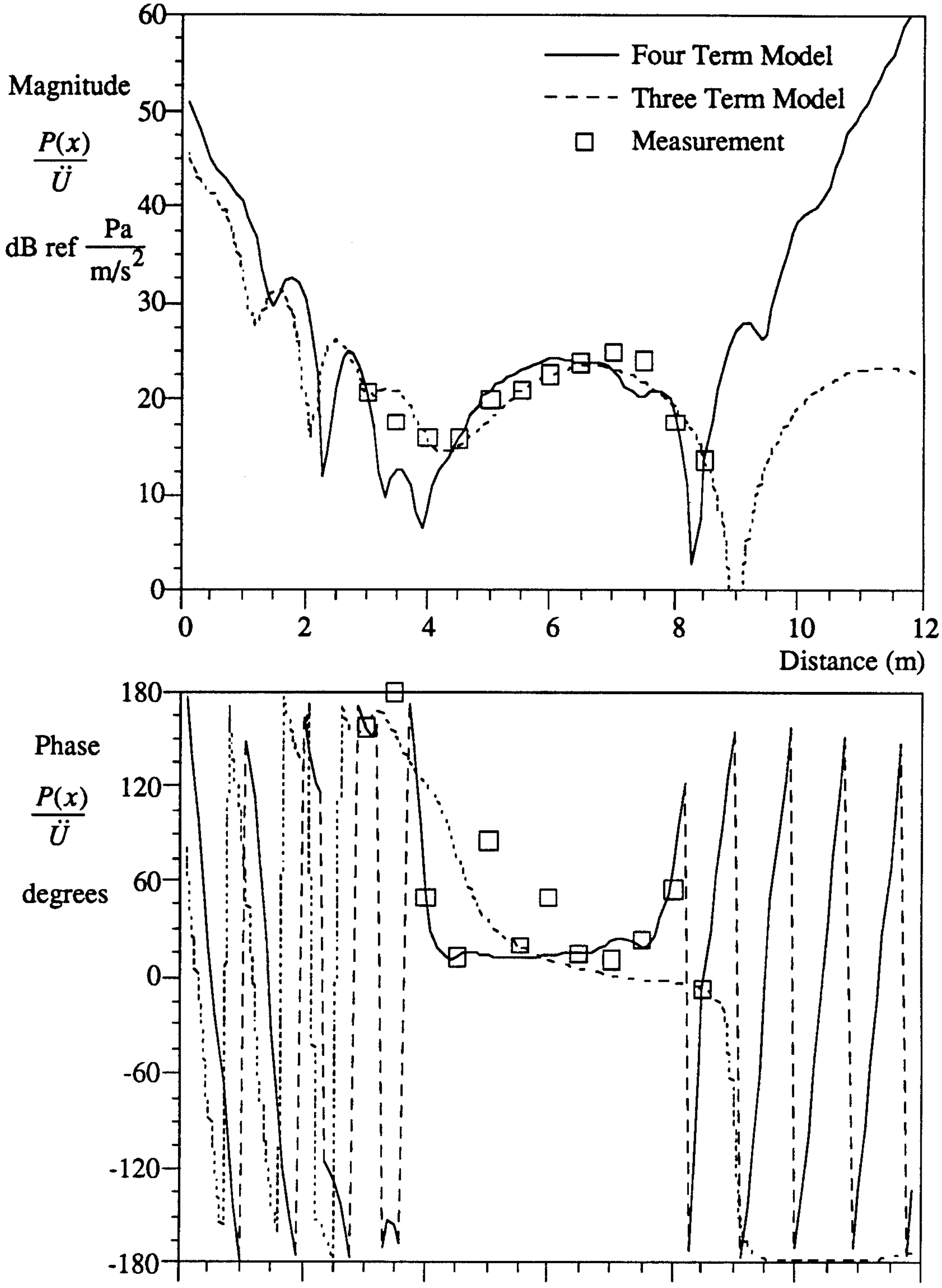

Figure B-33. Pressure Field Versus Distance at 80.6 Hz

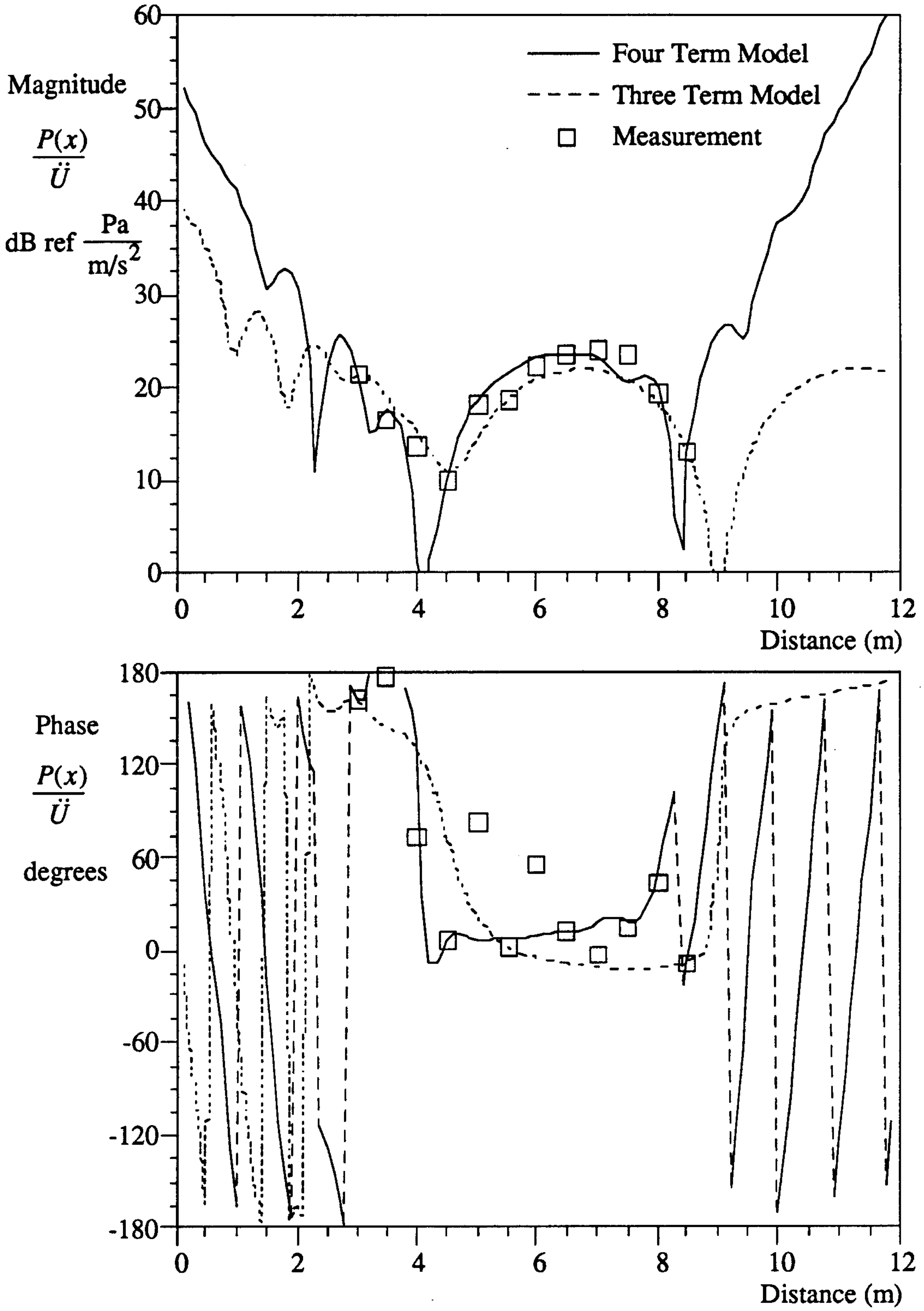

Figure B-34. Pressure Field Versus Distance at 83.0 Hz

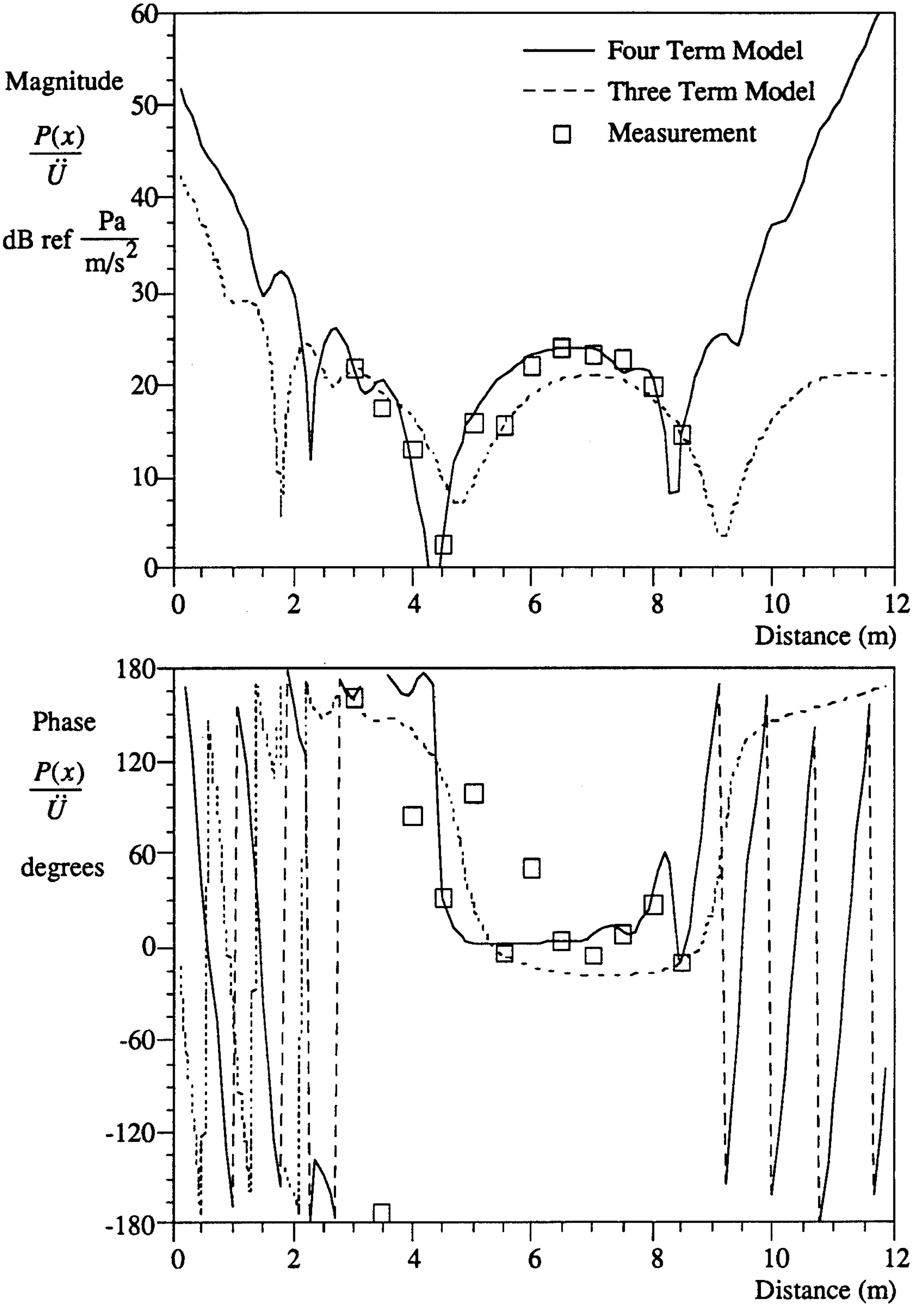

Figure B-35. Pressure Field Versus Distance at 85.5 Hz

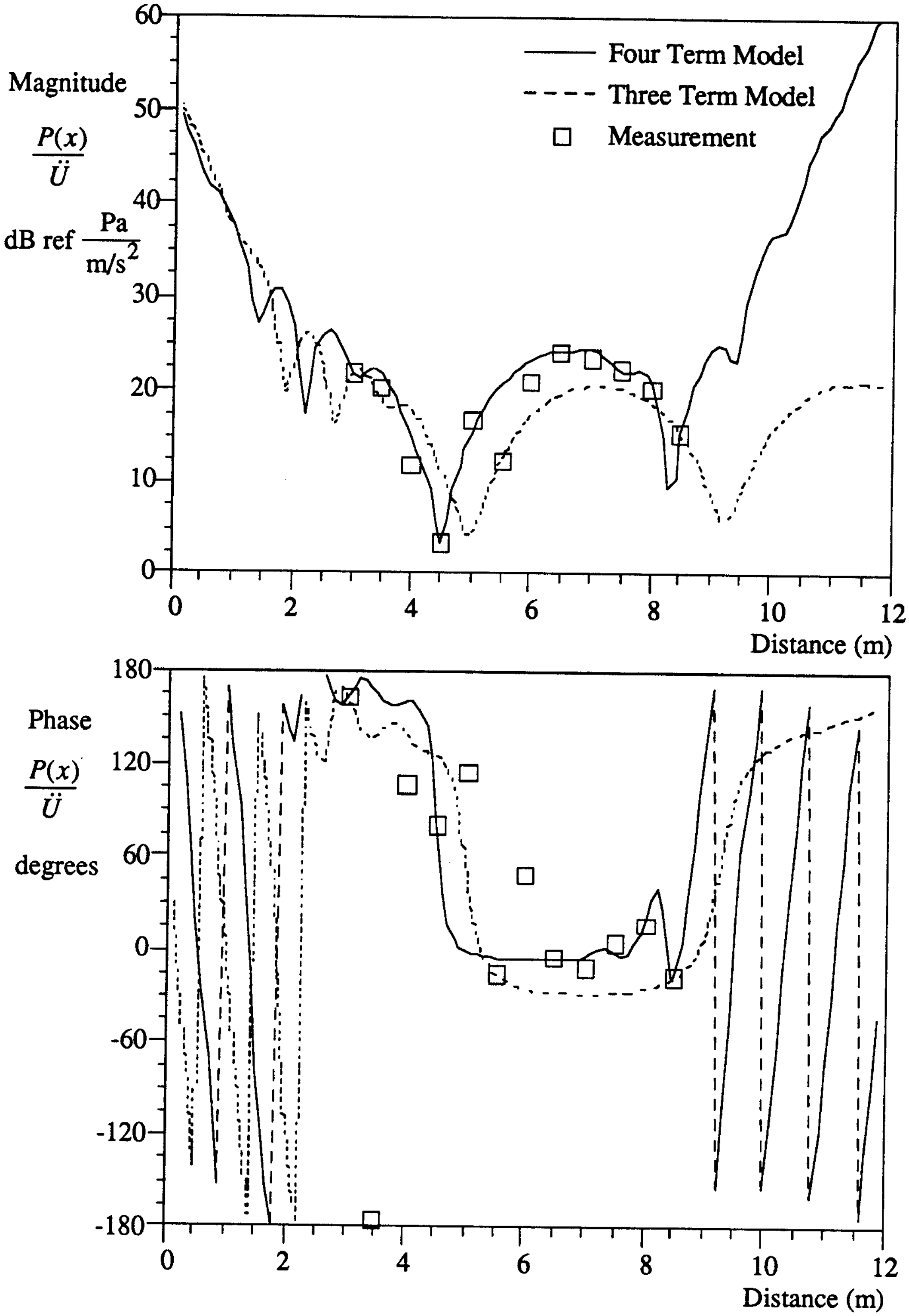

Figure B-36. Pressure Field Versus Distance at 87.9 Hz

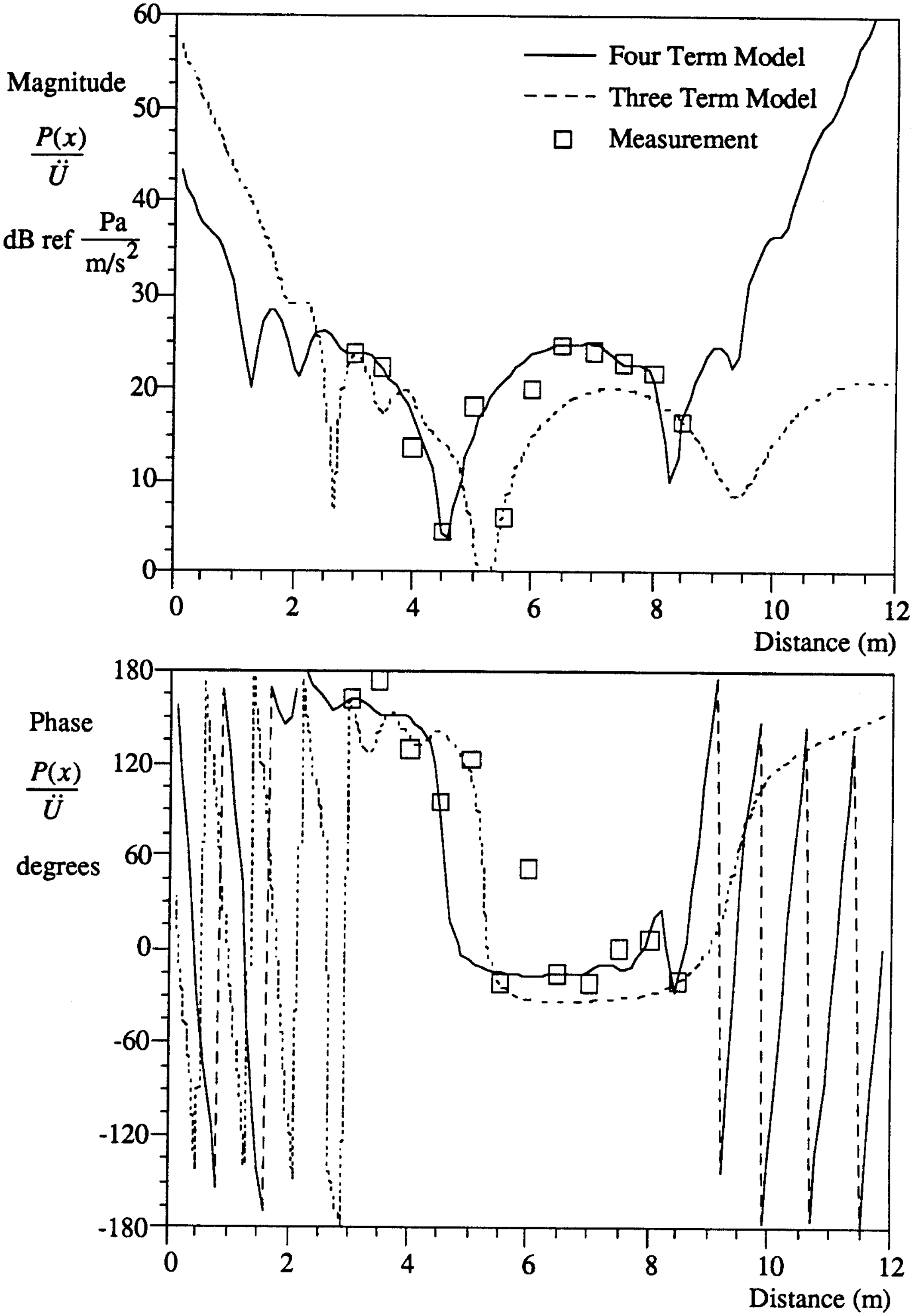

Figure B-37. Pressure Field Versus Distance at 90.3 Hz

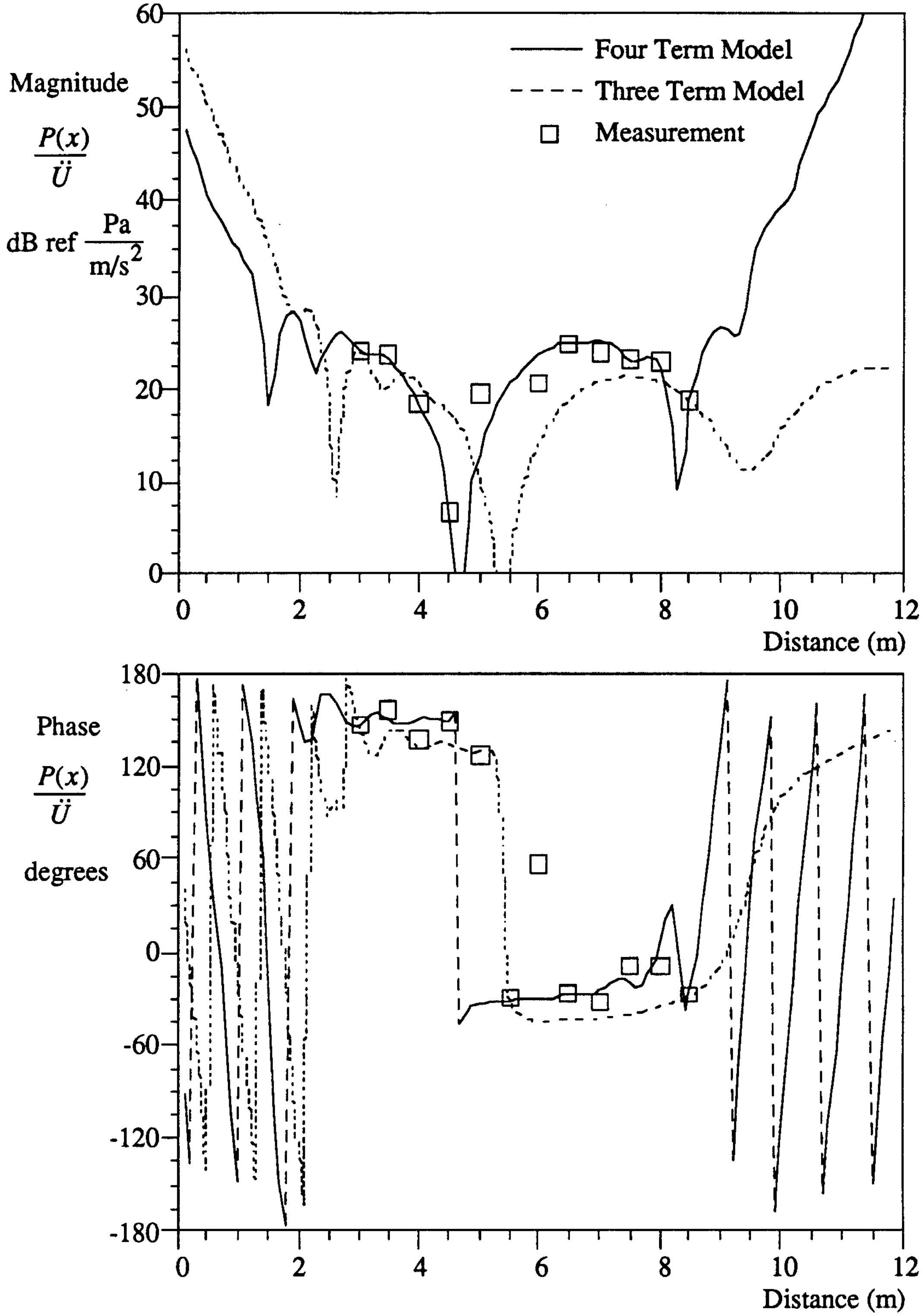

Figure B-38. Pressure Field Versus Distance at 92.7 Hz

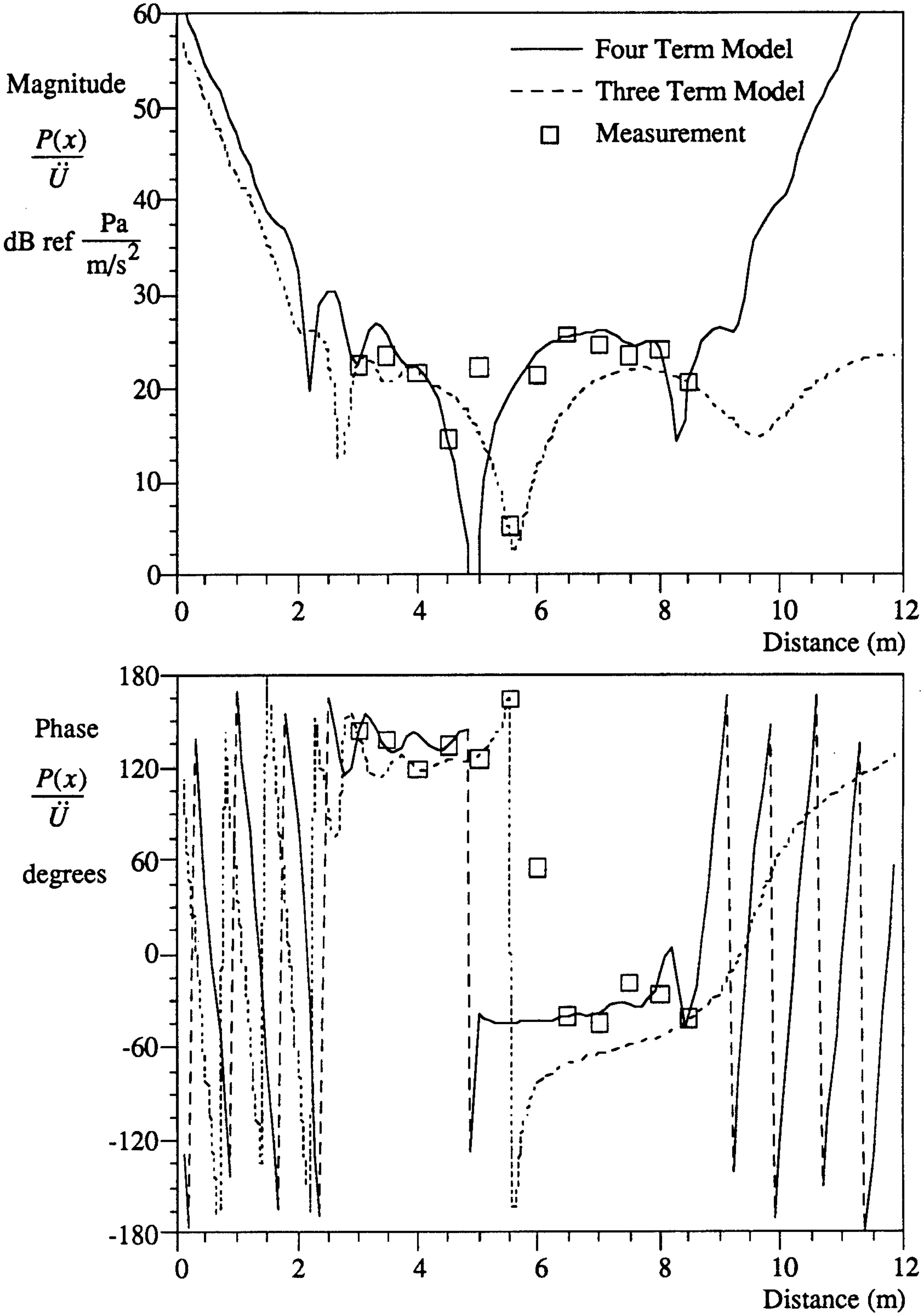

Figure B-39. Pressure Field Versus Distance at 95.2 Hz

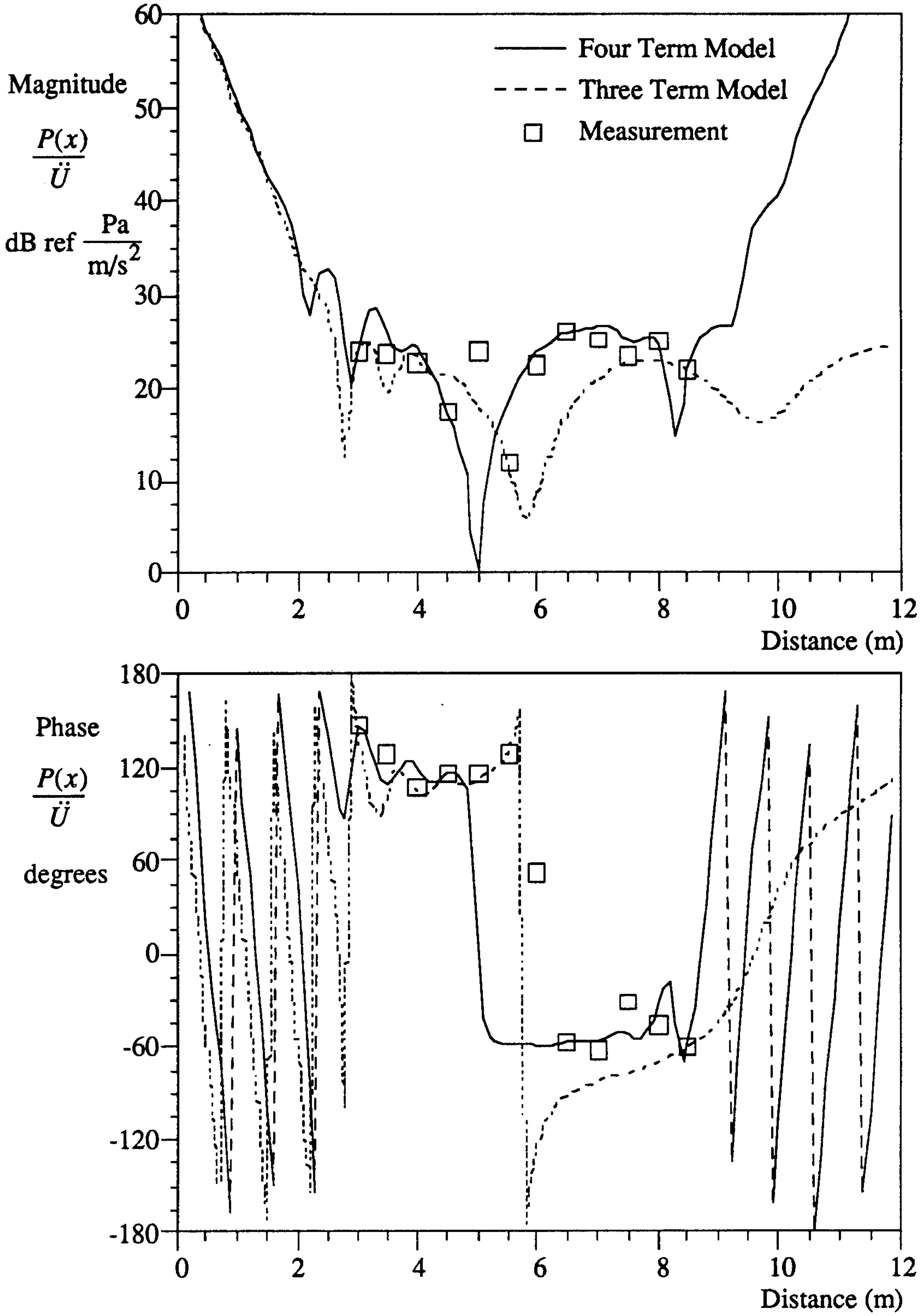

Figure B-40. Pressure Field Versus Distance at 97.6 Hz

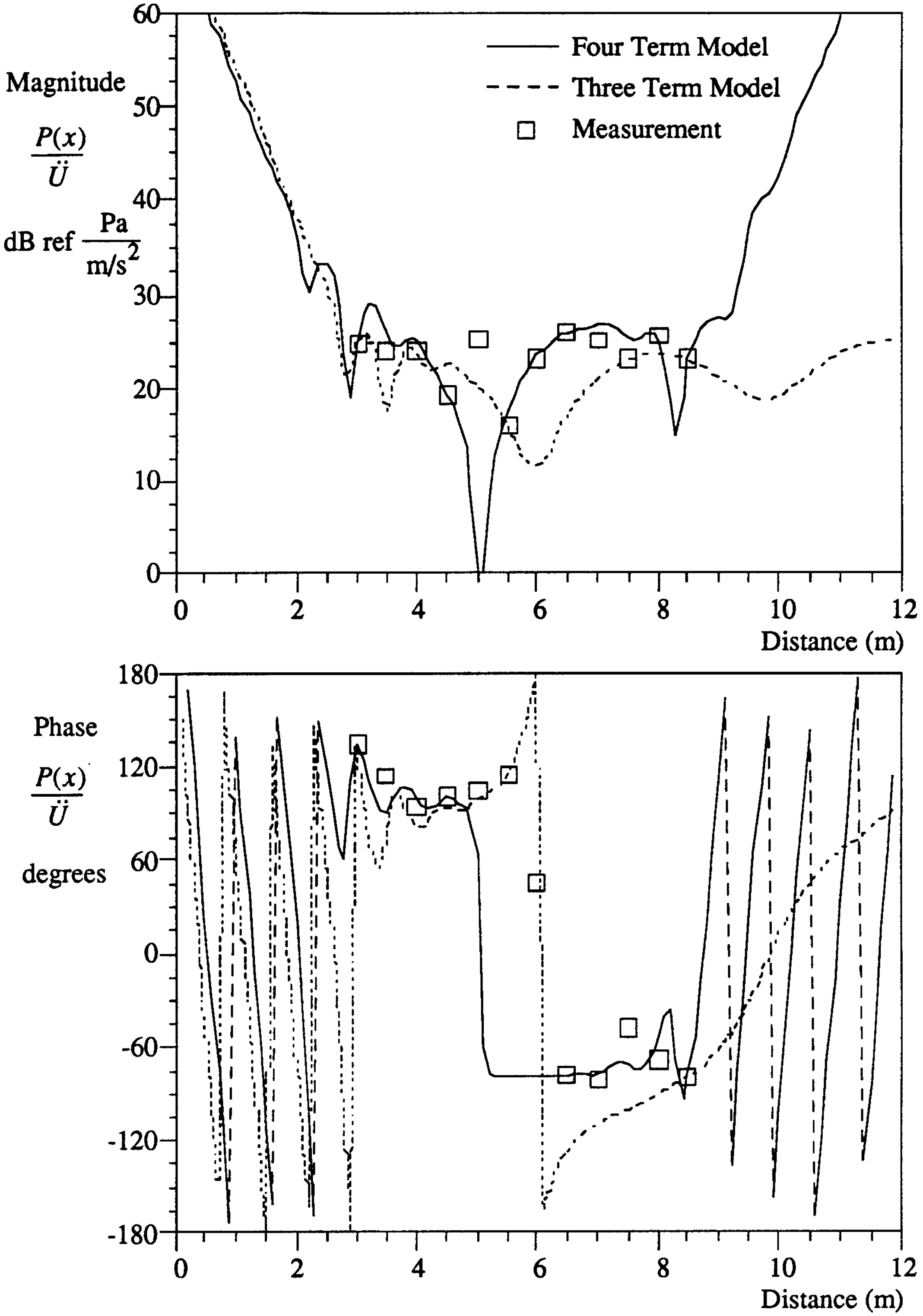

Figure B-41. Pressure Field Versus Distance at 100.0 Hz

INITIAL DISTRIBUTION LIST

Addressee	No. of Copies
Defense Technical Information Center	12
Naval Sea Systems Command (CAPT J. Jarbak, PMS-425; M. Basilica, PMS 4251; D. Lechner, PMS-42511)	3
Office of Naval Research (ONR 321: T. G. Goldsberry, K. Dial, R. Varley)	3
Program Executive Office-USW-ASTO (CDR J. Polcari, W. Chen, A. Hommel, J. Jones, LCDR M. Traweek, R. Melusky)	6
Space and Naval Warfare Systems Command (J. P. Feuillet, PMW-182)	1
Applied Measurement Systems, Inc. (J. Diggs, R. Hauptmann)	2
Technology Service Corporation (L. W. Brooks)	2